

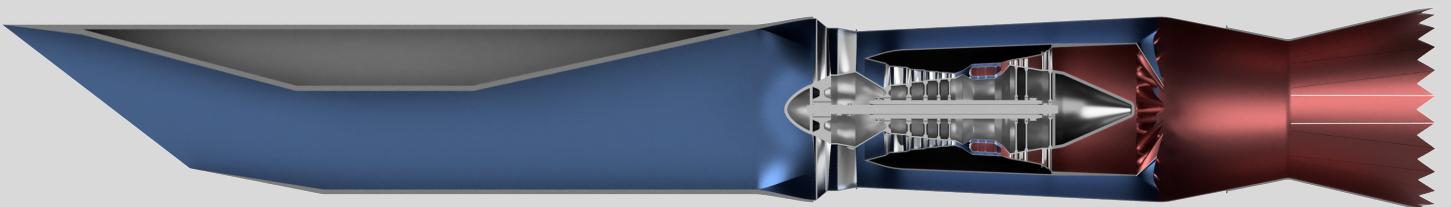


TOBB ETÜ
University of Economics & Technology



ETU-PHOENIX

2020-2021 AIAA ENGINE DESIGN COMPETITION CANDIDATE
LET'S RE-ENGINE THE CONCORDE!



Signatures



FACULTY ADVISOR

Asst. Prof. Sitki USLU

TOBB University of Economics and Technology
Department of Mechanical Engineering

A handwritten signature in black ink that reads "Sitki USLU".



TEAM LEADER

Mert Battal SEN

AIAA Member ID: #1108994

TOBB University of Economics and Technology
Department of Mechanical Engineering

A handwritten signature in black ink that reads "Mert Battal SEN".



TEAM MEMBER

Mustafa Cem CANBAZ

AIAA Member ID: #935345

TOBB University of Economics and Technology
Department of Mechanical Engineering

A handwritten signature in black ink that reads "Mustafa Cem CANBAZ".



TEAM MEMBER

Yagiz Ataberk ERISTI

AIAA Member ID: #1097606

TOBB University of Economics and Technology
Department of Mechanical Engineering

A handwritten signature in black ink that reads "Yagiz Ataberk ERISTI".





TEAM MEMBER

Deniz AKBULUT

AIAA Member ID: #1217353

TOBB University of Economics and Technology
Department of Mechanical Engineering



TEAM MEMBER

Remzi Erdem BARIS

AIAA Member ID: #1217363

TOBB University of Economics and Technology
Department of Mechanical Engineering



TEAM MEMBER

Tuna KOK

AIAA Member ID: #1217365

TOBB University of Economics and Technology
Department of Mechanical Engineering



TEAM MEMBER

Muaz Yusuf TAG

AIAA Member ID: #1217366

TOBB University of Economics and Technology
Department of Mechanical Engineering



TEAM MEMBER

Bugrahan UYSAL

AIAA Member ID: #1217369

TOBB University of Economics and Technology
Department of Mechanical Engineering



TABLE OF CONTENT

1. INTRODUCTION	2
2. STATE OF THE ART	3
3. ENGINE DESIGN PROCESS	3
3.1. Engine Cycle Design	3
3.2. Mission Profile	4
3.3. On Design and Off Design Features and Validation of Baseline Engine	4
3.4. Engine Components of Phoenix	6
3.5. On-Design Analysis and Optimization of Phoenix	6
3.6. Off-Design Analysis of ETU-PHOENIX	8
4.SUPERSONIC INLET DESIGN	11
4.1. Selection of Supersonic Intake	11
4.2 Details of Supersonic Intake Design	11
4.3. Verification of Supersonic Intake at On-Design with Computational Fluid Dynamics	13
4.4. Supersonic Intake Off Design Performance	14
5. AERODYNAMIC DESIGN OF THE TURBOMACHINERY SYSTEM	14
5.1. Design Guidelines for Compressors and Technological Limitations	14
5.2. Detailed Low-Pressure (Fan) and High-Pressure Compressor Design	15
5.3. Design Guidelines for Turbines	18
5.4. Detailed High-Pressure and Low-Pressure Turbine Design	18
5.5. Nozzle Guide Vane Cooling	20
6. COMBUSTION CHAMBER DESIGN	21
6.1. Selection of the Pre-Diffuser Configuration	22
6.2. Fuel Atomizing Flow	22
6.3. Selection of the Rich-Burn Quick-Quench Lean-Burn (RQL) Configuration	22
6.4. Advanced Cooling Techniques	23
6.5. Geometry and Performance of the Combustion Chamber	23
6.6. Computational Fluid Dynamics Analysis and Combustion Chamber Efficiency	25
7. MIXER DESIGN	27
7.1 Mixer Type, Number of Lobes and Shape Selection	27
8 VARIABLE NOZZLE DESIGN	28
8.1 Nozzle Type Selection	28
8.2 Variable Nozzle Geometry	29
8.2.1 Literature Survey About Nozzle Geometry Calculations	29
8.2.2 Phoenix Engine Variable Nozzle Geometry Calculation	30
8.2.3 Computational Analysis of the Nozzle Geometry	31
8.2.4 Off-Design Operation	32

8.3 Variable Exhaust Nozzle	32
9. SHAFT DESIGN	33
.....	35
10. BLADE ANALYSIS	35
11. MATERIAL SELECTION	37
11.1 Inlet Materials	37
11.2 Compressor Materials	38
11.3 Combustion Chamber Materials	38
11.4 Turbine Materials	39
11.5 Mixer-Nozzle Materials	39
11.6 Shaft Materials	39
12. WEIGHT ANALYSIS OF THE PHOENIX ENGINE AND OLYMPUS 593	40
13. ENGINE SUBSYSTEMS	41
13.1. Lubrication System	41
13.2. Oil Cooling	41
13.3. Anti-Icing System	42
13.4. Auxiliary Power Unit	42
13.5. Engine Starter Systems	42
13.6. Engine Control Systems	43
13.7. Fire Detection and Extinguishing Systems	43
14. EMISSIONS	43
15. PERFORMANCE CONSTRAINT ANALYSIS	44
15.1. Drag Polar Estimation	44
15.2. Take-off Distance, Landing Distance, Climb and Supersonic Cruise Constraints	44
16. ENGINE FLOW PATH	45
17. CONCLUSION	46
18. REFERENCES	47
APPENDIX A	48
APPENDIX B: TECHNICAL DRAWINGS OF THE COMPONENTS	49
APPENDIX C: TECHNICAL DRAWINGS OF THE COMPONENTS (Drawing Sheet Scales: A3)	49

LIST OF TABLE

Table 1. Concorde’s Technical and Engine Properties.....	2
Table 2. State-of-the-Art Engines’ Properties.....	3
Table 3. Base Engine (Olympus 593) Specifications	4
Table 4. Critical Flight Phases’ Properties for Base Engine.....	4
Table 5. Total Fuel Consumption of Base Engine (Olympus 593) (per engine).....	6
Table 6. Station Numbers.....	6
Table 7. Total Fuel Consumption of PHOENIX (per engine).....	10
Table 8. Comparison of Base Engine and PHOENIX.....	10
Table 9. Inlet Variables and Values Used in MATLAB.....	12
Table 10. Geometrical Results of the Intake.....	12
Table 11. Mach Numbers, Shock and Ramp Angles of Each Stages.....	12
Table 12. Mach Number at Stages	13
Table 13. PRF Result Comparison.....	13
Table 14. Variable Ramp Angles for Off-Design Conditions.....	14
Table 15. Technological Developments of the Turbomachinery Components for given Time Periods [14].....	15
Table 16. Guidelines on the Ranges and Typical Values of Compressor Parameters [14,21].....	15
Table 17. Thermodynamic and Geometrical Properties of Low-Pressure and High-Pressure Compressors.....	15
Table 18. Detailed Design Parameters of High-Pressure Compressor.....	17
Table 19. Detailed Design Parameters of Low-Pressure Compressor.....	17
Table 20. Certain Design Parameters for Turbines [14,23,24,25].....	18
Table 21. Thermodynamic and Geometrical Properties of High-Pressure and Low-Pressure Turbines.....	18
Table 22. Detailed Design Parameters of High-Pressure and Low-Pressure Turbines.....	20
Table 23. Typical Design Parameters of the Combustion Chamber [30,31,33,34].....	23
Table 24. On-Design Conditions of the Combustion Chamber.....	23
Table 25. Geometrical Results of the Combustion Chamber.....	24
Table 26. Flame Tube Hole Parameters.....	24
Table 27. Performance Constraints of the Combustion Chamber [30,31,33,34].....	24
Table 28. Combustion Chamber Performance Parameters.....	24
Table 29. Information Related with Generated Mesh.....	25
Table 30. CFD Results of the Combustion Chamber.....	26
Table 31. Nozzle MATLAB Inputs and Outputs for On-Design Condition.....	30
Table 32. Input Parameters of Each Mission Profile.....	30
Table 33. Calculated Nozzle Parameters for Mission Profiles (MATLAB).....	31
Table 34. CFD, MATLAB and GasTurb13 Results of the Nozzle.....	32
Table 35. Shaft Design Criterion.....	34
Table 36. MATLAB Results of the Each Shaft.....	34
Table 37. Technical Properties of BPTO-219743.....	34
Table 38. Fan and Compressor Blades’ Properties [55,56].....	36
Table 39. Turbine Blades’ Properties [57,58,59,60].....	37
Table 40. Inlet Material Properties [65].....	38
Table 41. Compressor Material Properties [55].....	38
Table 42. Compressor Material Mechanical Properties [72,73].....	39
Table 43. Frequently used nozzle materials by GE, P&W, RR [57].....	39
Table 44. Component-Material Overview.....	40
Table 45. Engine ETU-PHOENIX and Base Engine Weight Analysis Parameters and Results.....	40
Table 46. Physical Properties and Mass at Each Components.....	41
Table 47. Proposed NOx Emissions Correlation Constant and Exponent Default Values for RQL Combustor [97].....	43
Table 48. LTO Cycle for Supersonic Engines and Emission Comparison Between Phoenix and Standards.....	44
Table 49. Drag Polar Estimations for the Concorde.....	44
Table 50. Features and Improvements of the PHOENIX Engine.....	46
Table 51. Properties of Velocity Triangles for Mid-Section of LPC.....	48
Table 52. Properties of Velocity Triangles for Mid-Section Inlet of High-Pressure Compressor.....	48
Table 53. Properties of Velocity Triangles for Mid-Section Outlet of High-Pressure Compressor.....	48
Table 54. Properties of Velocity Triangles for Mid-Section of High-Pressure Turbine.....	48
Table 55. Properties of Velocity Triangles for Mid-Section of LPT.....	48

LIST OF FIGURE

Figure 1. Diagram of a Turbofan Engine and Different Engine Efficiencies [2,3]	2
Figure 2. Concorde Mission Profile.	4
Figure 3. Baseline Engine Performance at Cruise Condition	5
Figure 4. Baseline Engine Takeoff Condition Output	5
Figure 5. PHOENIX Engine Configuration Schematic	6
Figure 6. Parametric Studies of PHOENIX Engine	7
Figure 7. PHOENIX Engine Performance at Cruise Condition	8
Figure 8. PHOENIX Engine Performance at Takeoff (left) and Supersonic Climb (right) Conditions	8
Figure 9. Compressor and Turbine Maps Generated ETU-PHOENIX Performance Team	9
Figure 10. Detailed Output of Take-off Condition	9
Figure 11. Comparison of Fuel Consumption in Each Segment (Left) and Comparison of Fuel Consumption (Right)	10
Figure 12. Relationship between Total Pressure Recovery and Freestream Velocity [14]	11
Figure 13. Modes of Operation: a) (at $M < 1.3$), b) (at $M > 1.3$), c) at Critical Flow Regime Under Cruise Conditions, d) at Subcritical Regime Under Cruise Conditions, and e) at Supercritical Regime Under Cruise Conditions (Concorde flight manual) [20]	11
Figure 14. Sketch of a Mixed Compression Intake [15]	11
Figure 15. Pressure Recovery Factor vs Mach Number (MIL-E-5007 Standard) (left), Pressure Recovery Factor vs Up-Stream Mach Number (right)	12
Figure 16. Mach Number Contours	13
Figure 17. Density Gradient Contours	13
Figure 18. 3-D CAD Model of Supersonic Intake	14
Figure 19. Preliminary Design of Low-Pressure Compressor Rotor and Stator (left), Preliminary Design of High-Pressure Compressor Rotor and Stator (right)	16
Figure 20. Temperature Distribution of Fan (left), Total Pressure Distribution of Fan (middle), and Relative Mach Number at Tip Section of Fan's Rotor (right)	16
Figure 21. Temperature Distribution of HPC (top), Total Pressure Distribution of HPC (bottom)	16
Figure 22. 3-D CAD Geometries of the Fan (left) and the High-Pressure Compressor (right)	17
Figure 23. Preliminary Design of HPT Rotor and Stator (left), Preliminary Design of LPT Rotor and Stator (right)	18
Figure 24. Temperature Distribution of High-Pressure Turbine (left), Total Pressure Distribution of High-Pressure Turbine (right)	19
Figure 25. Temperature Distribution of Low-Pressure Turbine (left), Total Pressure Distribution of Low-Pressure Turbine (right)	19
Figure 26. 3-D CAD Geometry of the High-Pressure Turbine (left) and the Low-Pressure Turbine (right)	19
Figure 27. Smith Chart for Turbine Efficiency	19
Figure 28. a) Convection Cooling, b) Impingement Cooling, c) Film Cooling, d) Full-Coverage Film Cooling, e) Transpiration Cooling [21] (left), Cooling Systems for Ranges of Turbine Entry Temperatures [14] (right)	20
Figure 29. Cooled Nozzle Guide Vane of the PHOENIX	21
Figure 30. The Types of the Combustor (Annular Combustor (left), Can Combustor (middle), Turbo-annular Combustor (right)) [29]	21
Figure 31. Geometric Representation and Main Components of an Annular Combustor [28]	21
Figure 32. Representation of the Dump Diffuser [28]	22
Figure 33. Air-blast Atomizer of ETU-PHOENIX	22
Figure 34. Film Cooling Methodologies ((a) Wigglestrip, (b) Stacked Ring, (c) Splash-Cooling Ring, (d) Machined Ring) [28]	23
Figure 35. 3-D CAD Model of the Combustion Chamber of ETU-PHOENIX (left), 180° Section of the Combustion Chamber of ETU-PHOENIX (middle), 15° Section of Annular Combustion Chamber of ETU-PHOENIX (right)	25
Figure 36. Combustion Efficiency vs. Combustion Loading Parameter [14] (left), Design Parameters and Values for Supersonic Condition (right)	25
Figure 37. Boundary Conditions of the Geometry (left), Generated Mesh for the Geometry (right)	26
Figure 38. Temperature at Mid-Plane (top-left), Temperature at Outlet Plane (top-right), Velocity Magnitude at Mid-Plane (bottom-left), Velocity Vector at Mid-Plane (bottom-right)	26
Figure 39. Mixed Flow Turbofan Engine Core and Bypass Flow (Left), Expected Flow Development from The Mixer (Right) [35]	27
Figure 40. Comparison of Mixers with Different Number of Lobes (Left: Total Temperature Contours, Top-Right: Mixedness Index - Axial Distance Graph, Bottom-Right: Mixedness Index & Pressure Drop Values) [37]	27
Figure 41. Thermal Mixing Efficiency and Total Pressure Recovery Coefficient Along the Axis of the Different Lobed Mixers and Mixer Geometries [39]	28
Figure 42. Geometry Inputs and 3-D CAD Design of the ETU-PHOENIX Mixer	28
Figure 43. Boundary Conditions of the Nozzle Geometry	31
Figure 44. Mach Number and Density Gradient Contours of Geometries with Divergent Section Angles of 11,13 and 15 Degrees	31
Figure 45. CFD Analysis of Off-Design Condition	32
Figure 46. 3-D CAD Model of the ETU-PHOENIX Engine's Nozzle	33
Figure 47. Two Spool Shaft Structure and Bearing Placement [47]	33
Figure 48. 3-D CAD Drawing of the Shaft (Left), 3-D CAD Drawing of the ETU-PHOENIX Engine's Rotors (Right)	35
Figure 49. Rotor Nomenclature (left) and Centrifugal Stress on a Blade (right)	35

Figure 50. Materials used in engine structure through the years [57]	37
Figure 51. Alloy Comparisons Based on a Combination of Creep and Oxidation(left) & Hot-Corrosion Test Results (middle) and Tests for Cyclic Oxidation (right) [61].....	39
Figure 52. Dry-sump Lubrication Systems (left) [2], Wet-sump Lubrication Systems (right) [82].....	41
Figure 53. Hot Air Anti-Icing System [84]	42
Figure 54. Air Turbine Starters [88].....	42
Figure 55. FADEC System [92]	43
Figure 56. Fire Extinguishing System [95]	43
Figure 57. The Concorde Constraint Diagram with Phoenix Engine	45
Figure 58. The PHOENIX Engine Airflow Path (blue=cold side, red=hot side)	45
Figure 59. Final Representation of ETU-PHOENIX.....	46
Figure 63. Velocity Triangles of Low-Pressure Compressor for Mid-Section.....	48
Figure 64. Velocity Triangles of High-Pressure Compressor for Mid-Section	48
Figure 65. Velocity Triangles of High-Pressure Turbine for Mid-Section.....	48
Figure 66. Velocity Triangles of Low-Pressure Turbine for Mid-Section	48
Figure 61. Detailed Output of PHOENIX at Climb Condition	49
Figure 62. Detailed Output of PHOENIX at Supersonic Cruise Condition	49
Figure 60. Engine Overall Geometry from GasTurb 13.....	49

NOMENCLATURE

m_{core} : Core Mass Flow Rate (lb)

$\left(\frac{T}{W}\right)_{TO}$ Take-off thrust-to-weight ratio

λ Bypass ratio

s_{TOG} Ground run take-off distance

$\left(\frac{W}{S}\right)_{TO}$ Take-off wing loading

ρ_{sea} Density at sea level (59°F)

$C_{D0(TO,GD)}$ Parasite drag coefficient at take-off (Gears down configuration)

$C_{Lmax,TO}$ Maximum lift coefficient at take-off

μ_G Ground friction coefficient

V_{SL} Stall speed during landing

$C_{Lmax,L}$ Maximum lift coefficient during landing

$\frac{W_L}{W_{TO}}$ Ratio of landing weight to take-off weight

N_{engine} Number of engines on the aircraft

$L/D_{approach}$ Lift-to-drag ratio at approach position.

CGR Climb Gradient

α Thrust Ratio

β Weight Ratio

q_{cruise} Dynamic Pressure at cruise

K_1 Viscous drag coefficient

$C_{D0(clean)}$ Parasite drag coefficient (Clean configuration)

TSFC: Thrust Specific Fuel Consumption

LPC: Low Pressure Compressor

HPC: High Pressure Compressor

LPT: Low Pressure Turbine

HPT: High Pressure Turbine

T3: Compressor Exit Temperature

T4: Combustion Chamber Exit Temperature

OPR: Overall Pressure Ratio

FPR: Fan Pressure Ratio

BPR: Bypass Ratio

TET: Turbine Entry Temperature

PRF: Pressure Recovery Factor

M: Mach

x-D: x Dimensional

TF: Turbofan

TJ: Turbojet



Abstract

This report explains the design of the PHOENIX low bypass turbofan engine within the scope of the Undergraduate Team Engine Design Competition titled "Let's Re-Engine the Concorde" organized by AIAA. The PHOENIX engine developed within the scope of the Engine Design Competition is expected to meet the desired specifications and meet all the Concorde requirements, the platform on which it will be used, and to perform better than competing engines. Concorde, a milestone in aviation, was removed from the airline companies' inventory due to its high fuel consumption. Therefore, it is expected that the fuel consumption of Concorde will be reduced in the new engine to be designed. In addition, the engine mass, which has a negative impact on fuel consumption, should be reduced in the candidate engine that will enter service in 2028 with the help of developing technology.

As a result of the designs made for this target, the performance calculations of the PHOENIX engine have been made. All engine components were pre-dimensioned with optimized performance design parameters, and the final geometries of the components were obtained as a result of subsequent calculations and flow analysis. At the same time, the total mass of the PHOENIX was calculated by making material selections for each component, and its mass was compared with the Olympus 593, which is the base engine. The report includes engine subsystems and emission calculations. During the entire design process, a method such as updating the performance calculations and detailed designs of the components to verify each other and thus make an iterative study was followed. As a result of the analysis, it has been observed that PHOENIX meets the desired requirements, therefore the applied design methodology is considered to be suitable. The details of the designs and analyzes mentioned in this report will be accessible, and the performance results will be examined. Details of the methods used in the design process will be available. Also, CAD drawings of the engine will be able to be examined.

1. INTRODUCTION

A new low bypass ratio mixed turbofan engine design is required for a new version of the 120-passenger supersonic jet “Concorde” with an entry-into-service date of 2028. Our supersonic engine Phoenix has been designed for accomplishing the mentioned supersonic jet. Baseline engine Olympus 593 will be the origin of the project. The baseline engine will be optimized for engine size, mass, and SFC. During the optimization operation, the best values of fan pressure ratio, bypass ratio, overall pressure ratio and turbine entry temperature should be selected. Overall Pressure Ratio (OPR), Fan Pressure Ratio (FPR), Bypass Ratio (BPR) and Turbine Entry Temperature (TET) are main performance indicators of this design. In addition: reheat elimination, jet velocity reduction, T3, T4 limitations are considered. These values will be acceptable with the entry-into-service of 2028 [1].

After the optimization is done, the fuel burn should be minimized, and the flight range will be automatically increased. Thrust-specific fuel consumption should be decreased significantly because of the absence of reheat while thrust value is kept constant. In addition to these, the engine mass should be minimized.

Also,

- 🔥 The supersonic cruise flight should be at 53000 ft/Mach 2.01. These two flight conditions should be used for the design point for the optimum engine.
- 🔥 Turbofan engine components such as inlet, fan, compressor, spools, combustion chamber, turbine, mixer, and nozzle will be designed. Subsystems of the engine will also be considered and be examined while designing these components.
- 🔥 The diameter of the new engine should be kept at minimum.
- 🔥 A new limit will be set to T4.
- 🔥 T3 will be limited to 1620 R.
- 🔥 An appropriate inlet and nozzle should be designed. The components' noise values will be met airport noise requirements without a noise suppressor. To achieve that, nozzle jet velocity at take-off be limited to 1150 ft/s.
- 🔥 Concorde was an environmental failure. The engine should be environmentally friendly. Emission gasses are a significant public concern because of their impact on human health and the environment [1].

For cruise speeds lower than 800 mph, using a low bypass turbofan engine for an aircraft is more efficient than using a turbojet engine (Figure 1). However, in the early times of jet technology, turbofan engines were rejected in some aircraft due to their larger cross-section producing excessive drag. For the same reason, in the 20th century’s fastest civil aircraft, Concorde, engineers decided to use Olympus 59, a turbojet engine whose properties are given in Table 1. Concorde was an iconic figure of aviation and still is. Its unique aerodynamic shape is well-known for many people who are interested in aerospace. Unfortunately, it was also an environmental and financial failure. Expensive, noisy and inefficient: Concorde’s flights were stopped on 24 October 2003 and since then, there are no supersonic commercial flights available on the whole globe [1].

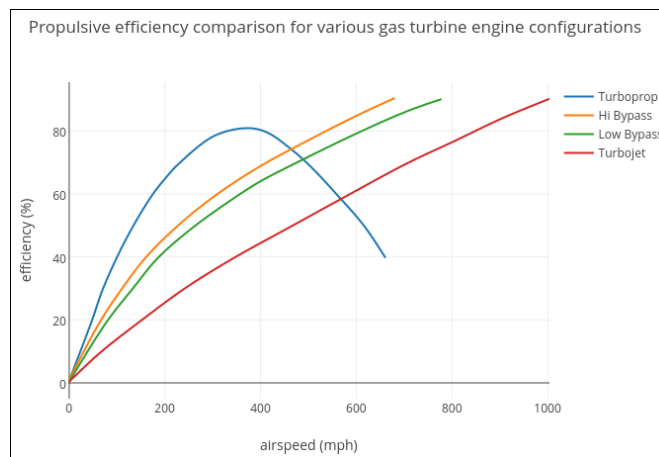


Figure 1. Diagram of a Turbofan Engine and Different Engine Efficiencies [2,3]

Table 1. Concorde’s Technical and Engine Properties

Length	2441 in	Maximum Thrust	Reheat ON: 38050 lbf
Wingspan	1023.5 in		Reheat OFF: 32000 lbf
Maximum Take-Off Weight	408009.5 lbm	Engine Components	Compressor: Axial-flow, 7-stage LP, 7-stage HP
Height	480.3 in		Combustion Chamber: Nickel alloy construction annular chamber
Engine	4 x Olympus 593 Turbojet		Turbine: Two stages: one HP, one LP
Cruise Speed	1967 ft/sec	TSFC	Reheat ON: 1.39 lbm/(lbf*h) (sea level)
Range	23750 ft		Reheat OFF: 1.195 lbm/(lbf*h) (cruise)
Flying Altitude	53000 ft	Overall Pressure Ratio	15:5:1
Length & Diameter (in)	159 /47.7		
Thrust-to-Weight Ratio	5.4		

“What Concorde showed is there is a market for customers who want to reach destinations faster. What we need to figure out is how to do the Concorde, but we need to do it safer, more efficiently and more sustainably.”- Spike CEO Vik Kachoria.

Although Concorde was not a commercial and environmental achievement, it can be re-designed with 21st-century technology when preserving its original shape. Seeing the Concorde in the air again is an engineering necessity for aviation enthusiasts, which was once the fastest plane in the skies. A phoenix symbolizes birth, death and rebirth, a magical bird, radiant and shimmering, which lives for several hundred years before it dies by bursting into flames. It is then reborn from the ashes to start a new, long life. This is the reason why we chose the “Phoenix Engine Design Team” as our team’s name to represent the re-birth of the Concorde. Starting with the base engine validation, some optimization studies were executed. As a result, Phoenix Engine resulted as:

- 🔥 **31% less fuel usage** from the base engine,
- 🔥 **No need to reheat** while taking off,
- 🔥 **No sonic booms** while taking off.

In the following sections, state of the art in technology research, engine cycle analysis and subsection designs are given in detail.

2. STATE OF THE ART

The aviation sector is developing and growing day by day. It is a sector where people constantly push the boundaries, where all the possibilities of technology are used and where developments that will lead many sectors are realized. The aviation industry, where many countries make large investments and continuously grow their research and development activities, is also seen as a source of prestige. While the activities carried out especially in the military field bring the defense power of the country to the forefront, its export capacity enables it to gain economic power. For this reason, engine and aircraft manufacturers produce a wide range of products.

Before starting to design any section, state of the art must be regulated to get a concept about the design operations and the verifications. In this project, engines for the state-of-the-art are selected as turbojet and turbofan engines and also the conditions are chosen to near the number of Mach. The benchmarks are engine type, Mach number, overall pressure ratio, bypass ratio, thrust, TSFC and its mission (military or civil). The engines with a low bypass ratio and close to the desired thrust are listed in Table 2 below.

Table 2. State-of-the-Art Engines’ Properties

	OPR	BPR	Thrust [lbf]	SFC[lb/lbf.h]	Weight [lbm]	Thrust to Weight Ratio (TO)(T/W)	Size[in]
Kuznetsov NK-321 (TF)	28.40	1.40	55078 30798	0.0258 0.06	7500	7.35	L=240/Dia=57.48
Kuznetsov NK-86 (TF)	N/A	1.15	28550	N/A	3395	8.41	L=245/Dia=63
Pratt & Whitney TF30 (TF)	19.8	0.87	25088 14567	N/A	3984	6.3	L=241.7/Dia=48.8
NK-144A Turbofan (TF)	14.20	0.53	40000 10566	0.0325 0.064	N/A	N/A	L=204.7/Dia=59
F101-GE-102 (TF)	26.8	1.91	136916 77355	0.56 2.46	4449	7.04	L=180.7/Dia=55.2

It is seen that the values of the Concorde base engine Olympus 593 coincide with the Tu-144D engine Kolesov RD-36. The Tupolev-144D is the Soviet version of the Concorde, referred to as "Concordski" in some sources. While performing engine optimization, changes have been made mainly on important basic parameters such as fan pressure ratio, bypass ratio, total pressure ratio and turbine inlet temperature. For this reason, it is important to examine the values reached by today's technologies in these parameters. The total pressure ratio parameter has an important place in the technology of turbofan engines. Roughly speaking, increasing the total pressure ratio increases the efficiency of the engine and enables a reduction in fuel consumption. However, increasing the compressor stage creates a disadvantage in motor weight.

3. ENGINE DESIGN PROCESS

Within the scope of the project, literature studies have been conducted by taking into consideration the technological developments to be carried out until 2028 which is entry into the service year.

3.1. Engine Cycle Design

This chapter describes the basic structures of the engine and documents the cycle analysis program that was used to aid in the design process of the Phoenix and baseline engine.

The analysis code used to complete the cycle analysis was the gas turbine simulation software GasTurb 13, and the simulation of the Phoenix is available from the author upon request. Baseline engine validation is an important reference and starting point for the engine to be designed. Therefore, the aircraft engine design process starts with the validation of the baseline engine model.

Validation also is an indication that correct assumptions will be made during the cycle design process of the newly designed engine. After the validation, the selection of the optimized engine PHOENIX's cycle and features, thermodynamic analysis and optimization process would be completed.

3.2. Mission Profile

In engine design and optimization processes, it is important to check engine operability under On-Design and Off-Design conditions. At this point, the "Off-Design" tool and "Map Scaling" play an important role. Under different flight conditions, the engine must provide the minimum thrust requirement. A detailed literature study has been conducted to determine the flight Mach number, altitude and minimum thrust that must be met in each flight phase. Accordingly, various mission profiles of Concorde's New York-Paris and New York-London flights were examined, and a mission profile based on the New York-Paris flight was created. In the Taxi condition, requirement thrust was determined such as 7% of the Take-Off thrust [4]. Figure 2 shows a simplified mission profile for only one engine of the Concorde. [5,6]

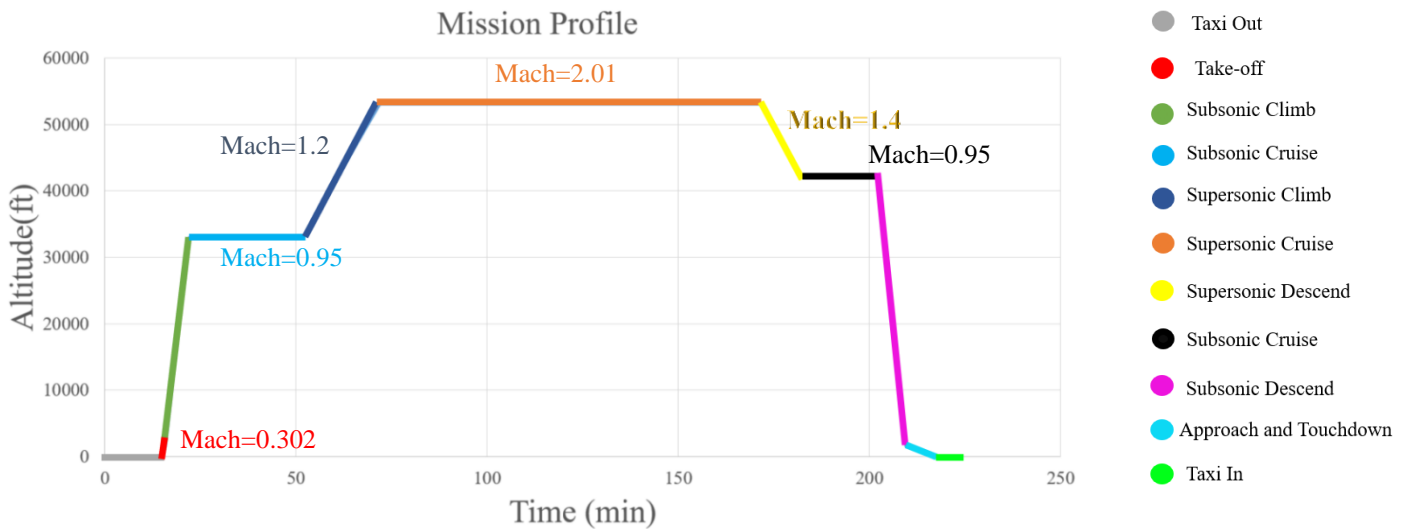


Figure 2. Concorde Mission Profile.

3.3. On Design and Off Design Features and Validation of Baseline Engine

It is necessary to decide which point should be chosen as the design point before the design of the new engine. For engines with supersonic flight characteristics, the top of climb (cruise) condition is considered by AIAA as the design point rather than take-off condition. As stated in the competition RFP, the On-Design point has been determined as cruise condition for base engine Olympus 593 and PHOENIX. Some features and basic performance characteristics of the baseline engine are given in Table 3. In Figure 3, the validation results of the baseline engine at cruise conditions obtained by using the GasTurb 13 program are given in detail. When Figure 3 is examined, it is clearly seen that the baseline engine model given in RFP has been successfully validated. The base engine Olympus 593 was performed in Two Spool Turbojet configuration. Flight information regarding the Off Design conditions, take-off and maximum climb are given in Table 4 together with the On Design condition.

Table 3. Base Engine (Olympus 593) Specifications

Engine Type	Turbojet
Number of LP/HP Compressor Stages	7,7 Axial
Thrust Req. per engine at supersonic cruise (ft)	10031
TSFC at Cruise (lbm/lbf.h)	1.3304
Max Thrust per engine at Take-Off	33610
Max. Envelope Diameter (in)	48
Length (Without Intake and Nozzle) (in)	159
Engine Weight	7000 lb

Table 4. Critical Flight Phases' Properties for Base Engine

	Design	Off Design	
	Cruise	Take-Off	Supersonic Climb
Mach Number	2.01	0.302	1.2
Altitude (ft)	53000	0	40000
Conditions	ISA + 5°C	ISA + 10°C	ISA + 5°C
PRF	0.937	0.986	0.986
Afterburner	Off	On	On
Net Thrust (lbf)	10031	33600	13618
TSFC (lbm/lbf.h)	1.3300	1.2576	1.3717

2-Spool Turbojet
Alt=53000ft / Mn=2.000 ISA

Station	W lb/s	T R	P psia	WRstd lb/s		
amb		389,97	1,456		FN =	10031,95 lb
1	289,345	701,78	11,402		TSFC =	1,3304 lb/(lb*h)
2	289,345	701,78	10,684	462,971	FN/W2 =	1115,51 ft/s
24	289,345	1098,53	43,803		WF Burner=	3,70746 lb/s
25	289,345	1098,53	43,365	142,705	P2/P1 =	0,9370
3	289,345	1537,76	125,757	58,221	P25/P24 =	0,9900
31	257,517	1537,76	125,757		P3/P2 =	11,7711
4	261,224	2430,00	120,727	68,828	P45/P44 =	0,9800
41	275,692	2385,73	120,727	71,975	P6/P5 =	0,9800
43	275,692	1965,47	47,934			
44	290,159	1944,88	47,934			
45	290,159	1944,88	46,976	175,776	W NGV/W25=	0,05000
49	290,159	1589,72	18,800		WHcl/W25 =	0,05000
5	290,159	1589,72	18,800	397,100	WLcl/W25 =	0,00000
6	290,159	1589,72	18,424		XM6 =	0,50000
8	290,159	1589,72	18,424	405,204	A8 =	1260,71 in ²
Bleed	2,893	1537,76	125,757		WBld/W2 =	0,01000

Efficiencies:	isent	polytr	RNI	P/P	Ang8 =	25,00 °
LP Compressor	0,8530	0,8782	0,507	4,100	CD8 =	0,95000
HP Compressor	0,8170	0,8402	1,208	2,900	P8/Pamb =	12,65199
Burner	0,9900			0,960	WlkLP/W25=	0,00000
HP Turbine	0,8900	0,8785	1,378	2,519	Loading =	100,00 %
LP Turbine	0,9000	0,8890	0,677	2,499	e444 th =	0,85985

HP Spool mech Eff	0,9900	Nom Spd	8382 rpm		Wlko/W25 =	0,00000
LP Spool mech Eff	0,9900	Nom Spd	5819 rpm		FWX =	100,0 hp

Con-Di Nozzle:					Core Eff =	0,5425
A9*(Ps9-Pamb)	1536,275				Prop Eff =	0,7778

hum [%]	war0	FHV	Fuel		A9/A8 =	1,80000
0,0	0,00000	18552,4	Generic		CFGid =	0,95633

Figure 3. Baseline Engine Performance at Cruise Condition

Thanks to the Off-Design analysis, the operability of the engine in different flight phases, which are other operating conditions, is examined. The base engine's Off-Design analysis was performed in order to compare PHOENIX and the base engine Olympus 593 not only in On-Design but also in Off-Design. The output of the base engine's take-off condition is given in Figure 4. Compressor maps had to be scaled. Since maps and "Map Scaling" are also made for PHOENIX, compressor and turbine maps are not given for the base engine. PHOENIX's maps will be given in the new engine design section.

With the Mission tool in GasTurb 13's Off Design part, TSFC values in each flight phase are determined. The total fuel consumption of the base engine was calculated to be compared with Phoenix by using the times determined by the literature studies [7,8,9,10]. It can be seen from various sources that the Concorde consumed around 1.5-2 tons of fuel during the taxi. When it is calculated for four engines, this value also validates the mission profile. In Table 5, flight Mach number, altitudes, calculated required thrust and fuel consumption values for one engine are given for baseline engine Olympus 593.

Station	W lb/s	T R	P psia	WRstd lb/s		
amb		518,67	14,696		Reheat on	
1	542,651	528,15	15,656		FN =	33611,27 lb
2	542,651	528,15	14,670	548,571	TSFC =	1,2576 lb/(lb*h)
24	542,651	888,90	68,507		FN/W2 =	1992,83 ft/s
25	542,651	888,90	67,712	154,182	WF Burner=	8,50070 lb/s
3	542,651	1330,35	234,555	54,452	WF total =	11,74189
31	482,959	1330,35	234,555		P2/P1 =	0,9370
4	491,460	2433,78	226,345	69,121	P25/P24 =	0,9884
41	518,593	2380,00	226,345	72,126	P3/P2 =	15,9892
43	518,593	1971,84	90,763		P45/P44 =	0,9803
44	545,725	1941,50	90,763		P6/P5 =	0,9838
45	545,725	1941,50	88,975	174,391	P16/P6 =	1,7503
49	545,725	1626,86	39,784		P16/Ps6 =	1,9800
5	545,725	1626,87	39,784	357,023	W NGV/W25=	0,05000
6	545,725	1626,87	39,139		WHcl/W25 =	0,05000
61	545,725	903,81	39,139		WLcl/W25 =	0,00000
7	249,007	1977,50	37,935		XM6 =	0,43286
8	548,966	1977,50	37,935	415,250	XM61 =	0,43286
13	0,000	888,90	68,507		XM7 =	0,52284
16	0,000	888,90	68,507		A8 =	1291,18 in ²
Bleed	5,427	1330,35	234,555		BypBld =	0,00000 lb/s

Efficiencies:	isent	polytr	RNI	P/P	WclNozzle=	0,00000 lb/s
LP Compressor	0,8018	0,8388	0,977	4,670	WBld/W2 =	0,01000
HP Compressor	0,8109	0,8391	2,424	3,464	BFR =	0,0000
Burner	0,9916			0,965	Ang8 =	21,87 °
HP Turbine	0,8789	0,8666	2,591	2,494	CD8 =	0,95625
LP Turbine	0,9024	0,8931	1,285	2,236	P8/Pamb =	2,58134
Reheat	0,9327			0,969	WlkLP/W25=	0,00000

HP Spool mech Eff	0,9900	Speed	8079 rpm		Loading =	100,00 %
LP Spool mech Eff	0,9900	Speed	5348 rpm		e444 th =	0,85389

Con-Di Nozzle:					Wlko/W25 =	0,00000
A9*(Ps9-Pamb)	364,539				far7 =	0,02186

hum [%]	war0	FHV	Fuel		P5/P2 =	2,7120 EPR
0,0	0,00000	18552,4	Generic		FWX =	100,0 hp

Figure 4. Baseline Engine Takeoff Condition Output

Table 5. Total Fuel Consumption of Base Engine (Olympus 593) (per engine)

Segment	Altitude (ft)	Mach Number [5]	Thrust (lbf)	TSFC (lbm/lbf*h)	Fuel Flow (g/sec)	Time (min)	Fuel Burned in Segment (lbm)
Taxi Out	0	0.019	2351.5 [5.6]	1.2578	49.3 [6]	15 [7]	788.77 [8]
Take Off	0	0.302	33600	1.2576	704.25	1.0	704.24
Subsonic Climb	17750	0.7	22170	1.343	496.24	6	2977.43
Subsonic Cruise	33000	0.95	14524	1.366	330.67	30	9920
Supersonic Climb	40000	1.2	13618	1.3717	311.33	20	6226.58
Supersonic Cruise	53000	2.01	10031	1.3301	222.23	100	22235.4
Supersonic Descend	45000	1.4	8162	1.2310	167.46	10	1674.6
Subsonic Cruise	42000	0.95	8428	1.1860	166.59	20	3331.87
Subsonic Descend	22500	0.6	15744	1.1470	300.97	7.5	2257.27
Approach & Touchdown	1500	0.24	23000 [9]	1.1024	422.55[6]	7.5[10]	3169.12
Taxi In	0	0.019	2351.5	1.2578	49.3	6[7]	295.77
TOTAL						Approx.:4hr[9]	53580 lbm [9]

3.4. Engine Components of Phoenix

Phoenix was designed as a low bypass, 2-spool mixed flow turbofan engine. The optimum engine Phoenix has an air intake system, 1 stage fan, 5 stage HPC (High-pressure compressor), combustor and fuel system, 2 stage HPT (High-pressure turbine), 1 stage LPT (Low-pressure turbine), mixer and exhaust systems. Stage numbers and efficiencies were found by making an iterative study between performance and turbomachinery studies. The applicability of the number of stages and efficiencies determined by performance calculations was examined in AxSTREAM. This iterative study continued until the maximum achievable efficiency was reached, and in this process, both performance calculations and turbomachinery studies were updated. For the maximum achievable efficiency, temperatures and speeds around the blades were examined, and the compatibility of various factors such as De-Haller, Zweifel coefficient, etc., to the literature was taken into consideration. Phoenix is designed for use in Concorde flying in supersonic conditions. Therefore, the Convergent-Divergent Nozzle with variable bypass channel technology and variable nozzle area is used to achieve the desired thrust and thrust specific fuel consumption.

PHOENIX's engine configuration is shown in Figure 5. The engine detailed station schematic of PHOENIX given in Figure 5 has station numbers created automatically by GasTurb 13. Table 6 shows which component these numbers represent.

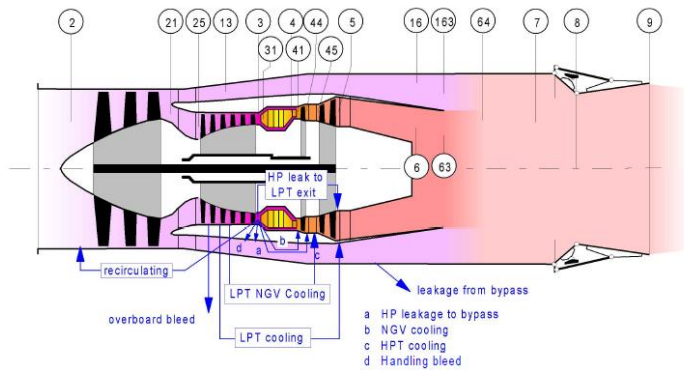


Table 6. Station Numbers

Station Numbers	Stations	Station Numbers	Stations
2	Fan Inlet	5	LP Turbine Exit
21	Fan Exit to Core	6	Exit Guide Vane Exit
25	HP Compressor Inlet	13	Bypass Inlet
3	HP Compressor Exit	16	Bypass Exit
4	Burner Exit	8	Nozzle Throat
44	HP Turbine Exit	9	Nozzle Exit
45	LP Turbine Inlet		

Figure 5. PHOENIX Engine Configuration Schematic

3.5. On-Design Analysis and Optimization of Phoenix

A detailed literature study on new engine technologies and various concepts of turbofan engine components has been made for the design of Phoenix. At the end of the literature study, it is aimed to select and design the engine in the best combination among the concept designs in order to meet the desired performance criteria for the new engine design and to provide the limits specified in the specified standard and RFP in the best way. As stated in the proposal, the new engine to be designed for the supersonic flying Concorde had to be a low bypass turbofan. An important point here is the Spool number. For the selection of spool numbers, a literature search was done and 2-Spool and 3-Spool options were compared. 2-Spool shaft was chosen because of the advantages of the 2-Spool option, such as providing lower weight without additional parts, having a simpler design and having a lower production cost than 3-Spool. [11][12] As a result, it was decided to select the 2-Spool Mixed Turbofan configuration. After selecting the engine cycle and deciding on the concept designs to be used in the new engine, performance analysis and optimization for the Phoenix engine were initiated. GasTurb 13's Optimization tool was used for optimization and trade studies were completed with the Parametric tool.

In the optimization of the engine, the specific fuel consumption has been tried to be reduced by using various parameters such as turbine inlet temperature, bypass rate, fan pressure ratio, overall pressure ratio by preserving the thrust force predicted for the cruising condition of the base engine with the help of the task profile. The main considerations in engine design are engine diameter, mass and TSFC. Concorde's high cost to commercial passenger transport companies caused it to be decommissioned, so Phoenix's design focused specifically on improving the TSFC. In addition, the improvement in engine mass will allow the TSFC to be improved. [13] In addition, the improvement in engine mass will allow the TSFC to be improved. For this reason, although the diameter of the engine will increase due to the addition of bypass, it is also aimed to reduce the mass of the engine by keeping this increase at a minimum and benefiting from the developing material technology. Mass flow corrected, BPR, TET, OPR, FPR, HPC pressure ratio parameters have been optimized for the improvement of TSFC. GasTurb 13 Cruise output of optimum engine PHOENIX is given in Figure 7. The trade studies on this optimization process are given in Figure 6. An iterative study was carried out between On-Design and Off-Design points to ensure the exit speed of 1150 ft/s on take-off condition. For PHOENIX to comply with the limit, TET had to be kept low, BPR kept high and mass flow rate increased. In fact, to design the engine more compact by reducing the engine diameter, Phoenix's TET has been improved according to the base engine, but considering its effect on the output speed, the maximum TET limit, which is 3150 Rankine, has not been reached.

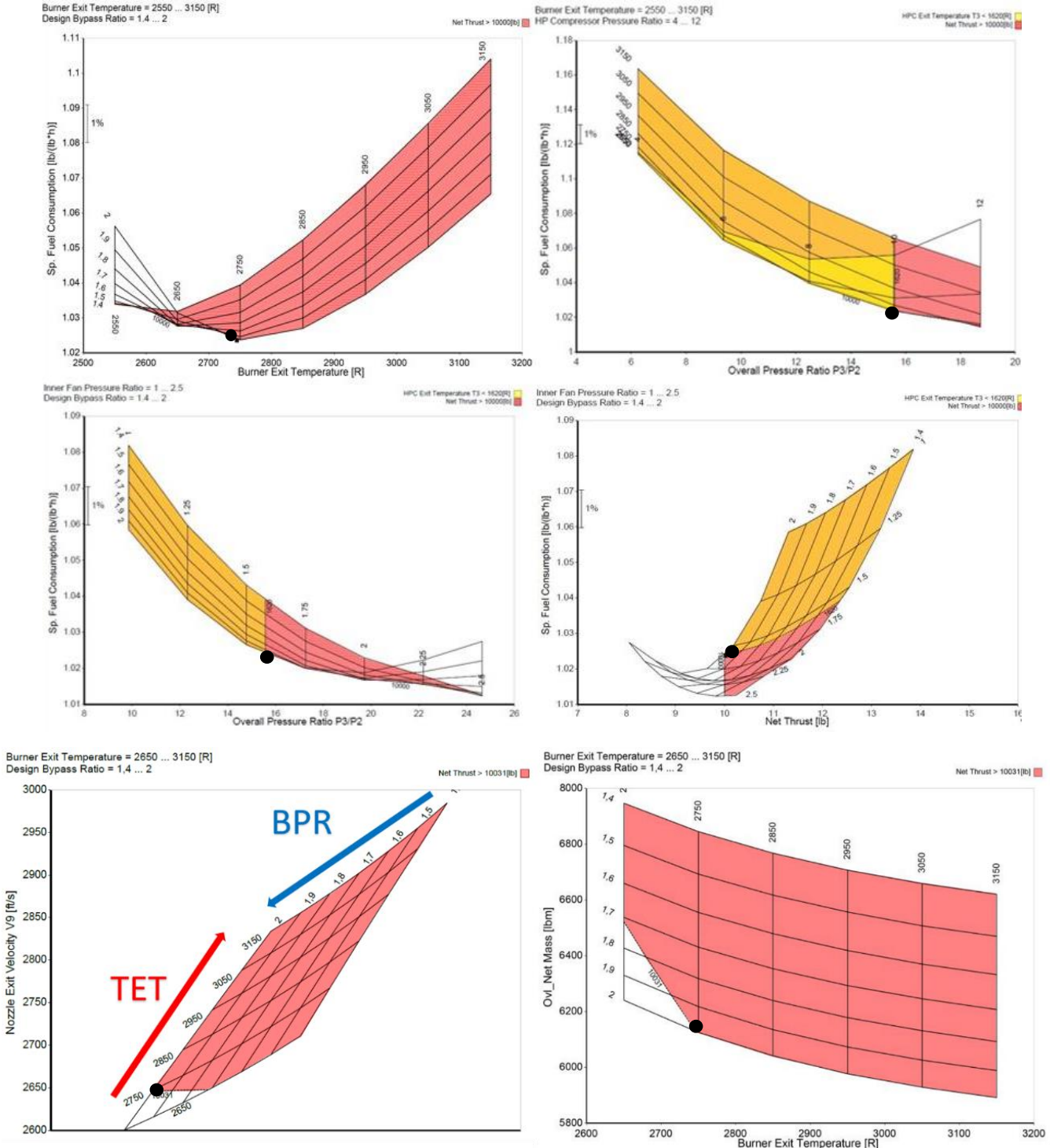


Figure 6. Parametric Studies of PHOENIX Engine

Although the engine net mass decreases with the increase of TET, TET should be increased in a controlled manner to improve TSFC. TSFC decreases with the increase of OPR, but the T3 limit of 1620 R also limits the increase of OPR. When the TSFC-OPR graphs are examined, it is clearly seen that Phoenix has the maximum OPR value that can be obtained by staying below the T3 limit. The minimum TSFC in the created space is provided in this way. The red zone symbolizes the minimum requirement thrust and the yellow zone where the T3 limit is not exceeded. The intersection of the red and yellow regions is represented by orange.

Station	W lb/s	T R	P psia	WRstd lb/s	FN	=	10044,43 lb	
amb		398,97	1,456					
1	494,327	717,90	11,402					
2	494,327	717,90	10,683	800,000	TSFC	=	1,0239 lb/(lb*h)	
13	329,116	852,84	18,578	333,846	WF Burner	=	2,85669 lb/s	
21	165,211	827,97	16,835	182,216	s NOX	=	1,1228	
25	165,211	827,97	16,667	184,057	BPR	=	1,9921	
3	164,291	1619,64	165,968	25,707	Core Eff	=	0,6266	
31	153,901	1619,64	165,968		Prop Eff	=	0,8584	
4	156,758	2744,74	159,329	33,261	P3/P2	=	15,535	
40	158,690	2731,97	159,329		NGV	=	2 Stage HPT	
41	163,638	2700,59	159,329	34,440	P16/P6	=	1,09321	
43	163,638	1996,73	38,750		A63	=	1333,20 in ²	
44	165,667	1992,34	38,750		A163	=	1309,54 in ²	
45	166,289	1988,38	38,362	124,727	A64	=	2642,74 in ²	
49	166,289	1657,74	16,994		XM63	=	0,36834	
5	166,587	1657,15	16,994	257,506	XM163	=	0,51312	
6	166,587	1657,15	16,824		XM64	=	0,45000	
16	329,116	852,84	18,392		P63/P6	=	0,99000	
64	495,704	1136,32	17,387		P163/P16	=	0,99000	
8	495,704	1136,32	17,387	620,155	A8	=	1913,99 in ²	
Bleed	1,480	1619,64	165,968		CDB	=	0,95000	

Efficiencies:	isent	polytr	RNI	P/P	Anq8	=	25,00 °	
Outer LPC	0,8957	0,9034	0,494	1,739	P8/Pamb	=	11,94014	
Inner LPC	0,8899	0,8966	0,494	1,576	WLKBy/W25	=	0,00000	
HP Compressor	0,8986	0,9239	0,649	9,958	WCHN/W25	=	0,04164	
Burner	0,9995			0,960	WCHR/W25	=	0,01228	
HP Turbine	0,9230	0,9099	1,578	4,112	Loading	=	100,00 %	
LP Turbine	0,9205	0,9128	0,539	2,257	WCLN/W25	=	0,00376	
Mixer	0,6500				WCLR/W25	=	0,00181	

HP Spool mech Eff	0,9900	Nom Spd	11500 rpm		WBHD/W21	=	0,00000	
LP Spool mech Eff	0,9900	Nom Spd	7500 rpm		far7	=	0,00580	

P2/P1=	0,9370	P25/P21=	0,9900	P45/P44=	0,9900	WBLD/W25	=	0,00896
Con-Di Nozzle:					FWX	=	100,0 hp	
A9*(Ps9-Pamb)		21,929			P16/P13	=	0,9900	

hum [%]	war0	FHV	Fuel		P6/P5	=	0,9900	
0,0	0,00000	18552,4	Generic		A9/A8	=	2,14433	

					CFGid	=	0,98403	

Figure 7. PHOENIX Engine Performance at Cruise Condition

3.6. Off-Design Analysis of ETU-PHOENIX

Station	W lb/s	T R	P psia	WRstd lb/s	FN	=	33598,89 lb	Station	W lb/s	T R	P psia	WRstd lb/s	FN	=	13610,50 lb		
amb		536,67	14,696					amb		398,97	3,142						
1	1268,416	546,44	15,655		TSFC	=	0,7817 lb/(lb*h)	1	480,984	514,12	7,623						
2	1268,416	546,44	15,436	1239,487	WF Burner	=	7,29597 lb/s	13	480,984	514,12	7,516	936,352					
13	844,434	735,32	39,860	370,696	s NOX	=	1,0142	21	303,113	663,39	16,500	305,325					
21	423,982	704,14	34,469	210,623	BPR	=	1,9917	25	177,871	637,58	14,517	199,645					
25	423,983	704,14	34,008	213,476	Core Eff	=	0,4311	3	176,880	1359,76	171,404	24,555					
3	421,622	1461,94	397,187	26,191	Prop Eff	=	0,4475	31	165,808	1359,76	171,404						
31	397,278	1461,94	397,187		P3/P2	=	25,731	4	168,981	2553,56	165,140	33,366					
4	404,574	2598,14	380,502	34,972	P5/P2	=	1,4561 EFR	40	171,061	2540,16	165,140						
40	409,531	2585,34	380,502		NGV	=	2 Stage HPT	41	176,388	2507,09	165,140	34,511					
41	422,230	2553,88	380,502	36,186	P16/P6	=	2,31578	43	176,388	1875,02	39,641						
43	422,230	1898,94	91,466		A63	=	1333,20 in ²	44	178,573	1869,06	39,641						
44	427,438	1893,99	91,466		A163	=	1309,54 in ²	45	179,242	1864,89	39,228	127,328					
45	429,033	1879,98	80,999	149,862	A64	=	2642,74 in ²	49	179,242	1536,14	16,159						
49	429,033	1413,59	22,476	463,861	XM63	=	1,00000	5	179,564	1535,36	15,966	280,974					
5	429,799	1413,16	22,476		XM163	=	1,00000	6	179,564	1535,36	15,966						
6	429,799	1413,16	14,454		XM64	=	1,00000	16	303,113	663,39	16,362						
16	844,434	735,32	33,471		P63/P6	=	0,92309	64	482,677	1002,90	15,879						
64	1274,233	973,17	22,313		P163/P16	=	0,98286	8	482,677	1002,91	15,879	621,176					
8	1274,233	973,17	22,313	1149,581	A8	=	3445,18 in ²	Bleed	1,480	1359,76	171,405						
Bleed	1,480	1461,94	397,187		CDB	=	0,95000										

Efficiencies:	isent	polytr	RNI	P/P	P8/Pamb	=	1,51830	Efficiencies:	isent	polytr	RNI	P/P	P8/Pamb	=	5,05393		
Outer LPC	0,8963	0,9091	0,987	2,582	WLKBy/W25	=	0,00000	Outer LPC	0,8653	0,8792	0,517	2,195	WLKBy/W25	=	0,00000		
Inner LPC	0,8906	0,9022	0,987	2,233	WCHN/W25	=	0,04164	Inner LPC	0,8596	0,8719	0,517	1,931	WCHN/W25	=	0,04164		
HP Compressor	0,8932	0,9217	1,608	11,679	WCHR/W25	=	0,01228	HP Compressor	0,8704	0,9055	0,763	11,951	WCHR/W25	=	0,01228		
Burner	0,9997			0,958	Loading	=	71,87 %	Burner	0,9989			0,963	Loading	=	164,50 %		
HP Turbine	0,9086	0,8931	4,018	4,160	WCLN/W25	=	0,00376	HP Turbine	0,8784	0,8586	1,781	4,166	WCLN/W25	=	0,00376		
LP Turbine	0,9139	0,9002	1,201	3,564	WCLR/W25	=	0,00181	LP Turbine	0,8945	0,8834	0,594	2,428	WCLR/W25	=	0,00181		
Mixer	0,6500				WBHD/W21	=	0,00000	Mixer	0,6500				WBHD/W21	=	0,00000		

HP Spool mech Eff	0,9900	Nom Spd	11012 rpm		far7	=	0,00576	HP Spool mech Eff	0,9900	Nom Spd	10554 rpm		far7	=	0,00662		
LP Spool mech Eff	0,9900	Nom Spd	8653 rpm		WBLD/W25	=	0,00349	LP Spool mech Eff	0,9900	Nom Spd	7598 rpm		WBLD/W25	=	0,00832		

P2/P1=	0,9860	P25/P21=	0,9866	P45/P44=	0,9757	FWX	=	100,0 hp	P2/P1=	0,9860	P25/P21=	0,9880	P45/P44=	0,9896	P16/P13	=	0,9916
Con-Di Nozzle:						P16/P13	=	0,8397	Con-Di Nozzle:						P6/P5	=	0,9881
A9*(Ps9-Pamb)		0,000				A9/A8	=	1,00000	A9*(Ps9-Pamb)		84,659				A9/A8	=	1,35000

hum [%]	war0	FHV	Fuel		CFGid	=	1,90000	hum [%]	war0	FHV	Fuel			CFGid	=	0,98028	
0,0	0,00000	18552,4	Generic					0,0	0,00000	18552,4	Generic						

Figure 8. PHOENIX Engine Performance at Takeoff (left) and Supersonic Climb (right) Conditions

Necessary changes are made to the On Design conditions to design an engine that also meets the limits of the Off-Design conditions. Thus, the engine is designed with an iterative study between Off-Design and On-Design. It was said that the engine's operability at different flight phases, which are other operating conditions, was examined thanks to the Off-Design analysis.

At the Off-Design point, the most important limitation was the exhaust exit temperature. This limit was that the exhaust exit temperature should not exceed 1150 ft/s. By changing the modifiers in the Off-Design tool of the GasTurb 13 program, the operability of the engine designed in On-Design was examined in takeoff. Compressor and turbine maps are scaled with modifiers. Takeoff and Climb outputs, which provide the required thrust and within limits, are given in Figure 8. Compressor and Turbine maps are also given in Figure 9.

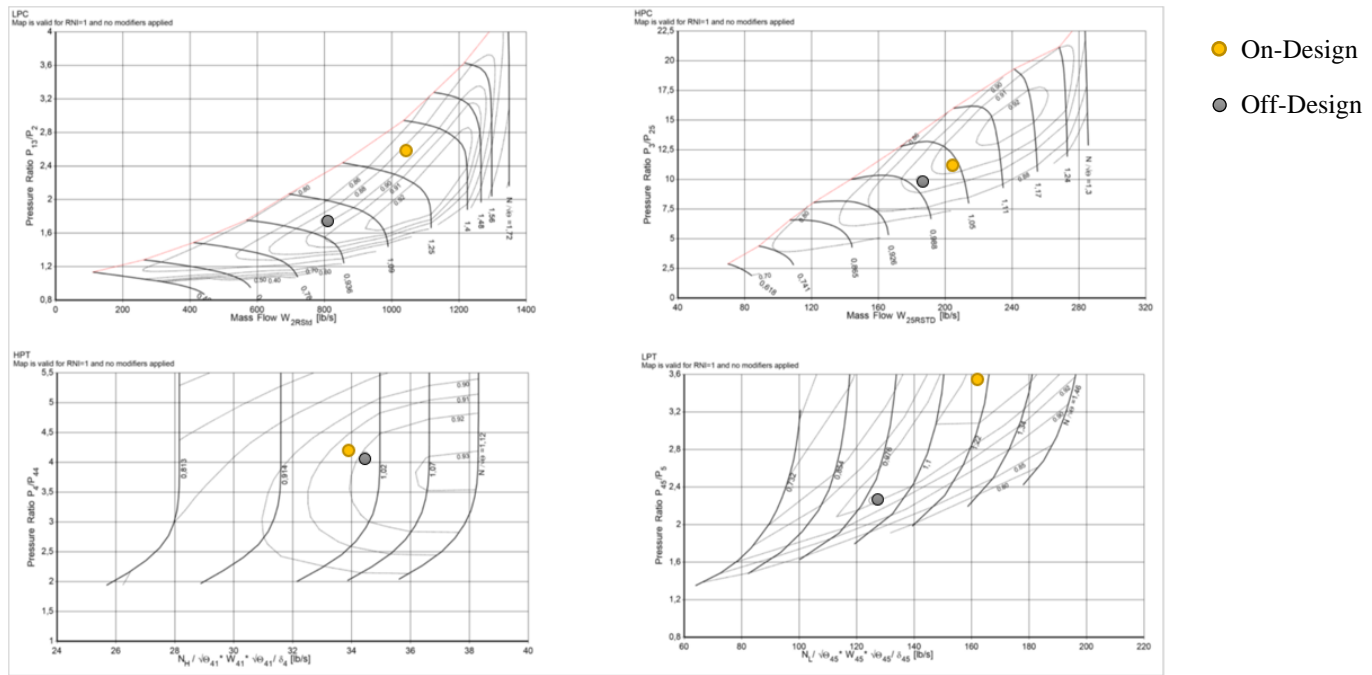


Figure 9. Compressor and Turbine Maps Generated ETU-PHOENIX Performance Team

Surge Margin is the distance of the design (operating) point from the surge line. For an ideal design, the surge margin should exceed 10% limits. The 0-10% surge margin range is assumed as a critical range for compressor design [14]. When the maps are examined, it is clearly seen that the design points of PHOENIX are far from the Surge Margin.

In the detailed output of the takeoff condition given in Figure 10, the engine exit velocity, which was limited to 1150 ft/s, is satisfied.

	Units	St 2	St 21	St 25	St 3	St 4	St 44	St 45	St 5	St 6	St 13	St 16	St 64	St 8	St 9
Mass Flow	lb/s	1268.42	423,982	423,983	421,622	404,574	427,438	429,033	429,799	429,799	844,434	844,434	1274.23	1274.23	1274.23
Total Temperature	R	546,439	704,139	704,139	1461,94	2598,14	1883,99	1879,98	1413,16	1413,16	735,323	735,322	973,167	973,166	973,166
Static Temperature	R	455,255	640,078	652,96	1429,9	2559,59	1779,01	1753,06	1201,54	1201,54	672,904	702,124	816,374	867,239	867,261
Total Pressure	psia	15,4363	34,4686	34,008	397,187	380,502	91,466	80,0988	22,4762	14,4536	39,8602	33,4714	22,3128	22,3128	22,3128
Static Pressure	psia	8,15331	24,6573	26,0912	364,765	356,602	72,293	60,1842	12,0344	7,73887	29,1636	28,4318	11,835	14,6934	14,6969
Velocity	ft/s	1046,18	879,018	785,684	650,085	757,914	1216,19	1335,17	1673,26	1673,26	868,992	634,593	1394,35	1148,51	1148,56
Area	in ²	2608,08	668,011	720,514	135,642	204,414	461,42	499,362	908,84	1680,54	1196,22	1753,19	2642,74	3493,63	3493,63
Mach Number		1	0,709432	0,627895	0,356573	0,316937	0,604344	0,668046	1	1	0,68423	0,489293	1	0,799696	0,799772
Density	lb/r ³	0,048338	0,103974	0,10785	0,688527	0,376037	0,109682	0,092662	0,027034	0,017384	0,116977	0,109296	0,039129	0,04573	0,045735
Spec Heat @ T	BTU/(lb*R)	0,240227	0,242049	0,242049	0,263242	0,29757	0,282329	0,282196	0,268216	0,268216	0,242558	0,242558	0,249906	0,249906	0,249906
Spec Heat @ Ts	BTU/(lb*R)	0,239883	0,241309	0,241458	0,282276	0,296955	0,279525	0,278744	0,260983	0,260983	0,241688	0,242026	0,245855	0,247003	0,247004
Enthalpy @ T	BTU/lb	2,35051	40,3619	40,3619	231,153	560,84	352,734	351,573	222,902	222,902	47,9241	47,9239	106,944	106,944	106,944
Enthalpy @ Ts	BTU/lb	-19,5217	24,9208	28,0258	222,708	549,36	323,175	315,948	166,951	166,951	32,8333	39,8763	68,0908	80,5833	80,5936
Entropy Function @ T		0,063248	0,953669	0,953669	3,62027	6,08051	4,71461	4,70547	3,56018	3,56018	1,10679	1,10679	2,12112	2,12112	2,12112
Entropy Function @ Ts		-0,575049	0,618695	0,688669	3,53511	6,01564	4,47937	4,41962	2,93549	2,93549	0,794332	0,943607	1,48702	1,70335	1,70353
Exergy	BTU/lb	1,83141	36,636	36,1408	219,245	456,767	246,467	240,755	107,463	91,2071	43,9115	37,4795	44,2214	44,2214	44,2214
Gas Constant	BTU/(lb*R)	0,068607	0,068607	0,068607	0,068607	0,068606	0,068606	0,068606	0,068606	0,068606	0,068607	0,068607	0,068606	0,068606	0,068606
Fuel-Air-Ratio		0	0	0	0	0,018365	0,017365	0,0173	0,017268	0,017268	0	0	5,7587E-3	5,7587E-3	5,7587E-3
Water-Air-Ratio		0	0	0	0	0	0	0	0	0	0	0	0	0	0

Figure 10. Detailed Output of Take-off Condition

As with the base engine, fuel consumption values were calculated for PHOENIX in each flight phase in the mission profile. Using GasTurb 13's Mission tool, TSFC values were calculated for the conditions of pre-determined flight phases. PHOENIX's total fuel consumption is given in Table 7.

Table 7. Total Fuel Consumption of PHOENIX (per engine)

Segment	Altitude (ft)	Mach Number[5]	Thrust (lbf)	TSFC (lbm/lbf*h)	Fuel Flow (lbm/min)	Time (min)	Fuel Burned in Segment (lbm)
Taxi Out	0	0.019	2351[5.6]	0.7818	30.64 [6]	15 [7]	459.6
Take Off	0	0.302	33600	0.7817	437.71	1.0	437.7
Subsonic Climb	17750	0.7	22178	0.6999	287.97	6	1727.8
Subsonic Cruise	33000	0.95	15186	0.7557	203.84	30	6115.2
Supersonic Climb	40000	1.2	13612	0.8393	190.35	20	3806.9
Supersonic Cruise	53000	2.01	10044	1.0240	171.43	100	7776.0
Supersonic Descend	45000	1.4	8413	0.8445	143.19	10	17143
Subsonic Cruise	42000	0.95	8526	0.7453	120.2	20	2404
Subsonic Descend	22500	0.6	16142	0.6407	204.23	7.5	1531.7
Approach & Touchdown	1500	0.24	23000 [8]	0.6851	262.62	7.5[9]	1969.7
Taxi In	0	0.019	2351	0.7818	30.64 [6]	6[7]	183.8
TOTAL						Approx. 4hr	37211.5 [10]

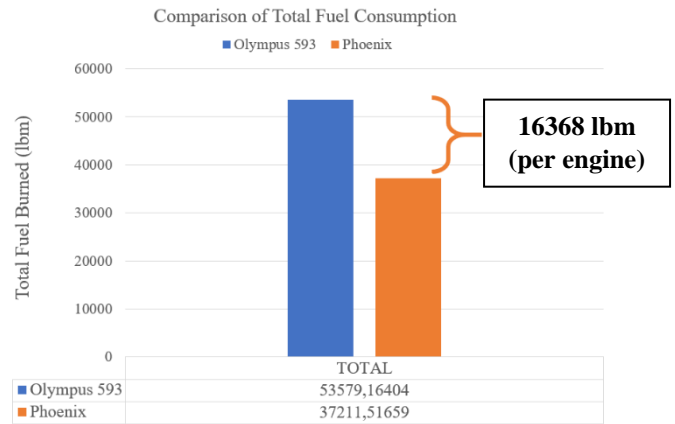
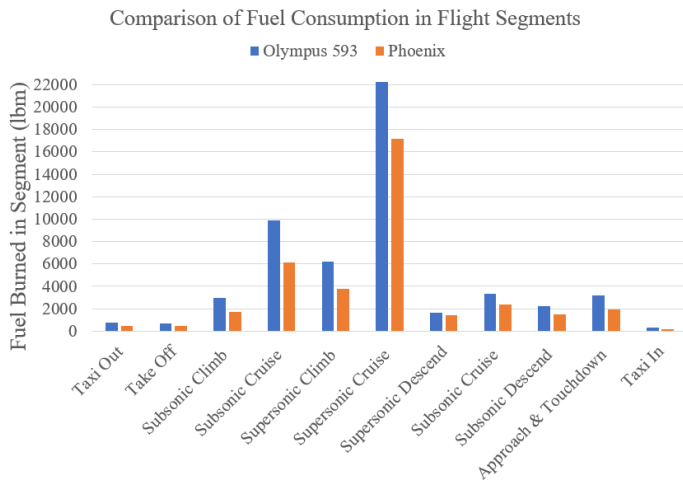


Figure 11. Comparison of Fuel Consumption in Each Segment (Left) and Comparison of Fuel Consumption (Right)

When the base engine and Phoenix are compared, it is seen that the total fuel consumption has decreased by 30%. TSFC is kept in a minimum value within limits with the trade study done On-Design. According to the mission profile created, the graph showing the fuel consumption of Olympus 593 and PHOENIX in each flight phase is given in Figure 11 (Left) and the graph showing the total fuel consumption is given in Figure 11 (Right). A comparison of the Table 8 base engine and PHOENIX is given below.

Table 8. Comparison of Base Engine and PHOENIX

	Base Engine Olympus 593	PHOENIX	Limitations and Improvement
Engine Type	Turbojet	Low-Bypass Mixed Turbofan	Satisfied
Axial Compressor Stage Number	7 HPC+7 LPC	1 Fan+5 HPC	-
Axial Turbine Stage Number	2 HPT+2 LPT	2 HPT+1 LPT	-
Cruise Thrust (lbf)	10031	10044	Satisfied
Takeoff Thrust (lbf)	33618	33610	Satisfied
Cruise TSFC (lbm/lbf*h)	1.3304	1.02	23 % Improvement
Takeoff TSFC (lbm/lbf*h)	1.2576	0.78	38 % Improvement
Cruise OPR	11.8	15.5	-
Takeoff OPR	16	25.7	-
Cruise T4 (R)	2430	2745	Limitation Satisfied
Cruise T3 (R)	1538	1620	Limitation Satisfied
Cruise BPR	-	1.99	-
Nozzle Exit Velocity (ft/sec)	-	1148	Limitation Satisfied
Max. Engine Dia. (in)	48	65	-
Engine Length (in)	159	156	2% Improvement
Reheat	YES	NO	Satisfied

4. SUPERSONIC INLET DESIGN

For engine performance and obtaining net power output, supersonic intake is one of the crucial components of the engine due to achieve minimum total pressure loss by decreasing the pressure of the freestream air. In order to obtain minimum total pressure loss, different intake options should include supplying sufficient mass flow to the engine face with an appropriate velocity, minimizing total mass as much as possible due to flight efficiency, providing well integration of the fuselage to minimize high installation drag and inducing proper acoustic absorption of fan noise to achieve less-noisy engine [14].

4.1. Selection of Supersonic Intake

While designing a supersonic intake, the decisions are generally made by considering the flight speed of on design point. Mixed compression intake is referred to as the best choice compared between pitot type (internal compression) and external compression intake. Another important point is related to the shape of the intake, which could be made between annular and rectangular supersonic intake. Rectangular supersonic intake provides less distortion at a high angle of attack with better geometry possibilities and lowers the jeopardy of the surge in asymmetric flow compared to annular supersonic intake which is more beneficial in terms of less total pressure loss and weight. In the light of the given information, it is decided to design a rectangular mixed compression intake for PHOENIX Engine. Furthermore, as stated in the request for proposal, Concorde's existing intake was retained which was rectangular variable mixed compression intake [14,15]. In addition, shocks and external ramp numbers are quite essential for the design. An increment in ramp number does not raise pressure recovery dramatically, causing to select 2-ramp intake instead of 4-ramp intake which could be noticed in Figure 12.

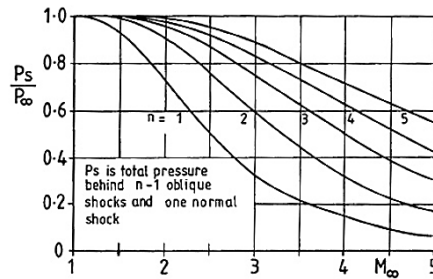


Figure 12. Relationship between Total Pressure Recovery and Freestream Velocity [14]

The working principles of the Concorde's intake which contains a bleed system at the throat is given in Figure 13.

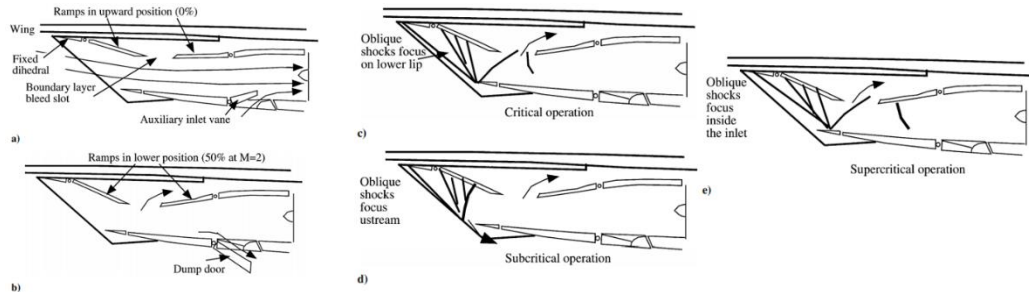


Figure 13. Modes of Operation: a) (at $M < 1.3$), b) (at $M > 1.3$), c) at Critical Flow Regime Under Cruise Conditions, d) at Subcritical Regime Under Cruise Conditions, and e) at Supercritical Regime Under Cruise Conditions (Concorde flight manual) [20]

4.2 Details of Supersonic Intake Design

2-D schematic of the 2-ramp mixed compression inlet which has two external shocks, one internal oblique shock and one normal internal shock, is represented in Figure 14 where θ and δ represent the shock wave angles and the ramp angles, respectively, number 1,2,3 represents oblique shocks and number 4 represents the normal shock. Inlet consists of 3 sections which are external supersonic diffuser, throat, and internal subsonic diffuser.

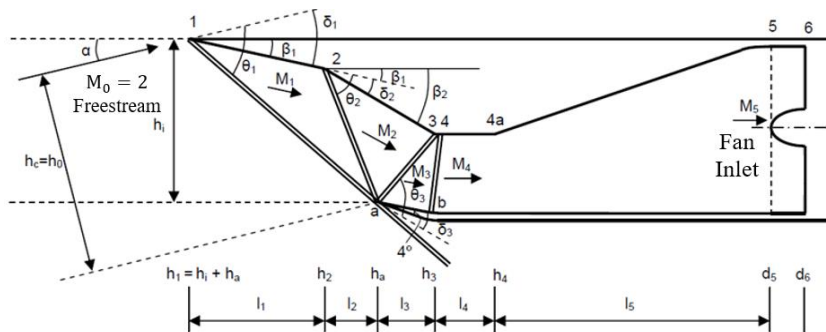


Figure 14. Sketch of a Mixed Compression Intake [15]

Calculations of shock angle (θ), ramp angle (δ), other dimensions and some properties of the free stream were performed from the developed MATLAB code, including the equations given below.

$$M_n^2 = \frac{(\gamma + 1)^2 M_{n-1}^4 \sin^2(\theta_n) - 4(M_{n-1}^2 \sin^2(\theta_n) - 1)(\gamma M_{n-1}^2 \sin^2(\theta_n) + 1)}{[2M_{n-1}^2 \sin^2(\theta_n) - (\gamma - 1)][(\gamma - 1)M_{n-1}^2 \sin^2(\theta_n) + 2]} \quad (4.1)$$

$$\tan \delta_n = \frac{2 \cot \theta_n (M_{n-1}^2 \sin^2(\theta_n) - 1)}{2 + M_{n-1}^2 (\gamma + 1 - 2 \sin^2(\theta_n))} \quad (4.2)$$

$$M_1 \sin^2(\theta_1) = M_2 \sin^2(\theta_2) = \dots = M_n \sin^2(\theta_n) \quad (4.3)$$

$$PR_n = \left[\frac{(\gamma + 1) M_{n-1}^2 \sin^2(\theta_n)}{(\gamma - 1) M_{n-1}^2 \sin^2(\theta_n) + 2} \right]^{\frac{\gamma}{\gamma - 1}} \left[\frac{(\gamma + 1)}{2\gamma M_{n-1}^2 \sin^2(\theta_n) - (\gamma - 1)} \right]^{\frac{1}{\gamma - 1}} \quad (4.4)$$

$$PRF = \prod_{i=1}^4 PR_i * PR_{sub} \quad (4.5)$$

In Table 9, parameters in cruise condition used as inputs in MATLAB code are given.

Table 9. Inlet Variables and Values Used in MATLAB

Parameters	Values	Parameters	Values
Freestream Mach Number (M_0) (for cruise)	2.01	Hub to Tip Ratio (h/t)	0.3
Freestream Static Temperature (R)	390	Engine Face Diameter (D_{fan}) (in)	58.39
Freestream Static Pressure (psi)	1.456	Engine Face Mass Flow Rate (W_{eng}) (lb/s)	494
Freestream Density (lb/in ³)	6.01×10^{-6}	Up-Stream Mach Number of Normal Shock	1.21
Gas Constant (ft.lb/slug.R)	1717	Diffuser Duct Angle (degree)	12.27
Specific Heat Ratio (γ)	1.4	Cowl Lip Angle (degree)	9.01
Fan Entry Mach Number (M_6)	0.67	Subsonic Diffuser Efficiency	0.92

In order to solve oblique and normal shock relations, a normal shock upstream Mach number has to be estimated. Otherwise, the number of unknown variables would be more than the number of equations [16]. In order to calculate dimensions and flow properties, the upstream Mach number must be picked according to Figure 15-right. Pressure recovery factor with corresponding normal shock upstream Mach number estimation is given in Figure 15-right. However, experimental results show that the pressure recovery factor could not exceed the value of 0.9, pressure recovery factor which has a value of 0.936 for cruise condition, is retained as stated in the request for proposal and 1.21 Mach number estimation is made to satisfy maximum pressure recovery factor which is chosen as 0.944 [18,19]. By considering MIL-E-5007 Standard, pressure recovery factor vs. Mach number and pressure recovery factor vs. up-stream Mach number is plotted in Figure 15.

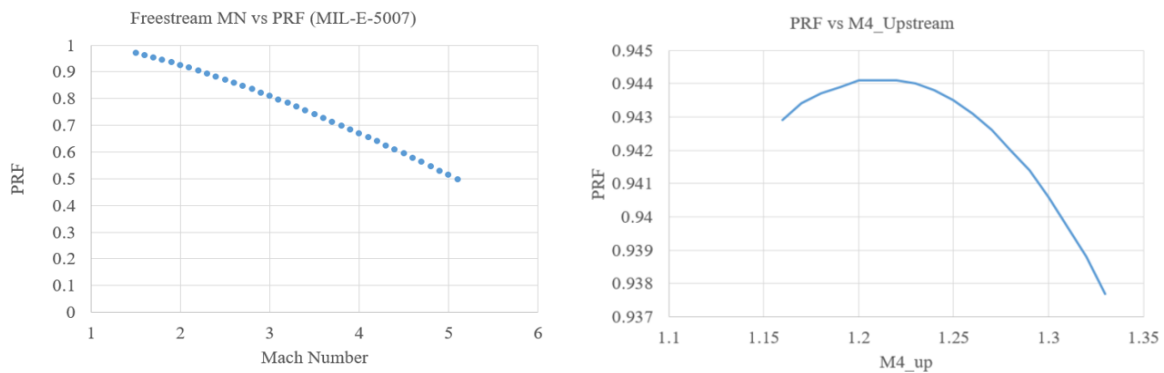


Figure 15. Pressure Recovery Factor vs Mach Number (MIL-E-5007 Standard) (left), Pressure Recovery Factor vs Up-Stream Mach Number (right)

Table 10. Geometrical Results of the Intake

Dimensions	Values (in)
First Ramp Length (L_1)	29.52
Second Ramp Length (L_2+L_3)	75.71
Throat Length (L_4)	62.67
Subsonic Diffuser Length (L_5)	99.84
Throat Height (H_4)	34.79
Engine Face Diameter (D_6)	58.3
Total Intake Length (Top)	267.79
Total Intake Length (Bottom)	204.45

Table 11. Mach Numbers, Shock and Ramp Angles of Each Stages

Parameter	θ_1	θ_2	θ_3	δ_1	δ_2	δ_3
Ramp Angles	36.11°	42.42°	52.51°	7.09°	7.62°	7.75°
Mach Number	M_0	M_1	M_2	M_3	M_4	M_5
	2.01	1.76	1.49	1.21	0.84	0.67

By using inviscid relations in the MATLAB code, the intake dimensions, Mach numbers obtained from each station, shock and ramp angles and are calculated which are stated in Table 10 and Table 11 for supersonic cruise condition, respectively.

4.3. Verification of Supersonic Intake at On-Design with Computational Fluid Dynamics

2-D Computational fluid dynamics analyses were performed using Star CCM+ software to validate the performance of the intake. Boundary conditions were determined from GasTurb 13 and for the analyses, SST k- ω turbulence model was selected and trimmer mesh with 140 000 cells in the domain was generated. Freestream boundary condition was set as 53 000 ft altitude and Mach 2. Fan inlet boundary was set as pressure outlet boundary condition, which is 7.912 psi static pressure and 659 Rankine static temperature.

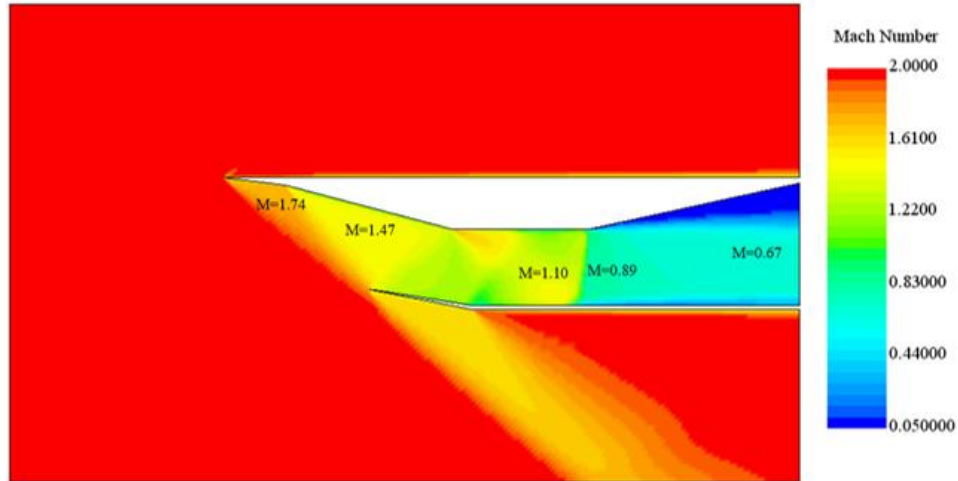


Figure 16. Mach Number Contours

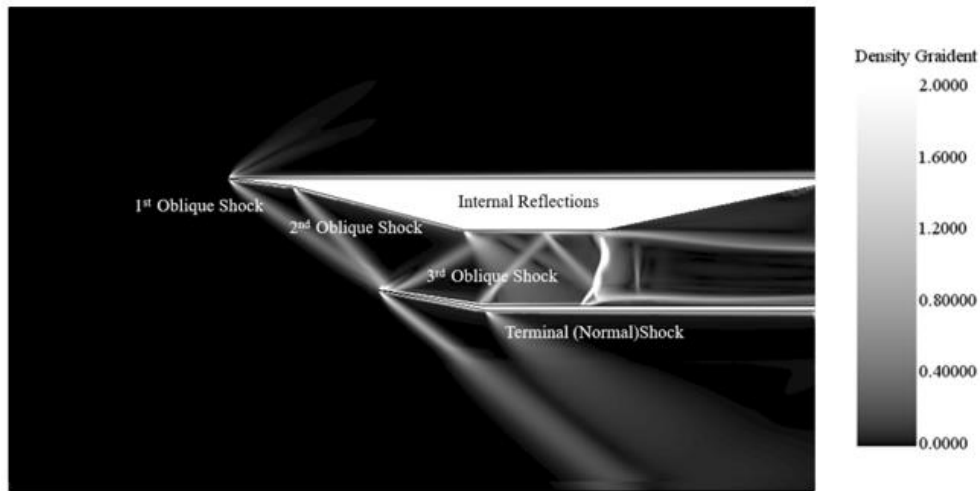


Figure 17. Density Gradient Contours

Computational fluid dynamics analysis shows, Figures 16-17, that first and second oblique shocks touch the cowl lip and are reflected by the lip again which continues to reflect in the throat. The terminal shock was obtained right before the subsonic diffuser. After external and internal shocks, the Mach number is investigated and a comparison of MATLAB outputs and CFD results are given in Table 12. In addition, PRF comparison between MIL-E-5007 Standard, MATLAB code and CFD could also be found in Table 13. A MATLAB code called PHOENIX-INTAKE was written by the team for the design of supersonic intake using oblique and normal relations.

Table 12. Mach Number at Stages

Method	M ₀	M ₁	M ₂	M ₃	M ₄	M ₅
MATLAB	2.01	1.76	1.49	1.21	0.84	0.67
CFD	2.01	1.74	1.47	1.10	0.89	0.67

Table 13. PRF Result Comparison

	CFD	RFP	PHOENIX-INTAKE	MIL-E-5007	Difference %
PRF	0.89	0.936	0.94	0.92	5.6

Using geometrical outputs from the MATLAB code, 3-D geometry of supersonic intake is created which is shown in Figure 18.

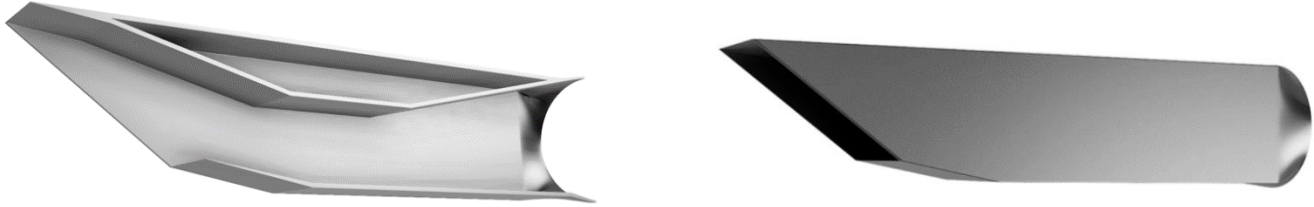


Figure 18. 3-D CAD Model of Supersonic Intake

4.4. Supersonic Intake Off Design Performance

Ramp angles could be changed in different flight segments, including various altitude and flight speeds of mixed compression supersonic inlet. Ramp angles ($\delta_{1,2,3}$) and mass flow properties for three key flight segments are described in detail in Table 14.

Table 14. Variable Ramp Angles for Off-Design Conditions

Segment	Altitude(ft)	Mach Number	Mass Flow Ratio	Mass Flow Rate (lb/s)	δ_1	δ_2	δ_3
Take Off	0	0.302	1	1268	0	0	0
Supersonic Climb	40000	1.2	0.72	481	0.05	0.05	0.04
Supersonic Cruise	53000	2.01	0.95	494.4	7.1	7.6	7.7

At off-design conditions, the terminal shock could not stay downstream or throat. Instead of staying downstream, terminal shock moves upstream and even it can spill over from the lip which would cause huge boundary layer separation at the upstream of the intake and flow distortion at the face of the engine. This phenomenon is called an unstart intake or buzz of the inlet. Due to this, there is a possibility that a compressor stall could occur. Therefore, distortion, buzz must be avoided to stay in the safe zone for the compressor. This condition is called a subcritical shock which could be seen in Figure 13 [14,17,18].

5. AERODYNAMIC DESIGN OF THE TURBOMACHINERY SYSTEM

This section includes detailed information about the PHOENIX's low-pressure (fan), high-pressure compressor, high-pressure turbine, and low-pressure turbine designs. For this purpose, initially, the thermodynamic properties and geometrical constraints are determined which were implemented as boundary conditions for the design by using AxSTREAM software. Furthermore, 1-D and 2-D analyses were performed in AxSTREAM software after obtaining total temperature, total pressure, and mass flow rate by using GasTurb 13.

After the 1-D and 2-D analyses were completed, the crucial design parameters such as averaged flow and work coefficients, De-Haller number, diffusion factor, aspect ratios, solidities, chord dimensions, Zweifel coefficient for turbine design were checked and compared with the typical values which were obtained from the literature survey, the process was followed to acquire 3-D blade geometries of each stage of the turbomachinery system. Since time duration is given for the design, 3-D numerical calculations, computational fluid dynamics analyses could not be performed.

5.1. Design Guidelines for Compressors and Technological Limitations

Since the compressor has more design parameters than the other gas turbine components, designing it to the most suitable conditions and constraints is a difficult and complicated operation. As a result, an iterative approach must be followed, with theoretical estimations based on certain assumptions being used in particular to simplify the preliminary design process [14,21,22].

In the aviation industry, two types of compressors are used in aviation which are axial compressors and radial, axial compressors. Although radial compressors have higher stage pressure ratios, axial compressors operate with larger mass flow rates. For higher pressure ratios axial compressor is a better candidate. Moreover, axial compressor efficiencies are greater than the radial compressors and axial compressors are more suitable for high volume engines. The axial compressor is selected for PHOENIX Engine.

In turbomachinery design, the isentropic efficiencies of the components are important and must be held on a higher value remaining on the technological limitations. Components and their technological developments could be seen in Table 15 [14].

Table 15. Technological Developments of the Turbomachinery Components for given Time Periods [14]

Component	Figure of Merit	Type	Level of Technology	
			Level 1 (1985 - 2005)	Level 2 (2005 - 2025) (Projected)
Fan	e_{fan}		~0.86	$e_{fan} \geq 0.89$
Compressor	$e_{compressor}$		~0.88	$e_{compressor} \geq 0.9$
Turbine	$(e_{turbine})_{uncooled}$	Uncooled	~0.89	$(e_{turbine})_{uncooled} \geq 0.9$
	$(e_{turbine})_{cooled}$	Cooled	~0.87	$(e_{turbine})_{cooled} \geq 0.89$

In order to design low-pressure and high-pressure axial compressors, some guiding criteria must be followed. Table 16, which includes ranges of some of the important design parameters and its typical values for axial compressors, is given below.

Table 16. Guidelines on the Ranges and Typical Values of Compressor Parameters [14,21]

Parameter	Range of Values	Typical Value	Parameter	Range of Values	Typical Value
Flow Coefficient, ϕ	$0.3 \leq \phi \leq 0.9$	0.6	Tip Rotational Speed, ω_{rt}	$450 \leq \omega_{rt} \leq 500$ m/s	500 m/s
Axial Mach Number, M_z	$0.3 \leq M_z \leq 0.6$	0.55	De Haller Criterion, W_2 / W_1	$W_2 / W_1 \geq 0.72$	0.75
Degree of Reaction, ${}^\circ R$	$0.1 \leq {}^\circ R \leq 0.90$	0.5 (for $M < 1$)	Compressor Pressure Ratio per Spool	$\Pi_c < 20$	up to 20
D-Factor, D	$D \leq 0.6$	0.45	Aspect Ratio, Fan	~2- 5	< 1.5
Tip Tangential Mach Number, M_T	1.0-1.5	1.3	Aspect Ratio, Compressor	~1- 4	~ 2
Reynolds Number Based on Chord, Re_c	$300,000 \leq Re_c$	>500,000	DCA Blade (Range)	$0.8 \leq M \leq 1.2$	Same
Stage Average Aspect Ratio, AR	$1.0 \leq AR \leq 4.0$	< 2.0	Axial Gap Between Blade Rows	$0.23c_z$ to $0.25c_z$	$0.25c_z$
Stage Average Solidity, σ	$1.0 \leq \sigma \leq 2.0$	1.4	NACA-65 Series (Range)	$M \leq 0.8$	Same
Loading Coefficient, ψ	$0.2 \leq \psi \leq 0.5$	0.35	Taper Ratio	~ 0.8- 1.0	0.8
Polytropic Efficiency, e_c	$0.85 \leq e_c \leq 0.92$	0.9	Pressure Ratio for One Stage	1.5- 2.0	Same
Tip Relative Mach Number (1 st Rotor), $(M_{1r})_{tip}$	$(M_{1r})_{tip} \leq 1.7$	1.3-1.5	Hub/Tip Ratio at Inlet, Compressor	0.6 – 0.75	Same
Hub Rotational Speed, ω_{rh}	$\omega_{rh} \leq 380$ m/s	300 m/s	Hub/Tip Ratio at Outlet, Compressor	0.9 -0.92	Same

In light of the information given above, the design of the low-pressure and high-pressure compressors was conducted. Since the maximum pressures and temperatures for the turbomachinery parts are obtained at supersonic cruise, all turbomachinery components are designed based on performance analysis results obtained at supersonic cruise.

5.2. Detailed Low-Pressure (Fan) and High-Pressure Compressor Design

PHOENIX Engine has 1 stage axial low-pressure compressor (fan) and 5 high-pressure stage compressor. The design process is conducted by using AxSTREAM software. AxSTREAM provides design choices by considering polytropic efficiency as a function of work and flow coefficients. As boundary conditions, the thermodynamic properties and geometrical dimensions of the low-pressure and high-pressure compressors obtained using the GasTurb 13 are given in Table 17.

Table 17. Thermodynamic and Geometrical Properties of Low-Pressure and High-Pressure Compressors

Low-Pressure Compressor				High-Pressure Compressor			
Thermodynamic and Geometrical Properties				Thermodynamic and Geometrical Properties			
$(P_{total})_{inlet}$ [psi]	10.68	$\eta_{isentropic}$	0.89	$(P_{total})_{inlet}$ [psi]	16.67	$\eta_{isentropic}$	0.90
$(T_{total})_{inlet}$ [R]	717.90	D_{tip} [in]	60.41	$(T_{total})_{inlet}$ [R]	827.97	D_{tip} [in]	34.65
$(P_{total})_{outlet}$ [psi]	16.84	$H_{(blade)1st}$ [in]	19.87	$(P_{total})_{outlet}$ [psi]	165.97	$H_{(blade)1st}$ [in]	7.79
$(T_{total})_{outlet}$ [R]	827.97	$H_{(blade)min}$ [in]	19.87	$(T_{total})_{outlet}$ [R]	1619.64	$H_{(blade)min}$ [in]	2.11
\dot{m} [lb/s]	494.33	N_{stage}	1	\dot{m} [lb/s]	165.21	N_{stage}	5
rpm	7500	$D_{(hub)min}$ [in]	20.68	rpm	11500	$D_{(hub)min}$ [in]	19.07
$\eta_{polytropic}$	0.9	$D_{(hub)max}$ [in]	20.68	$\eta_{polytropic}$	0.92	$D_{(hub)max}$ [in]	28.46

After the design space is created, the design with the highest performance value is chosen. The main design parameters, such as the De-Haller number and diffusion coefficient, are met in this choice. Following the specification of upper and lower limits for these parameters, the preliminary design of the rotor and stator created by using the values are shown in Figure 19.

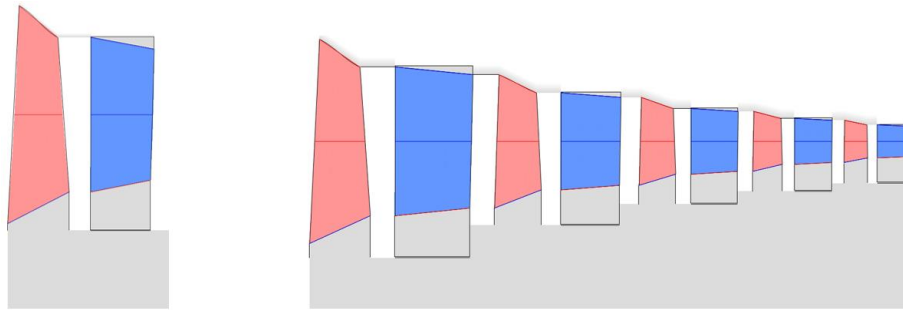


Figure 19. Preliminary Design of Low-Pressure Compressor Rotor and Stator (left), Preliminary Design of High-Pressure Compressor Rotor and Stator (right)

After the preliminary design of the low-pressure and high-pressure compressors are completed, each stage's velocity triangles are obtained, but only the velocity triangles for the mean section of the blades are given in Appendix since there is a time page limitation. Furthermore, 1-D/2-D streamline calculations are performed to determine the total temperature, total pressure, and Mach number distribution in each stage. The flow path through the fan stages is calculated using a streamline analysis, and critical points are identified by looking for pressure and temperature changes in each stage. The distribution of temperature, total pressure, and relative Mach number in the first blade's tip section for low-pressure compressor and the distribution of temperature, total pressure for the high-pressure compressor is given in Figure 20 and Figure 21, respectively.

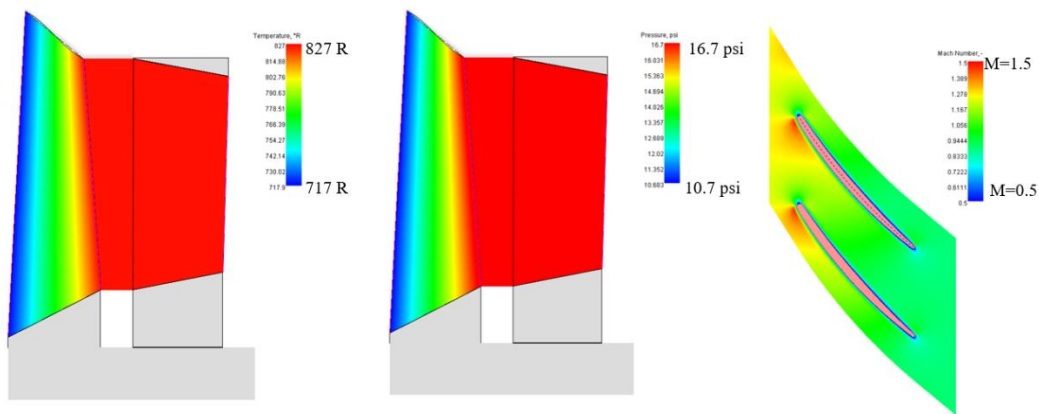


Figure 20. Temperature Distribution of Fan (left), Total Pressure Distribution of Fan (middle), and Relative Mach Number at Tip Section of Fan's Rotor (right)

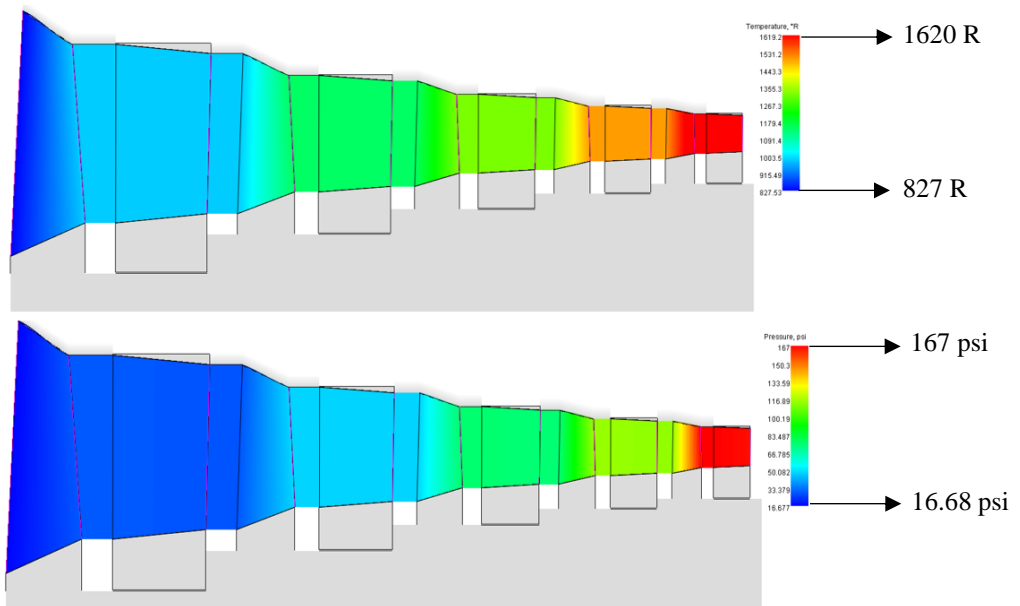


Figure 21. Temperature Distribution of HPC (top), Total Pressure Distribution of HPC (bottom)

When the results are reviewed, it is noticeable that they are consistent with the boundary conditions and design constraints obtained from the survey. Following the blade design, the 3-D rotor and stator geometries for low-pressure and high-pressure compressors are formed, as shown in Figure 22.

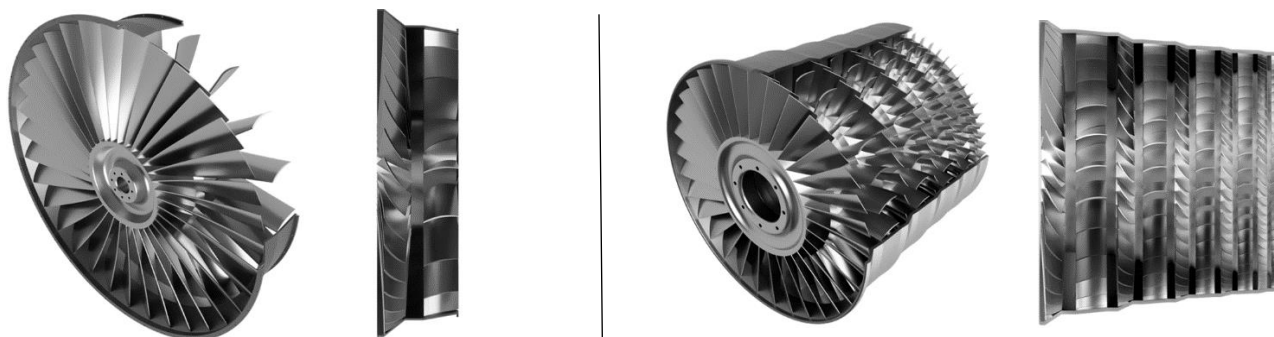


Figure 22. 3-D CAD Geometries of the Fan (left) and the High-Pressure Compressor (right)

Detailed design parameters obtained from AxSTREAM for each stage of the axial fan and high-pressure compressor are given in Table 18 and Table 19, respectively. It is consistent when the results of each parameter are compared with the typical values.

Table 18. Detailed Design Parameters of High-Pressure Compressor

	STAGE 1		STAGE 2		STAGE 3		STAGE 4		STAGE 5	
	Rotor	Stator								
De Haller Number	0.737	0.847	0.736	0.858	0.738	0.865	0.74	0.87	0.744	0.857
Flow Coefficient	0.547		0.58		0.621		0.633		0.652	
Aspect Ratio	2.46	1.88	2.03	1.58	1.71	1.36	1.47	1.19	1.32	1.1
Solidity	1.65	1.28	1.45	1.21	1.31	1.16	1.21	1.08	1.15	1.08
Work Coefficient	0.408		0.401		0.412		0.426		0.443	
Number of Blades	32	27	37	33	44	40	52	48	63	59
Stagger Angle [tan.deg]	43.32	19.29	45.04	19.94	44.99	15.50	44.04	14.53	42.66	13.84
Inlet Metal Angle [tan.deg]	40.48	45.71	36.68	49.63	35.11	51.95	34.72	53.47	34.97	54.54
Outlet Metal Angle [tan.deg]	52.88	95.72	53.23	96.51	54.92	97.06	57.19	97.47	59.72	97.79
Degree of Reaction	0.71	0.29	0.65	0.35	0.71	0.29	0.71	0.29	0.7	0.3
Blade Chord [in]	3.51	3.34	2.78	2.56	2.17	2.04	1.73	1.63	1.36	1.28
Leading Edge Radius [in]	0.07	0.067	0.055	0.052	0.043	0.040	0.034	0.032	0.027	0.026
Trailing Edge Radius [in]	0.035	0.033	0.027	0.026	0.022	0.020	0.017	0.016	0.014	0.013
Hub to Tip Ratio at Inlet	0.47	0.58	0.62	0.71	0.73	0.79	0.81	0.85	0.86	0.89
Hub to Tip Ratio at Outlet	0.58	0.62	0.71	0.73	0.79	0.81	0.85	0.86	0.89	0.9
Mean Radius [in]	13.86									
Stage Pressure Ratio	1.728		1.646		1.574		1.51		1.464	
Polytropic Efficiency [$\eta_{polytropic}$]	0.905		0.922		0.928		0.926		0.92	

Table 19. Detailed Design Parameters of Low-Pressure Compressor

	STAGE 1	
	Rotor	Stator
De Haller Number	0.82	0.79
Flow Coefficient	0.69	
Aspect Ratio	2.41	3.03
Solidity	1.61	1.22
Work Coefficient	0.5	
Number of Blades	34	26
Stagger Angle [tan.deg]	30.89	20.78
Inlet Metal Angle [tan.deg]	54.79	42.98
Outlet Metal Angle [tan.deg]	63.44	95.44
Degree of Reaction	0.7	0.3
Blade Chord [in]	7.56	6.74
Leading Edge Radius [in]	0.15	0.14
Trailing Edge Radius [in]	0.08	0.07
Hub to Tip Ratio at Inlet	0.3	0.43
Hub to Tip Ratio at Outlet	0.44	0.49
Mean Radius [in]	20.45	
Stage Pressure Ratio	1.58	
Polytropic Efficiency [$\eta_{polytropic}$]	0.925	

5.3. Design Guidelines for Turbines

The value ranges of certain turbine design parameters based on literature studies are given in Table 20.

Table 20. Certain Design Parameters for Turbines [14,23,24,25]

Parameter	Typical Values	Parameter	Typical Values
AN^2	$0.5 - 10 \times 10^{10} \text{ in}^2 \cdot \text{rpm}^2$	Zweifel Coefficient, Z_w	0.7-0.8, for Stators / 0.8 – 1.0, for Rotors
Loading Factor (ψ)	1.4 – 2.4	Degree of Reaction at Hub, ${}^\circ R_{\text{hub}}$	$0.15 < {}^\circ R_{\text{hub}}$
Exit Mach Number	0.4 – 0.5	Axial Velocity at Hub, U_{hub}	$U_{\text{hub}} < 1480\text{-}1650 \text{ ft/s}$
Exit Swirl Angle	$0^\circ - 40^\circ$	Hub to Tip Ratio at Inlet	0.5 - 0.85
Degree of Reaction at 50% Span, ${}^\circ R$	$0.3 \leq {}^\circ R \leq 0.6$	Aspect Ratio	2.5 - 3.5
Mach Number between Stages, M_2	0.85-1.2		

The same design approach for compressors is followed for turbine design. For detailed design, the point that meets the design requirements which are consistent with the values that are obtained from the literature survey and has the maximum efficiency for the turbine, is chosen.

5.4. Detailed High-Pressure and Low-Pressure Turbine Design

The PHOENIX Engine has a two-stage high-pressure turbine and a single-stage axial low-pressure turbine (fan). The thermodynamic properties and geometrical dimensions of the low-pressure compressor obtained with the GasTurb 13 are mentioned in Table 21 as boundary conditions.

Table 21. Thermodynamic and Geometrical Properties of High-Pressure and Low-Pressure Turbines

High-Pressure Turbine				Low-Pressure Turbine			
Thermodynamic and Geometrical Properties				Thermodynamic and Geometrical Properties			
$(P_{\text{total}})_{\text{inlet}}$ [psi]	159.33	$\eta_{\text{isentropic}}$	0.92	$(P_{\text{total}})_{\text{inlet}}$ [psi]	166.29	$\eta_{\text{isentropic}}$	0.92
$(T_{\text{total}})_{\text{inlet}}$ [R]	2700.59	D_{tip} [in]	40.88	$(T_{\text{total}})_{\text{inlet}}$ [R]	1988.38	D_{tip} [in]	43.01
$(P_{\text{total}})_{\text{outlet}}$ [psi]	38.75	$H_{\text{(blade)1st}}$ [in]	2.79	$(P_{\text{total}})_{\text{outlet}}$ [psi]	17.0	$H_{\text{(blade)1st}}$ [in]	5.6
$(T_{\text{total}})_{\text{outlet}}$ [R]	1992.34	$H_{\text{(blade)min}}$ [in]	2.79	$(T_{\text{total}})_{\text{outlet}}$ [R]	1657.15	$H_{\text{(blade)min}}$ [in]	5.6
\dot{m} [lb/s]	163.64	N_{stage}	2	\dot{m} [lb/s]	166.587	N_{stage}	1
rpm	11500	$D_{\text{(hub)min}}$ [in]	34.31	rpm	7500	$D_{\text{(hub)min}}$ [in]	26.46
$\eta_{\text{polytropic}}$	0.91	$D_{\text{(hub)max}}$ [in]	35.288	$\eta_{\text{polytropic}}$	0.91	$D_{\text{(hub)max}}$ [in]	31.68

In Figure 23, the rotor and stator geometries of each stage for the High-Pressure and Low-Pressure Turbine in the preliminary design developed using the values in Table 21.

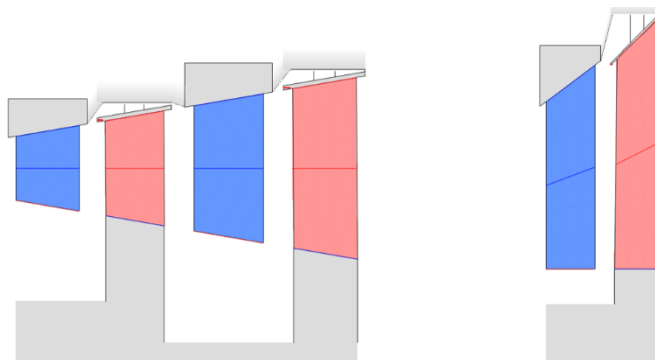


Figure 23. Preliminary Design of HPT Rotor and Stator (left), Preliminary Design of LPT Rotor and Stator (right)

The velocity triangles for each stage are obtained after the preliminary design of the low-pressure and high-pressure turbines are completed, but only the velocity triangles for the mean section of the blades are given in Appendix. Additionally, 1-D/2-D streamline calculations are used to calculate the total temperature and total pressure distributions in each stage, as shown in Figures 24 and 25, respectively. Further, 3-D geometries of the turbines are given in Figure 26.

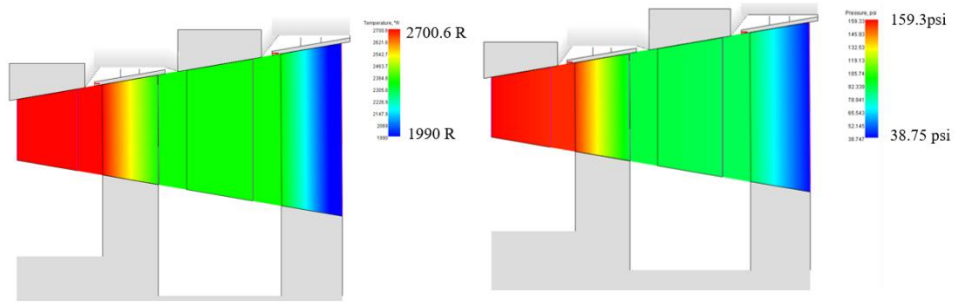


Figure 24. Temperature Distribution of High-Pressure Turbine (left), Total Pressure Distribution of High-Pressure Turbine (right)

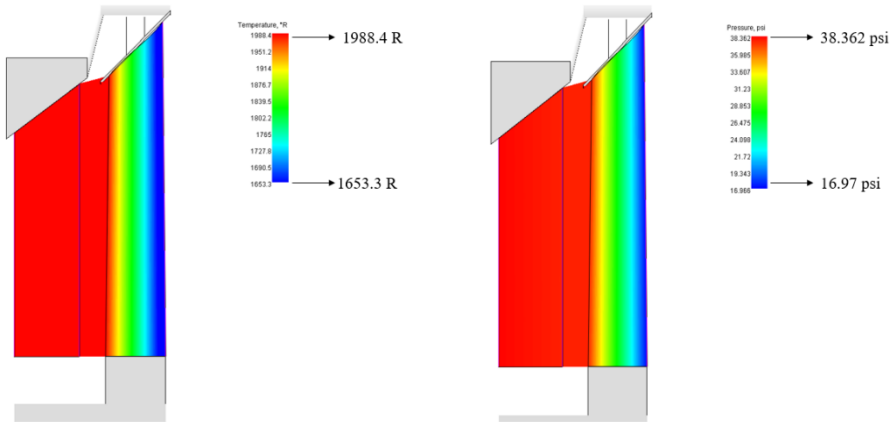


Figure 25. Temperature Distribution of Low-Pressure Turbine (left), Total Pressure Distribution of Low-Pressure Turbine (right)

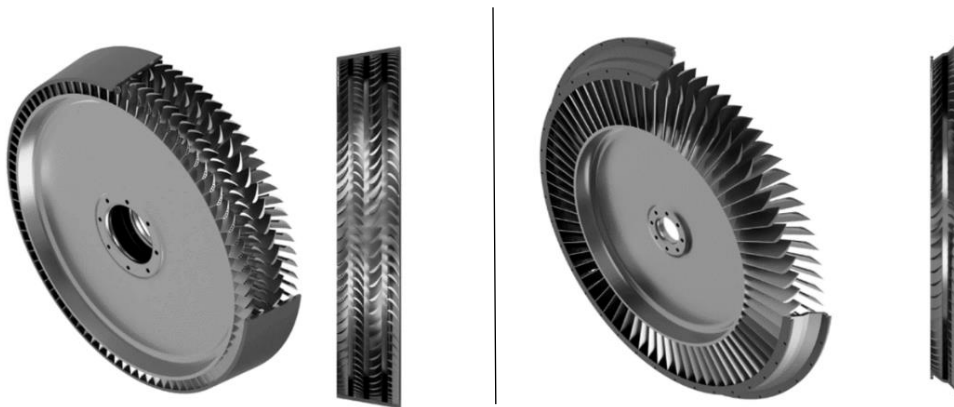


Figure 26. 3-D CAD Geometry of the High-Pressure Turbine (left) and the Low-Pressure Turbine (right)

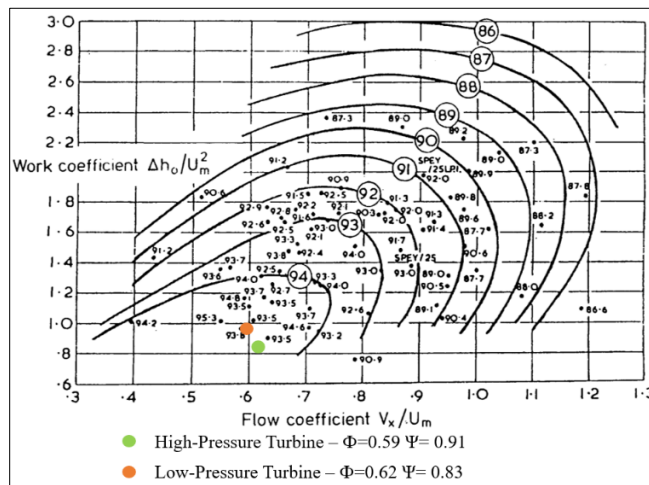


Figure 27. Smith Chart for Turbine Efficiency

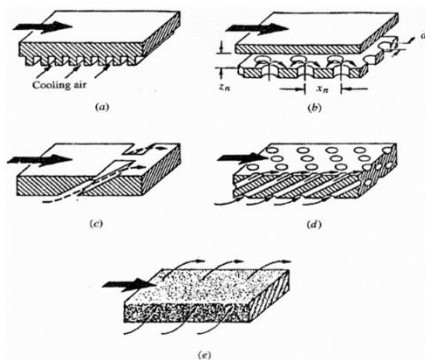
In Table 22, specific design parameters for high-pressure and low-pressure turbines which are consistent with the literature values are listed. Further, the Smith Chart which is used to indicate the average efficiency of the turbines, is given in Figure 27.

Table 22. Detailed Design Parameters of High-Pressure and Low-Pressure Turbines

	High-Pressure Turbine				Low-Pressure Turbine	
	STAGE 1		STAGE 2		STAGE 1	
	Stator	Rotor	Stator	Rotor	Stator	Rotor
Aspect Ratio	1.31	1.45	1.48	2.0	3.09	4.21
Number of Blades	82	88	72	86	69	81
Solidity	1.32	1.43	1.33	1.44	1.36	1.39
Work Coefficient, Ψ	0.81		1.06		0.9	
Degree of Reaction	0.31	0.69	0.51	0.49	0.5	0.5
Degree of Reaction at Hub	0.26	0.31	0.51	0.51	0.41	0.42
Inlet Metal Angle [tan.deg]	90	86.69	91.79	89.93	90	98.64
Outlet Metal Angle [tan.deg]	28.39	29.62	26.41	27.09	32.49	29.84
Stagger Angle [tan.deg]	44.61	42.40	46.63	45.38	42.36	40.71
Zweifel Coefficient	0.88	0.83	0.70	0.78	0.92	0.76
Hub to Tip Ratio at Inlet	0.9	0.83	0.86	0.82	0.84	0.72
Hub to Tip Ratio at Outlet	0.91	0.88	0.84	0.81	0.7	0.68
Flow Coefficient, Φ	0.47		0.60		0.64	
Blade Chord [in]	1.67	1.49	1.9	1.71	2.08	1.88
Mean Radius [in]	16.52				16.615	
AN^2 [$\text{in}^2 \cdot \text{rpm}^2 \times 10^{10}$]	2.22	2.97	3.86	4.69	3.92	5.01
Stage Pressure Ratio	1.73		2.37		2.26	
Exit Mach Number	0.48				0.5	

5.5. Nozzle Guide Vane Cooling

Although the ability to operate at high temperatures has a critical role in improving the performance of jet engines, an adequate amount of cooling is needed to sustain high turbine inlet temperatures for a long time. As a result, nozzle guide vane cooling is an important design issue [26]. First-stage stator blades are exposed to high temperatures from the combustor, whereas first-stage rotor blades are colder due to the dilution of hot gases with first-stage stator cooling air. On new aircraft engines, approximately 20% of the compressor discharge flow is used for cooling [27]. Turbine blade cooling methodologies and ranges of turbine-inlet temperatures for relevant cooling systems are illustrated in Figure 28.



Temperature Range (R)	Cooling Methods
$T < 2160$	Cooling is not required
$2160 < T < 2610$	Internal convective cooling
$2610 < T < 2880$	Convective systems augmented by rows of film cooling holes
$2880 < T < 3600$	Combination of convection, impingement systems and film cooling
$T > 3600$	Transpiration Cooling

Figure 28. a) Convection Cooling, b) Impingement Cooling, c) Film Cooling, d) Full-Coverage Film Cooling, e) Transpiration Cooling [21] (left), Cooling Systems for Ranges of Turbine Entry Temperatures [14] (right)

Considering the analyses and the information given above, convection and film cooling methodologies are selected for PHOENIX. The designed nozzle guide vane for PHOENIX is given in Figure 29.

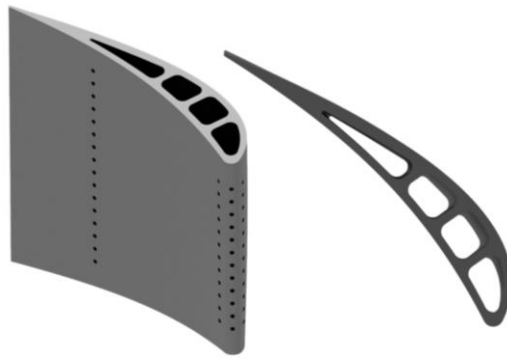


Figure 29. Cooled Nozzle Guide Vane of the PHOENIX

6. COMBUSTION CHAMBER DESIGN

This section contains detailed information about the combustion chamber of the PHOENIX Engine. The combustion chamber is the part of a jet engine that burns the fuel and air mixture. To achieve a high combustion efficiency, proper air and fuel mixing are essential. Fitting a swirler in the dome around the fuel injector is one of the most efficient ways of inducing flow recirculation in the primary zone [28]. With the aid of swirlers, liquid fuel should be atomized into tiny droplets as quickly as possible for high combustion efficiency. In addition, many criteria must be considered when designing a highly efficient combustion chamber, and the combustor must meet a broad range of requirements [28].

Combustion chambers are classified into three different types, which could be expressed as the can combustor (tubular), annular combustor, and can-annular (tubo-annular) combustor. Due to its clean aerodynamic structure, fully annular combustion is the most widely used type of combustor. As compared to other types of the combustor, the annular combustor has many advantages which could be given as more uniform combustion, less surface area, and shorter size compared to other types of the combustor, tending to have uniform exit temperatures, having the lowest pressure difference (approximately 5% of combustor inlet total pressure), and simplified design are among these advantages [28]. The three types of the combustor are given in Figure 30.

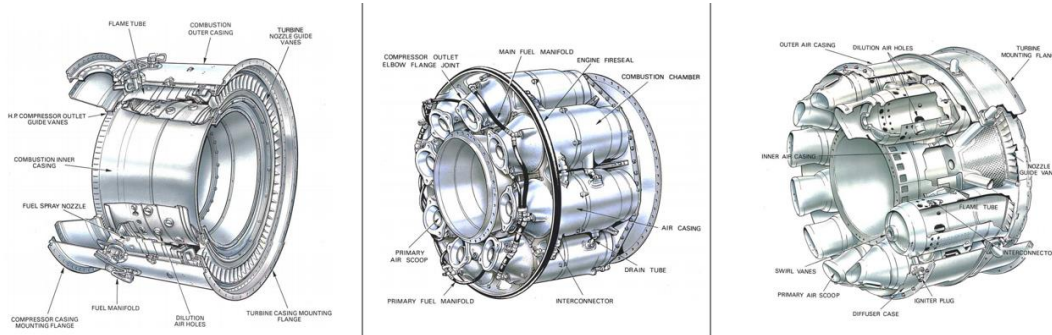


Figure 30. The Types of the Combustor (Annular Combustor (left), Can Combustor (middle), Turbo-annular Combustor (right)) [29]

As a result, the annular combustor was chosen and designed for ETU-PHOENIX. The critical components of annular combustion and the geometry of the combustion chamber are depicted in Figure 31.

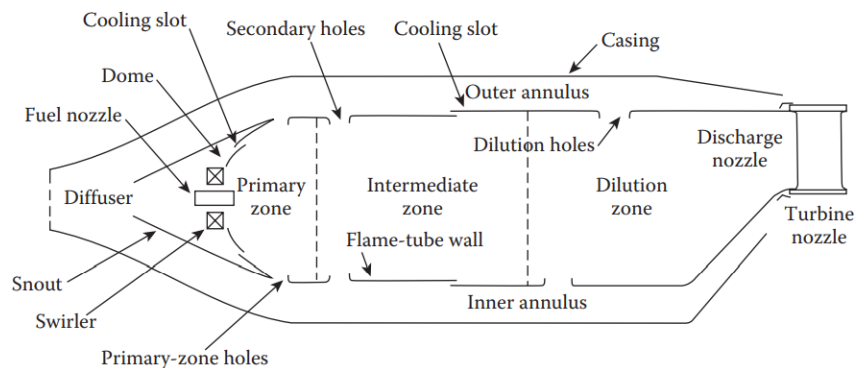


Figure 31. Geometric Representation and Main Components of an Annular Combustor [28]

6.1. Selection of the Pre-Diffuser Configuration

Compressor outlet velocities could exceed 558 ft/s or higher in many aircraft engines. Before the combustion process can begin, the air velocity must be reduced significantly, typically to one-fifth of the compressor outlet velocity [28].

In Figure 32, the annular dump diffuser principle is illustrated. Even though the dump configuration has a pressure loss because of the sudden expansion at the pre-diffuser outlet, the length and weight savings more than compensate for this penalty. Due to these characteristics, a dump diffuser is particularly beneficial in aircraft applications. In addition, the dump diffuser provides a reliable flow pattern that is unaffected by manufacturing tolerances, differential thermal expansions between the liner and combustor casing, and changes in inlet velocity profile [28]. Considering the information given above, it is decided to select a dump diffuser configuration for the ETU-PHOENIX Engine.

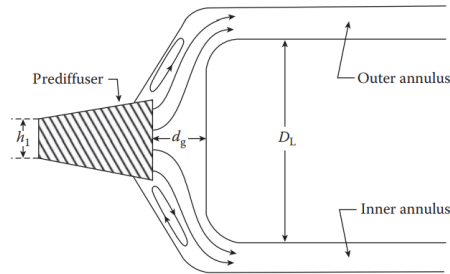


Figure 32. Representation of the Dump Diffuser [28]

6.2. Fuel Atomizing Flow

The processes of liquid atomization and evaporation are critical to the efficiency of a gas turbine combustion system. As a result, liquid fuel can be atomized into many droplets with a smaller droplet size inducing quick evaporation. For this purpose, there are numerous atomizer design trends. For PHOENIX Engine, a pre-filming radial-axial air-blast swirler type atomizer was chosen since it enables central recirculation vortex structures and liner walls are relatively cold, reducing exhaust smoke [30,31]. The air-blast atomizer, which is used for PHOENIX Engine, is given in Figure 33.

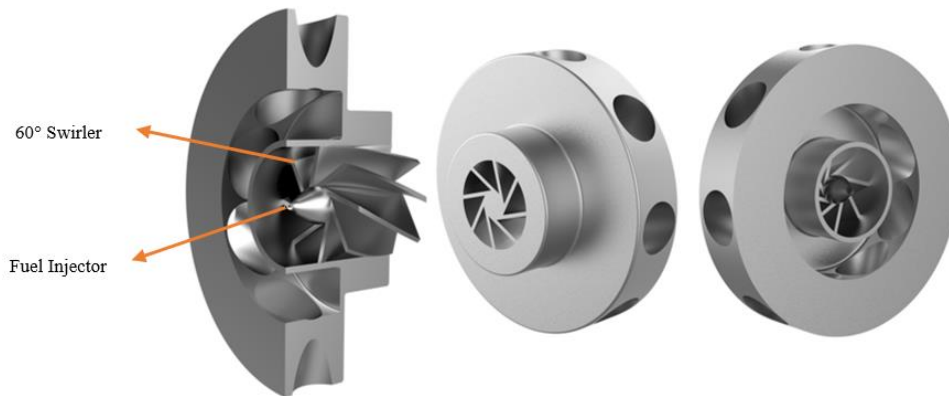


Figure 33. Air-blast Atomizer of ETU-PHOENIX

6.3. Selection of the Rich-Burn Quick-Quench Lean-Burn (RQL) Configuration

NOx emissions are another critical factor to consider when designing a combustion chamber. A low-emission design includes a balance that allows for enough time and temperatures to complete the reactions. Three separate concept modeling approaches are highlighted for this reason. Lean-Premixed-Pre-vaporized Combustor (LPP), Rich-Burn Quick-Quench Lean-Burn (RQL), and Direct Injection are the three types of combustion systems (DI) [32].

RQL concept is chosen for PHOENIX Engine due to the rich region, where NOx formation rates are poor due to combined effects of oxygen depletion and low temperature inducing good stability, fast mixing with the rest of the combustion air in the quick quench zone [30,32]. In order to reduce the volume rates of smoke, carbon monoxide (CO), and unburned hydrocarbons (UHC), the primary zone equivalence ratio should not be greater than 1.6. The definition of the equivalence ratio is given in terms of FAR (Fuel Air Ratio) as shown in Eqn. (6.3.1).

$$\Phi = \frac{m_{\text{fuel}}/m_{\text{air}}}{(m_{\text{fuel}}/m_{\text{air}})_{st}} = (FAR)/(FAR)_{st} \quad (6.3.1)$$

6.4. Advanced Cooling Techniques

Cooling is used in most modern gas turbines. About 40 percent of the air leaving the compressor is used for cooling. Liners are used to keep the combustion process contained and to ensure that enough air is distributed to all of the various combustion zones. The liner must be thermally resistant enough to endure continuous and cyclic high-temperature operation, as well as structurally strong enough to withstand the buckling load produced by differential strain. This could be achieved by the efficient use of cooling air and the application of suitable materials [30]. Film cooling is the most common method of protecting the combustion chamber. The method's key benefit is that the cooling slots could be built to withstand extreme pressure and thermal stresses at high temperatures for thousands of hours. Furthermore, the stiffness offered by the cooling slots results in a lightweight and mechanically robust liner construction [28]. The film cooling method is depicted in Figure 34.

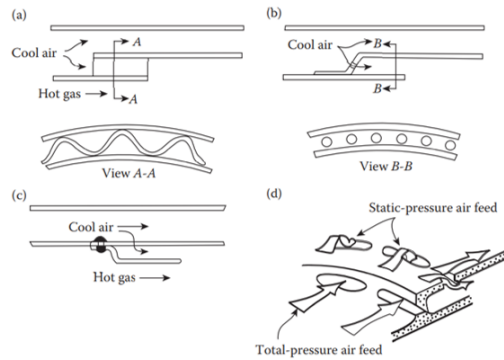


Figure 34. Film Cooling Methodologies ((a) Wigglestrip, (b) Stacked Ring, (c) Splash-Cooling Ring, (d) Machined Ring) [28]

For the PHOENIX Engine, stacked ring film cooling is chosen. The cooling-air velocity could be maintained at the optimum value for optimal cooling effectiveness, regardless of the actual pressure drop through the liner, which is a benefit of this technique [28]

6.5. Geometry and Performance of the Combustion Chamber

A recently developed MATLAB code was used to calculate the combustor's geometrical dimensions and important combustion performance parameters. While determining the critical dimensions of the combustion chamber, some assumptions were made. Table 23 shows the typical values of the combustion chamber design parameters and the assumptions selected for the ETU-PHOENIX Engine.

Table 23. Typical Design Parameters of the Combustion Chamber [30,31,33,34]

Design Parameters	Typical Values	Assumptions	Design Parameters	Typical Values	Assumptions
Reference Velocity (ft/s)	16 - 131	120.39	Stoichiometric FAR (Fuel to Air Ratio)	0.0685	0.0685
Dome Velocity (ft/s)	22 - 40	29.36	Equivalence Ratio in the Primary Zone (Φ_{pz})	1.2 - 1.6	1.5
Passage Mach Number	0.1 - 0.15	0.12	Equivalence Ratio in the Secondary Zone (Φ_{sz})	0.4 - 0.8	0.7
Pattern Factor (PF)	0.2 - 0.3	0.3	The Ratio of Primary Zone Length to Flame Tube Height	1 - 1.1	1
Mean Flame Tube Temperature (R)	3600 - 4500 R	3960 R	The Ratio of Secondary Zone Length to Flame Tube Height	1.2 - 1.3	1.2
Snout Discharge Coefficient	1	1	Total Pressure Loss in Diffuser (ΔP)	1%	1%

In Table 24, the design conditions for the combustion chamber as determined by GasTurb 13 are given.

Table 24. On-Design Conditions of the Combustion Chamber

Parameter	Value	Parameter	Value
Total Air Mass Flow Rate (lb/s)	153.9	Static Temperature at Combustor Inlet (R)	1602.02
Total Fuel Mass Flow Rate (lb/s)	2.86	Total Temperature at Combustor Outlet (R)	2744.74
Mach Number at Combustor Inlet	0.25	Static Temperature at Combustor Outlet (R)	2708.63
Mach Number at Combustor Outlet	0.3	Total Pressure at Combustor Inlet (psi)	165.97
Total Temperature at Combustor Inlet (R)	1619.64	Total Pressure at Combustor Outlet (psi)	159.33

Geometric results of the combustion chamber as a result of the calculations made for on-design condition using the MATLAB code are given in Table 25.

Table 25. Geometrical Results of the Combustion Chamber

Geometrical Parameters	Value	Geometrical Parameters	Value
Combustion Chamber Angle (degree)	8.60	Reference Height (in)	5.024
Diffuser Inlet Area (in ²)	172.52	Snout Inner Area (in ²)	27.59
Diffuser Inlet Height (in)	1.626	Snout Inner Height (in)	0.26
Diffuser Angle (degree)	48.85	Snout Outer Area (in ²)	138.11
Diffuser Area Ratio	0.80	Snout Outer Height (in)	1.95
Diffuser Length (in)	0.142	Total Length of Combustor (in)	18
Dome Area (in ²)	556.14	Liner Length (in)	14.01
Dome Height (in)	4.189	Liner Inner Radius (in)	14.80
Dome Length (in)	0.599	Liner Outer Radius (in)	19.0
Dome Diffuser Angle (degree)	52.81	Recirculation Zone Length (in)	3.354
Flame Tube Volume (in ³)	6022.1	Recirculation Zone Angle (degree)	64.54
Primary Zone Length (in)	3.69	Reference Area (in ²)	666.7
Secondary Zone Length (in)	6.89	Passage Area (in ²)	110.52
Dilution Zone Length (in)	3.43	Passage Height (in)	0.665
Combustion Inner Radius (in)	14.39	Combustion Outer Radius (in)	19.41
Primary Hole Diameter (in)	0.67	Primary Hole Number per Nozzle	4
Secondary Hole Diameter (in)	0.63	Secondary Hole Number per Nozzle	4
Dilution Hole Diameter (in)	0.47	Dilution Hole Number per Nozzle	8
Swirler Diameter (in)	2.28	Number of Fuel Nozzle	24

In addition, the parameters related to a flame tube hole, which could be defined as crucial parameters, are shown in Table 26.

Table 26. Flame Tube Hole Parameters

Parameters	Value
Jet Velocity (ft/s)	~330
Primary Hole Discharge Coefficient	0.55
Secondary Hole Discharge Coefficient	0.5
Dilution Hole Discharge Coefficient	0.63

In order to determine whether the combustion chamber design obtained is effective, several constraints were also considered. The combustion chamber performance constraints are given in Table 27.

Table 27. Performance Constraints of the Combustion Chamber [30,31,33,34]

Design Parameters	Typical Values
Loading Factor (kg/bar ^{1.8} m ³ s)	$\Omega < 1$
Combustion Intensity (MWx10 ⁴ /m ³ atm)	$I_{comb} > 50$
Residence Time (ms)	$\tau_{res} > 3$
Air Liquid Ratio (ALR)	$ALR > 7$

The combustion chamber performance parameters can be seen in Table 28. When the results are reviewed, the values obtained from MATLAB results are compatible with the values in the literature.

Table 28. Combustion Chamber Performance Parameters

Parameters	Value
Residence Time (ms)	4.10
Loading Factor (kg/bar ^{1.8} m ³ s)	0.51
Combustion Intensity (MWx10 ⁴ /m ³ atm)	54.57
Air-Liquid Ratio	7.59
Air-Fuel Ratio	53.88
Global Equivalence Ratio	0.271

The designed combustion chamber geometry as a result of the MATLAB outputs is given in Figure 35.

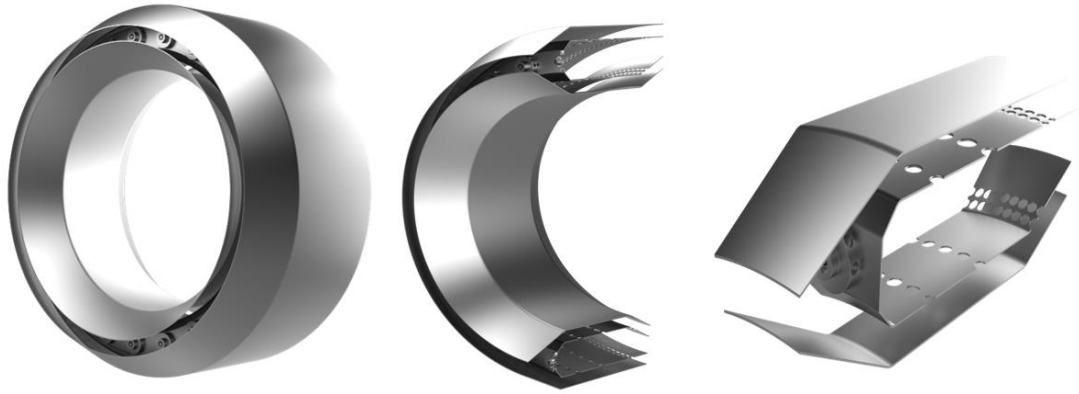
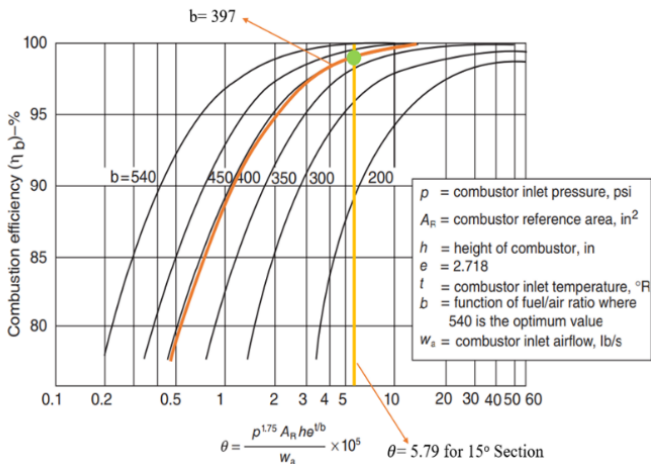


Figure 35. 3-D CAD Model of the Combustion Chamber of ETU-PHOENIX (left), 180° Section of the Combustion Chamber of ETU-PHOENIX (middle), 15° Section of Annular Combustion Chamber of ETU-PHOENIX (right)

6.6. Computational Fluid Dynamics Analysis and Combustion Chamber Efficiency

Combustion efficiency compares the real rate of heat release in a burner to the maximum theoretical rate of heat release [14]. The combustion loading parameter (θ), which correlates well with the combustion efficiency, is introduced by Lefebvre for a gas turbine combustion chamber which is given in Equation 6.6.1. In Equation 6.6.1, 'b' is defined as the reaction parameter which depends on the primary zone equivalence ratio (ϕ_{pz}). In addition, the relationship between combustion efficiency and combustion loading parameter is given in Figure 36 which also indicates the combustion efficiency of the combustor of PHOENIX.

$$\theta = \frac{p^{1.75} A_R h e^{\frac{T}{b}}}{w_a}, \quad b = 382 \left(\sqrt{2} \pm \ln \left(\frac{\phi_{pz}}{1.03} \right) \right) \quad [(+) \text{ for } \phi_{pz} < 1.03, (-) \text{ for } \phi_{pz} > 1.03] \quad (6.6.1)$$



Design Parameter	Supersonic Cruise Condition
Primary Zone Equivalence Ratio (ϕ)	1.5
Combustion Loading Parameter (θ)	5.792×10^5
Reaction Rate Parameter (b)	397
Combustion Efficiency (η_{comb})	~99% (15° section of the combustor)

Figure 36. Combustion Efficiency vs. Combustion Loading Parameter [14] (left), Design Parameters and Values for Supersonic Condition (right)

3-D computational fluid dynamics analysis is performed using outputs using Siemens STAR CCM+. These calculations were examined in the sector of 15° considering 24 fuel injectors. The polyhedral mesh was created for the geometry shown above. Detailed information about the mesh is given in the following Table 29. The generated mesh scene taken from a middle plane of the geometry and the boundary conditions used in computational fluid dynamics analysis is given in Figure 37. In addition, the meshes in the primary, secondary jets, cooling (dilution) holes, and swirler are tightened.

Table 29. Information Related with Generated Mesh

Mesh Type	Number of Cells	Number of Prism Layers	Base Size (mm)
Polyhedral Mesh	1825485	7	7.5

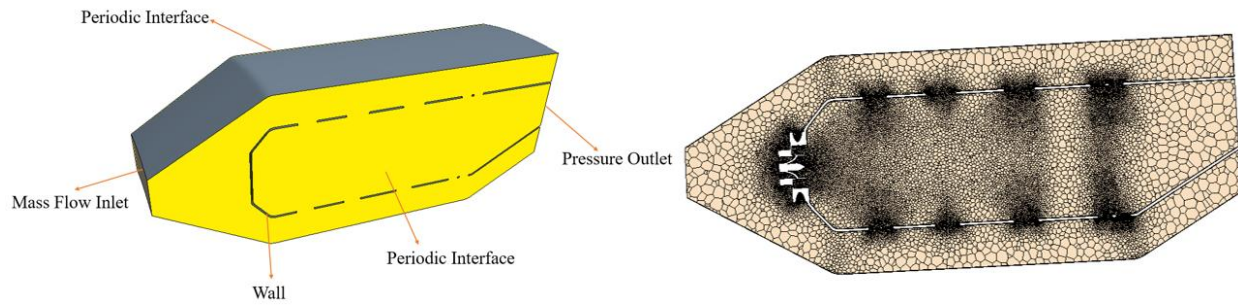


Figure 37. Boundary Conditions of the Geometry (left), Generated Mesh for the Geometry (right)

In this analysis, the Realizable $k-\epsilon$ Turbulence Model and the Standard Eddy Break Up (SEBU) combustion model is used. Shih et al. [Turbulent Flow/Pope] developed the realizable $k-\epsilon$ turbulence model for flow problems for which the Standard $k-\epsilon$ model is insufficient. The standard Eddy Break Up (SEBU) is a combustion model, a fast chemistry approach proposed by Spalding in 1970 [31].

The temperature at mid-plane, the temperature at outlet plane, velocity magnitude at mid-plane, and velocity vector at mid-plane contours are given in Figure 38.

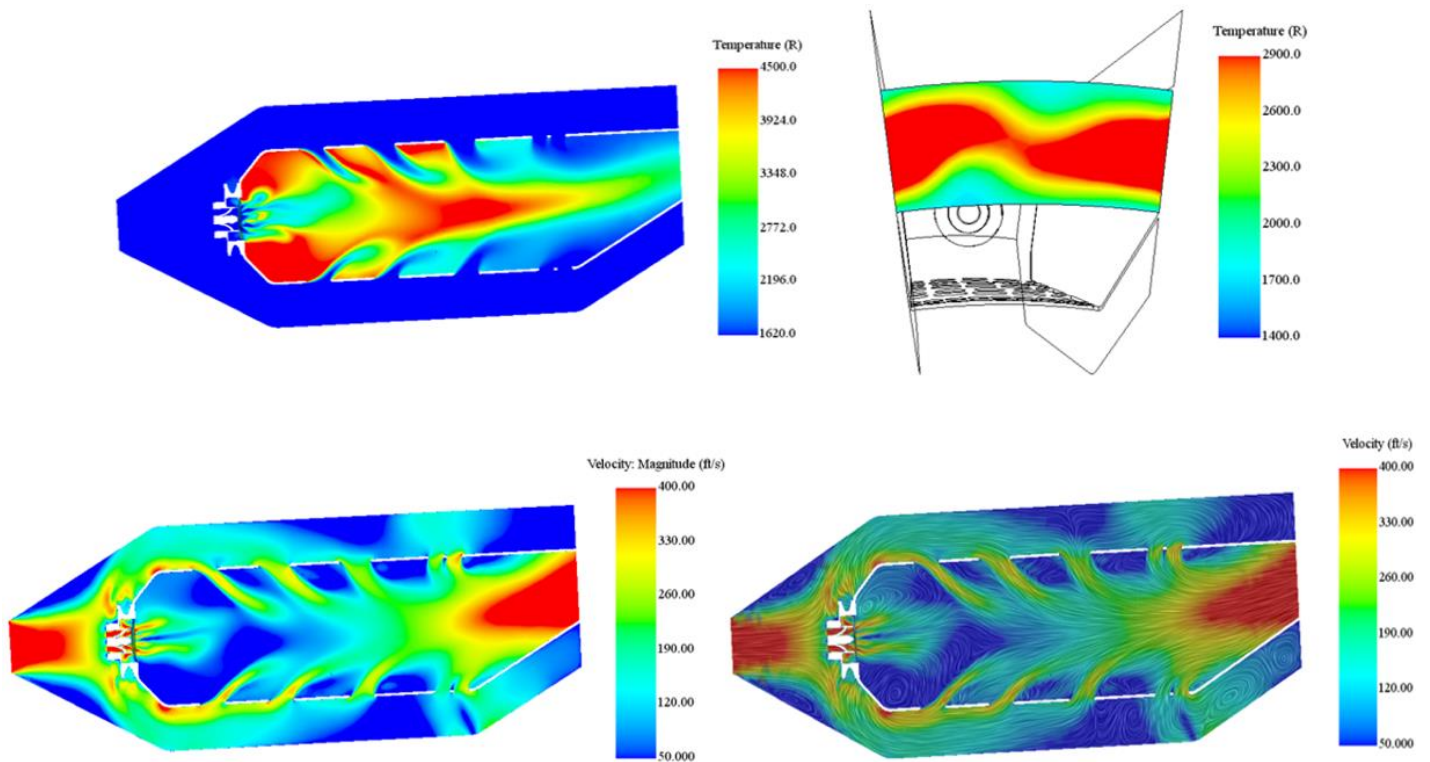


Figure 38. Temperature at Mid-Plane (top-left), Temperature at Outlet Plane (top-right), Velocity Magnitude at Mid-Plane (bottom-left), Velocity Vector at Mid-Plane (bottom-right)

If the results of the analysis are examined, it could be seen that the recirculation zones help the mixing of fuel and air. For effective cooling of liners, the Mach number should be kept lower than 0.15, which was achieved. As could be seen from Exit Temperature contours, the regions that contact with the nozzle guide vane were kept lower, which is necessary for avoiding the nozzle guide vanes from higher temperatures. As a result of the 3-D computational fluid dynamics analysis, the outlet temperature distribution (Mass flow averaged), combustion efficiency, and pressure difference which are essential parameters for the combustion chamber, were calculated and given in Table 30.

Table 30. CFD Results of the Combustion Chamber

Combustion Efficiency (π_{comb})	98.7%
Total Temperature at Outlet (R)	2728.8
Pressure Difference	3.01%

7. MIXER DESIGN

Turbofan jet engines have hot & fast core and cold & slow bypass flow, and in mixed flow turbofan jet engines, these two flows are mixed before the engine outlet, as shown in Figure 39 (Left). However, if these two flows meet as they are, the mixing will be in a chaotic way, and it causes noise and loss of thrust. In addition, this not well mixed low-density hot core flow will cause high velocities at the nozzle outlet. It might be considered positive for thrust, but it significantly increases the noise. However, the relatively quieter flow with higher density and lower velocity are desirable, especially for SST airplanes like Concorde. To provide this, mixers are designed to mix the flows with as little pressure loss as possible by creating a vortex, as shown in Figure 39 (Right). For this reason, a mixer should be used in mixed flow turbofan jet engines like the Phoenix.

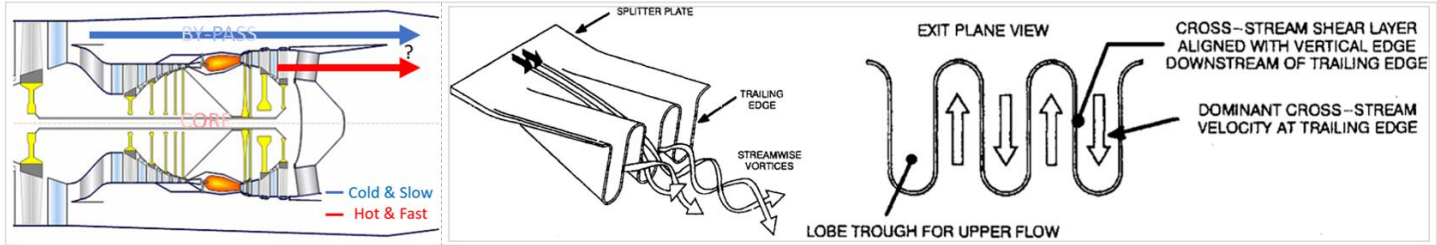


Figure 39. Mixed Flow Turbofan Engine Core and Bypass Flow (Left), Expected Flow Development from The Mixer (Right) [35]

7.1 Mixer Type, Number of Lobes and Shape Selection

State-of-the-art and widely used lobe-forced mixer type is selected because of the mixing performance and low total pressure loss. However, this mixer type can be used in different shapes and numbers of lobes. Firstly, to select the number of lobes of the mixer, various mixers were compared as shown in Figure 40 from Reference [37]. As shown in the figure below, with the increasing number of mixer lobes, an increase in the quality of the mixture has been observed from mixedness index and temperature distribution with the cost of pressure drop, however, because of the significant change in mixture quality, 18 lobes selected as a number of lobes of the mixer.

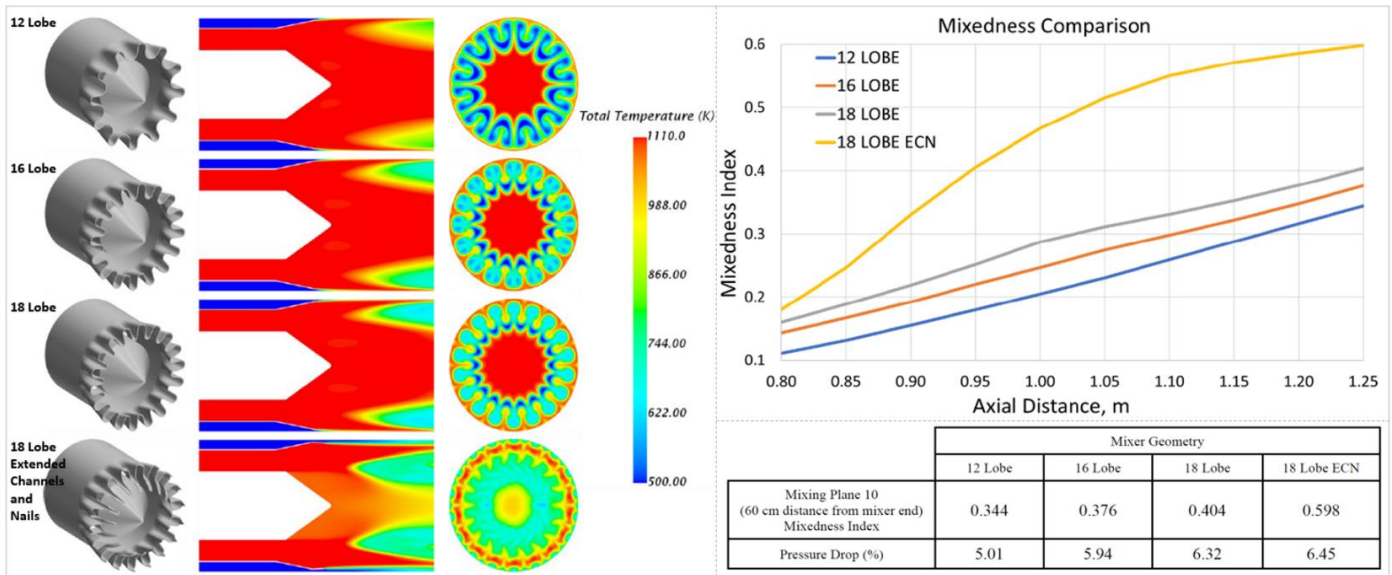


Figure 40. Comparison of Mixers with Different Number of Lobes (Left: Total Temperature Contours, Top-Right: Mixedness Index - Axial Distance Graph, Bottom-Right: Mixedness Index & Pressure Drop Values) [37]

Secondly, to select the mixer shape of the Phoenix, various mixers from Reference [38] and Reference [39] were compared. Pressure drop, σ (Total pressure recovery coefficient), n_{tr} and mixedness index is selection criteria. While mixedness index and n_{tr} are about mixture quality, Pressure drop and σ is about how much energy is lost during the mixing. After the mixer, a length is required for mixing to develop, and the ratio of this length to diameter is around 1.5 for the Phoenix. Under these conditions, as shown in Figure 41, the longer nail NSwALN mixer shape gives the highest mix quality for 1.5 x/d with relatively low-pressure loss. In addition, considering both articles, it has been seen that the longer nail structures significantly increase the mixing performance. However, in high lobe numbers, when all the nails are extended, the nails intersect with each other. For this reason, to have both 18 lobe numbers and long nails, two lobes and one penetrating long nail structure are selected like NSwALN type mixer for Phoenix mixer.

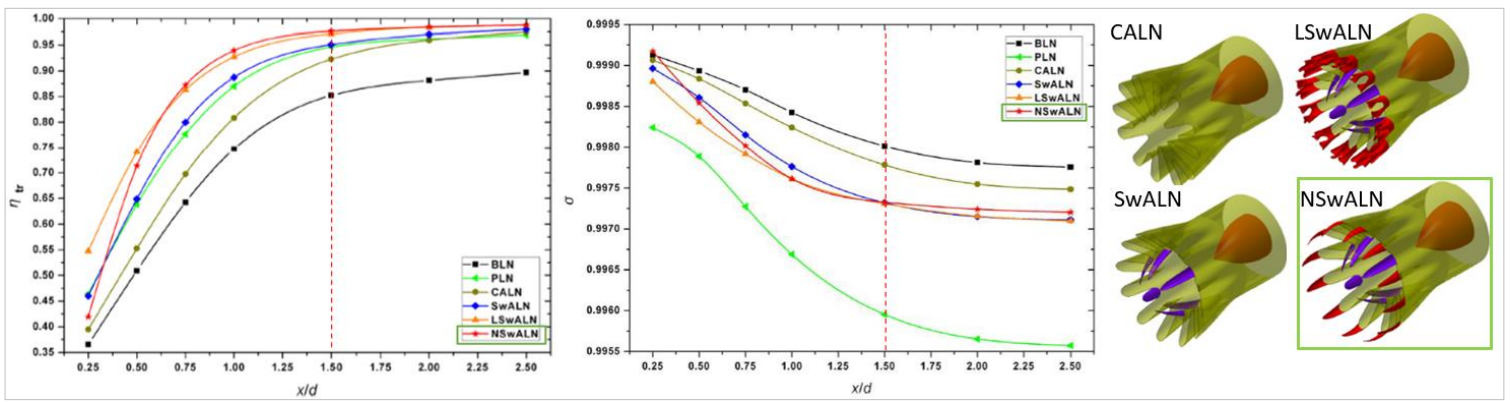


Figure 41. Thermal Mixing Efficiency and Total Pressure Recovery Coefficient Along the Axis of the Different Lobed Mixers and Mixer Geometries [39]

GasTurb 13 was used to determine geometric lengths. For the required lobe angles, the ratios of the NSwALN mixer type are used according to the determined number of lobes. Then, using these geometric quantities, the mixer design of the Phoenix engine was completed in the CAD design, as shown in Figure 42.

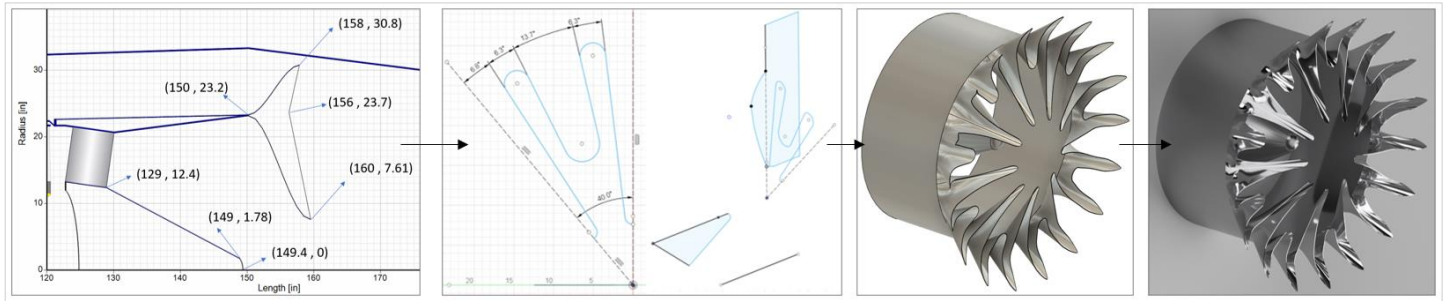


Figure 42. Geometry Inputs and 3-D CAD Design of the ETU-PHOENIX Mixer

8 VARIABLE NOZZLE DESIGN

The nozzle design goals of the PHOENIX engine are to bring the exhaust gases to the required speeds and to keep the pressure loss to a minimum while doing this, to provide the necessary thrust under on-design and off-design conditions, to keep the exhaust gases outlet pressure equal to or slightly higher (under-expanding) atmospheric pressure. It consists of certain basic criteria such as reducing jet noise, having a long cycle life, and being low cost and light while doing all these.

8.1 Nozzle Type Selection

The nozzle type should be decided as the first step of the nozzle design process. Equation 8.1.1 from Farokhi [14] is used in order to decide the appropriate nozzle between two basic nozzle options, which are convergent and divergent.

$$\frac{F_{g\text{-condi}}}{F_{g\text{-conv}}} = \sqrt{\frac{1 - (\text{NPR})^{-\frac{\gamma-1}{\gamma}}}{\frac{\gamma-1}{\gamma+1}}} \times \frac{\gamma}{\gamma + \left(1 - \left(\frac{\gamma+1}{2}\right)^{\frac{\gamma}{\gamma-1}} \times \frac{1}{\text{NPR}}\right)} = 1.126 \quad (8.1.1)$$

NPR, Nozzle Pressure Ratio (P_{07}/P_0) = 11.9416
 γ , Ratio of specific heats = 1.2112

When the result of the equation is examined, using the convergent-divergent nozzle for the on-design condition provides 12.6% more thrust than the use of the convergent nozzle. According to Farokhi [14], it is recommended to use convergent-divergent nozzles in cases of 5.5% and above thrust increases.

8.2 Variable Nozzle Geometry

To create an appropriate nozzle geometry, three steps were followed. Firstly, a literature survey was made to find some relations to select proper dimensions for a nozzle. Then, these relations were applied to the Phoenix engine, and a nozzle geometry was formed. Lastly, CFD analyzes were executed to give the nozzle its final shape and also to check the off-design characteristics of the nozzle.

8.2.1 Literature Survey About Nozzle Geometry Calculations

Before starting to design nozzle geometry, a literature survey was made. Then, some calculations were made according to these studies. From Saeed Farokhi's Aircraft Propulsion [14], the necessary equations were found to create the nozzle geometry and according to the equations, an original MATLAB code was created. Outputs from the GasTurb13 software were expected to match to verify the MATLAB code. Also, the Specific heat ratio of exhaust gases at 8th and 9th stations is used to calculate most of these values. Thus, for that calculations Equation (8.2.1) is solved iteratively in MATLAB.

$$T_{s8} = \frac{T_{08}}{\left(1 + \frac{\gamma_1 - 1}{2} \times M_8\right)}, \quad T_{s9} = \frac{T_{09}}{\left(1 + \frac{\gamma_2 - 1}{2} \times M_9\right)} \quad (8.2.1)$$

After calculating γ_1 and γ_2 , an average of these two values γ is calculated:

$$\gamma = \frac{\gamma_1 + \gamma_2}{2} \quad (8.2.2)$$

Next, Mass Flow Parameter (MFP) is calculated by using Equation (8.2.3) to calculate the throat area required for the choked condition where Mach Number equals "1".

$$MFP = \sqrt{\frac{\gamma}{R}} \times \left(\frac{\gamma + 1}{2}\right)^{\frac{\gamma+1}{2(1-\gamma)}} \quad (8.2.3)$$

Nozzle throat area (A_8) is calculated by using Equation (8.2.4)

$$MFP = \frac{\dot{m}_8 \sqrt{T_{08}}}{A_8 P_{08}} \quad (8.2.4)$$

Nozzle exit area (A_9) is calculated by using the nozzle area ratio (A_9/A_8). However, the existence of a boundary layer on a surface represents a displacement thickness blocking the geometric flow field. There is also a total pressure loss associated with the formation of the boundary layer in the wall. The combined effect of these parameters on the mass flow rate is called the "Discharged Coefficient (C_D)". With this coefficient, the effective nozzle throat area (A_{8e}) can be calculated.

$$C_D = \frac{A_{8e}}{A_8} \quad (8.2.5)$$

With discharged coefficient and non-discharged coefficient, nozzle exit numbers (M_9 and M_{9i}) can be calculated using Equation (8.2.9).

$$\frac{A_9}{A_{8e}} = \frac{1}{M_9} \left(\left(\frac{2}{\gamma + 1} \right) \left(1 + \frac{\gamma - 1}{2} M_9^2 \right) \right)^{\frac{\gamma+1}{2\gamma-2}}, \quad \frac{A_9}{A_8} = \frac{1}{M_{9i}} \left(\left(\frac{2}{\gamma + 1} \right) \left(1 + \frac{\gamma - 1}{2} M_{9i}^2 \right) \right)^{\frac{\gamma+1}{2\gamma-2}} \quad (8.2.6)$$

Using the isentropic equations, the ratio of static pressure and the total pressure at the outlet of the nozzle can be calculated for the values of discharged coefficient and non-discharged coefficient nozzle exit numbers from Equation (8.2.9).

$$\frac{P_9}{P_{09}} = \left(\frac{1}{1 + \frac{\gamma - 1}{2} M_9^2} \right)^{\frac{\gamma}{\gamma - 1}}, \quad \frac{P_{9i}}{P_{09i}} = \left(\frac{1}{1 + \frac{\gamma - 1}{2} M_{9i}^2} \right)^{\frac{\gamma}{\gamma - 1}} \quad (8.2.7)$$

By putting the calculated pressure ratios, the velocity for discharged and non - discharged values at the nozzle exit is obtained by Equation (8.2.8).

$$V_9 = \sqrt{R \times T_{08}} \sqrt{\frac{2\gamma}{\gamma - 1} \left(1 - \left(\frac{P_9}{P_{09}} \right)^{\frac{\gamma-1}{\gamma}} \right)}, \quad V_{9i} = \sqrt{R \times T_{08}} \sqrt{\frac{2\gamma}{\gamma - 1} \left(1 - \left(\frac{P_9}{P_{09}} \right)^{\frac{\gamma-1}{\gamma}} \right)} \quad (8.2.8)$$

Nozzle exit flow velocity coefficient that measures the extent of viscous flow losses in the exhaust plane which define as C_v . It is the ratio of actual nozzle exit velocity with discharged and non - discharged value.

$$C_v = \frac{V_9}{V_{9i}} \quad (8.2.9)$$

An angularity loss coefficient is the ratio of axial (momentum) thrust to the momentum thrust of an equivalent bell-shaped nozzle which is gross thrust actual. It can be calculated from Equation (8.2.10)

$$F_g = C_A \dot{m}_9 (V_9 - V_{air}) + (P_9 - P_0) A_9 \quad (8.2.10)$$

Ideal gross thrust is calculated from Equation (8.2.11). Finally, nozzle gross thrust is obtained by Equation (8.2.13).

$$F_{gi} = \dot{m}_{8i} \times (V_s - V_{air}) \quad (8.2.11)$$

$$V_9 = \sqrt{R \times T_{08}} \sqrt{\frac{2\gamma}{\gamma-1} \left(1 - \left(\frac{P_0}{P_{08}} \right)^{\frac{\gamma-1}{\gamma}} \right)} \quad (8.2.12)$$

$$C_{fg} = \frac{F_g}{F_{gi}} \quad (8.2.13)$$

Convergent-divergent nozzle with the primary, secondary, and exit flow, each identified with a loss parameter C_D , C_V and C_A . One of the most important factors when designing a nozzle is to determine whether the expansion of the flow. Expansion is an operation that transforms the thermal energy of the combustion into kinetic energy to move an object onward [41].

In an ideal nozzle, the exit pressure (P_9) will be equal to the ambient pressure (P_0). To check the expansion situation of the nozzle, CFD analyzes are examined to see the effect of divergent half-angle value on expansion types in the following sections.

8.2.2 Phoenix Engine Variable Nozzle Geometry Calculation

The MATLAB code prepared by the Phoenix Design Team is used to create the nozzle geometry. The code is derived from isentropic nozzle relationships and Mattingly Aircraft Engine Design source. In order to verify the MATLAB code, the outputs obtained in the design case are compared with the outputs from the GasTurb13 program. Table 31 shows the validation results.

Table 31. Nozzle MATLAB Inputs and Outputs for On-Design Condition

Inputs	Throat Mass Flow Rate \dot{m}_8 (kg/s)	224.847		
	Ambient Pressure P_0 (kPa)	10.039		
	Throat Total Temperature T_{08} (K)	631.23		
	Throat Total Pressure P_{08} (kPa)	119.879		
	Discharge Coefficient C_d	0.95		
	Area Ratio A_9/A_8	2.1443		
MATLAB Outputs		GasTurb13 Outputs		% Dif.
Throat Area A_8 (m ²)	1.2270	Throat Area A_8 (m ²)	1.173	4.6
Throat Radius R_8 (m)	0.645	Throat Radius R_8 (m)	0.611	4.9
Nozzle Exit Area A_9 (m ²)	2.631	Nozzle Exit Area A_9 (m ²)	2.516	4.57
Nozzle Exit Radius R_9 (m)	0.915	Nozzle Exit Radius R_9 (m)	0.896	2.1
Nozzle Exit Mach Number M_9	2.2633	Nozzle Exit Mach Number M_9	2.2632	≈0
Nozzle Exit Velocity (m/s)	806.62	Nozzle Exit Velocity (m/s)	819.44	1.56

As can be seen from Table 31, the generated MATLAB code gives results that very close to the GasTurb13 outputs. Code entries for on-design and off-design conditions to design the convergent-divergent nozzle of the PHOENIX Engine are given in Table 32 below.

Table 32. Input Parameters of Each Mission Profile

Inputs	Mission Profiles		
	Cruise	Take-Off	Climb
Throat Mass Flow Rate \dot{m}_8 (kg/s)	224.847	577.98	224.85
Ambient Pressure P_0 (kPa)	10.039	101.325	21.663
Throat Total Temperature T_{08} (K)	631.23	540.64	557.12
Throat Total Pressure P_{08} (kPa)	119.879	153.841	109481
Discharge Coefficient C_d	0.95	0.95	0.95

Using the inputs given above, configurations for the ideal convergent-divergent nozzle are created by giving values equal to or very close to the atmospheric pressure of the nozzle outlet pressure. Nozzle design parameters for on-design and off-design conditions are given in Table 33 below.

Table 33. Calculated Nozzle Parameters for Mission Profiles (MATLAB)

Parameters	Cruise	Take Off	Climb
Area Ratio A9/A8	2.1443	1.0	1.35
Throat Area A8 (m ²)	1.2331	2.3267	1.2673
Effective Throat Area A8e (m ²)	1.1714	2.2104	1.2040
Nozzle Exit Area A9 (m ²)	2.6442	2.3267	1.7109
Nozzle Gross Thrust Coefficient Cfg	0.9723	0.8713	0.9717
Velocity Coefficient Cv	0.988	0.8274	0.9751
Actual Nozzle Gross Thrust Fg (kN)	467.07	352.53	637.77
Ideal Nozzle Gross Thrust Fgi (kN)	480.36	404.63	656.33
Nozzle Exit Mach Number M9	2.2633	0.80	1.7084
Ambient Pressure P0 (kPa)	10.04	101.325	21.663
Nozzle Exit Pressure P9 (kPa)	119.88	153.753	109.481
Nozzle Exit Velocity V9 (m/s)	806.624	352	644.56

8.2.3 Computational Analysis of the Nozzle Geometry

In GasTurb13, the angle for the convergent part is given as 11.23°. Keeping this angle constant, CFD analyzes will be done by changing the angle of the divergent section. Divergent part half-angle was tested in CFD analysis with 11, 13 and 15 degrees. CFD analyzes were done using the Siemens STAR CCM+ software. The CFD analysis was expected to have a nozzle exit static pressure (P₉) and nozzle exit Mach number (M₉) similar to the nozzle designed with the MATLAB code and also have no flow separation. In order to get faster results from the CFD analysis, since the geometry is symmetrical, 2D-Axisymmetric computational fluid dynamics (CFD) analyzes were performed using the half of the geometry. The mesh is formed with approximately 230000 cells. The mesh properties are Trimmer mesher, prism layer mesher and surface re-mesher. Boundary Conditions could be seen in Figure 43.

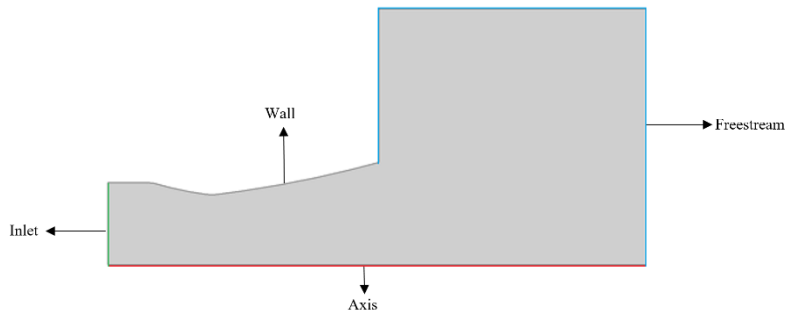


Figure 43. Boundary Conditions of the Nozzle Geometry

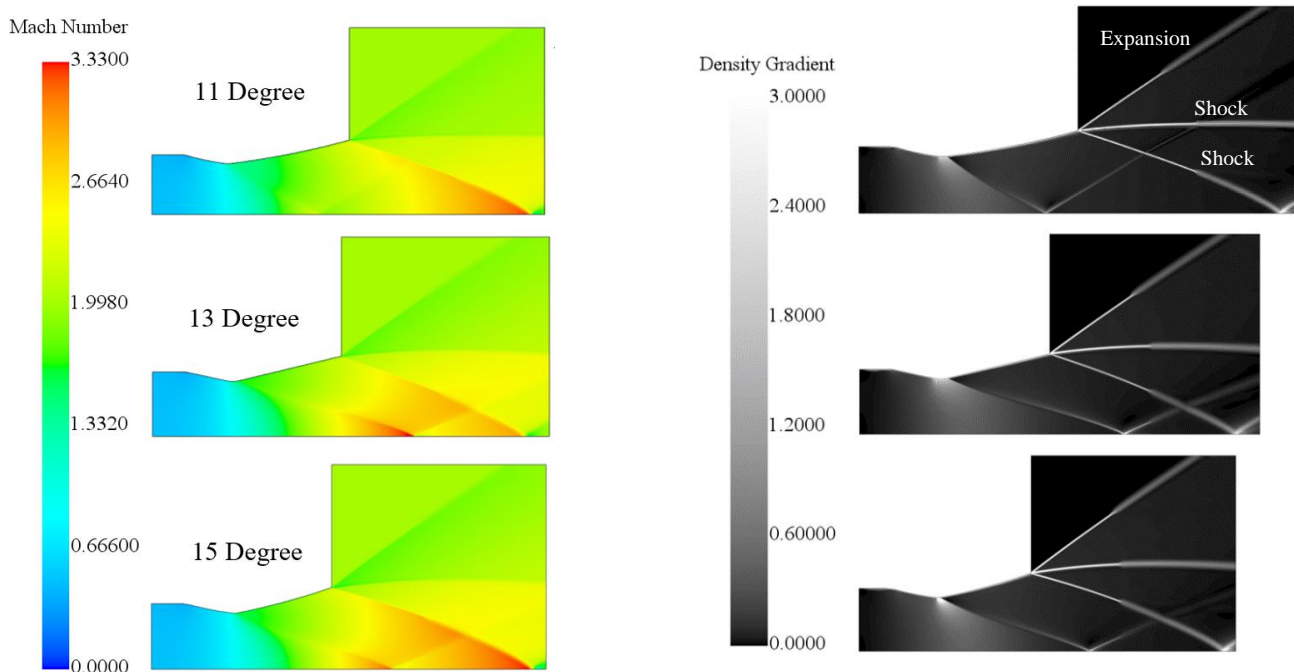


Figure 44. Mach Number and Density Gradient Contours of Geometries with Divergent Section Angles of 11, 13 and 15 Degrees

As can be seen from the analyzes above, no separation occurred in any of the geometries. However, the position of the shock in the nozzle changes. For this reason, differences occur in the values at the output of the nozzle. In Table 34 below, the average Mach number measured at the exit of the nozzle and absolute static pressure values are given.

Table 34. CFD, MATLAB and GasTurb13 Results of the Nozzle

	CFD			MATLAB	GASTURB
	11°	13°	15°	13°	13°
Divergent Angle	11°	13°	15°	13°	13°
Mach Number	2.22	2.24	2.22	2.26	2.26
Absolute Pressure (kPa)	10.5	10.4	10.59	9.7	10.07

As can be seen, the CFD analysis results are close to each other for each angle value. Although the data of the 13° degrees are closer to the MATLAB and GasTurb13 outputs, it was decided to have a nozzle divergence angle of 11° because 11° angle corresponds to a shock-free nozzle case.

8.2.4 Off-Design Operation

Since the noise of the Concorde was a great issue, nozzle exit jet velocity of take-off condition is a big concern. In GasTurb13 software, velocity below 1150 ft/s at 9th station was achieved. To validate this, another CFD analysis were made with similar boundary and mesh conditions to the on-design condition which can be seen in Figure 45.

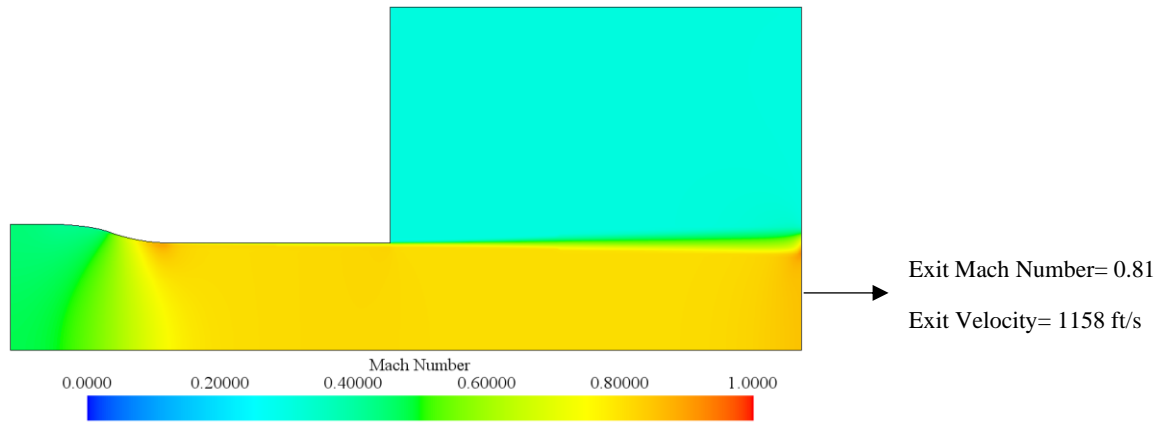


Figure 45. CFD Analysis of Off-Design Condition

From this analysis, velocity and Mach number at station 9 is achieved 1158 ft/s and 0.81, respectively. With that output, the validation can be said to be met.

8.3 Variable Exhaust Nozzle

In fully variable nozzles, different area ratios are obtained by expanding and narrowing the throat and the outlet section to the desired extent. In this way, ideal thrust values are obtained in other off-design conditions, excluding the on-design condition [40]. In addition, in fully variable nozzles, the back pressure value is decreased by increasing the throat area and thus, the power required for engine start-up is possible with lower turbine inlet temperatures with the increase in the expansion ratio [21].

Optimal nozzle geometry can be achieved by variable area fan nozzles for all flight phases. With varying the area of a jet engine's nozzle for varying Mach number, altitude, etc. substantial can optimize fan loading and enhanced fuel consumption and emissions, and also reduction in noise can be accomplished. Varying the fan nozzle area, and thus the ratio of engine bypass is an incredibly efficient way to minimize noise during takeoff and approach [43]. Nevertheless, several studies have shown the most significant factor impacting range is total weight. Hence, it is necessary to reduce additional weight due to noise reduction devices and evaluation of the selection of a complex nozzle should be done, even though it allows for a reduction in jet noise [44].

For these reasons, Variable Geometry Chevrons (VGC) using compact, lightweight and robust thermally activated shape memory alloy (SMA) actuators are chosen. Chevrons are triangular notches in the nozzle exit plane along the rear edge of a jet engine primary and/or secondary exhaust nozzle to control the engine's exhaust flow and suppress noise from both the environment and the shock cell. Moreover, it is possible to significantly minimize jet noise by facilitating advantageous flow mixing with these strip mechanisms. A 2-5 dB reduction in far-field noise can be achieved according to General Sound Pressure Level Measurements (OASPL).

The ability to change the area allows the chevron to enter the flow to reduce noise during take-off and withdraw reduced thrust losses during cruise [45]. Significant advantages can be achieved with exhaust nozzles with area changes of 10-20%, and Boeing has tested a scaled variable area jet nozzle that can adjust the area by 20% [46]. The final geometry of the PHOENIX Engine's nozzle is given in Figure 46.

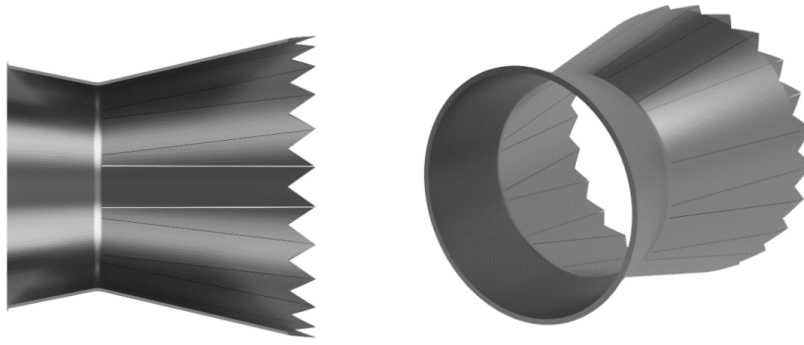


Figure 46. 3-D CAD Model of the ETU-PHOENIX Engine's Nozzle

9. SHAFT DESIGN

The shaft design is the most crucial component in geometric sizing since increasing performance values lead to higher engine temperatures and shaft rotational speeds. Moreover, as engine complexity increases, so do the loading values on the shaft [47,49]. The critical speed of the shaft is one of the most significant parameters in shaft design. The critical velocity of the shaft is defined as the speed at which the natural frequency of objects rotating around their axes expands and axial deviations increase [48].

Operating the shaft near the critical speed value results in unbalanced loads in the engine. It is a critical parameter for the engine's lifecycle. As a result, the shaft should be kept as far away from the critical speed as possible, and operating conditions near the critical speed should be kept as short as possible. Otherwise, this causes a variety of issues within the engine.

The material used for the shaft has an effect on the critical speed of the shaft and hence the system. The shaft should be as light as possible while still being resistant to high temperatures and heavy loads. As a result, before beginning calculations, the shaft material must be selected. Super CMV was selected as a material for the PHOENIX Engine and is discussed in the Material Selection section.

The general shaft structure and bearing numbers for the PHOENIX engine were calculated based on literature surveys, and the number, location, and types of bearings are shown in Figure 47. Pratt & Whitney introduces this shaft concept for Energy Efficient Engines for next-generation engines. This shaft structure is intended to reduce the effects of certain previous engine drawbacks (such as limited aerodynamic options, noise considerations, and mechanical complexity) [52]. Classical roller bearing has been more appropriately chosen in terms of reliability and applicability. Hence, two ball bearings and three roller bearings were selected for the ETU-PHOENIX Engine [50].

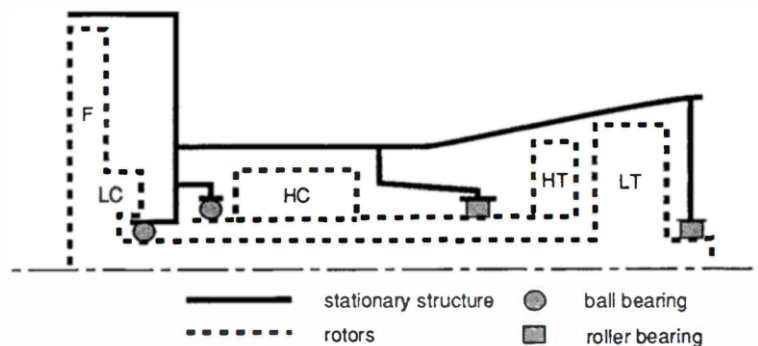


Figure 47. Two Spool Shaft Structure and Bearing Placement [47]

The PHOENIX Engine's shaft is a two-spool shaft, one with a lower RPM for Fan(LPC) stage and one with a higher RPM for HPC and turbine stages. Force and torsion analysis estimated by Equation 9.1 and the results are given in Table 35.

$$T = \frac{SHP \times 63025}{RPM_{shaft}} \quad F = \frac{T}{R_{mid}} \quad (9.1)$$

Table 35. Shaft Design Criterion

Criterion	Hollow Shaft	Solid Shaft	Criterion	Hollow Shaft	Solid Shaft
K_f	2	2	SHP(hp)	33082	20843
K_τ	2	2	RPM_{shaft}	7500	11500
F_s	3	3	T(lbf.ft)	8687.17	7819.22

The dimensions of the shaft can be calculated using Equations 9.2 and 9.3 according to Shigley's and Ugural [51,52].

$$d_{inner(hollow)} = 0.4 + d_{solid} \quad (9.2)$$

$$d_{solid}^3 = \frac{32F_s}{\pi} \sqrt{k_f^2 \left(\frac{M_m}{S_y} + \frac{M_a}{S_e} \right)^2 + k_{fs}^2 \left(\frac{T_m}{S_y} + \frac{T_a}{S_e} \right)^2}, \quad d_o = \frac{d_o^4 - d_i^4}{\frac{128F_s}{\pi} \sqrt{k_f^2 \left(\frac{M_m}{S_y} + \frac{M_a}{S_e} \right)^2 + k_{fs}^2 \left(\frac{T_m}{S_y} + \frac{T_a}{S_e} \right)^2}} \quad (9.3)$$

For shaft critical speed calculations, there are two different approaches. These are the Dunkerley's Method and the Rayleigh-Ritz Method. Calculations in this project were performed using both Dunkerley's and Rayleigh-Ritz's methods. While the Dunkerley method was used to calculate the shaft's lower limit speed, the Rayleigh-Ritz method was used to determine the shaft's upper limit speed.

Dunkerley's and Rayleigh-Ritz methods' mathematical expressions are given in Equations 9.4 and 9.5 respectively.

$$\omega_{ii} = \sqrt{\left(\frac{g}{w_i \delta_{ii}} \right)} \quad \frac{1}{\omega_1^2} \approx \sum_{i=1}^n \delta_{ij} \frac{1}{\omega_{ii}^2} \quad (9.4)$$

$$\omega_{critical} = \sqrt{\left(\frac{g \sum_{i=1}^n \omega_i y_i}{\sum_{i=1}^n \omega_i y_i^2} \right)} \quad (9.5)$$

The shaft critical speed calculations were performed with the help of a newly developed MATLAB code. Using the superposition technique, different MATLAB codes were written for each shaft. While the length and diameter of each shaft were determined from the GasTurb 13, the properties of each segment were determined using AxSTREAM. The codes were validated using sample cases from the literature surveys. Ball and roller bearings on the compressor side's low spool shaft are considered cantilever in these codes. The critical speeds of the compressor shaft and the other shaft which the tribune is connected are calculated separately. As a result, the critical speed with the lowest value was selected.

Table 36. MATLAB Results of the Each Shaft

	HP Spool Shaft	LP Spool Shaft
Dunkerley's Method (rpm)	12786	6030
Rayleigh's Energy Method (rpm)	12855	6338
Inner Diameter(in)	3.5	-
Outer Diameter(in)	6.5	3.25

The inner diameter of the shaft is selected as 3.5 in instead of the formula result 3.27 in, the outer diameter of the solid shaft is selected as 3.25 in instead of 3.23 and the outer diameter of the hollow shaft is selected as 6.5 in instead of 6.33 in because of the commercial concerns. Technical properties of the lubricant oil BPTO-219743 are given in Table 37 [53].

Table 37. Technical Properties of BPTO-219743

Parameter	Unit	BPTO-219743
Density at 520 R	lbm/in ³	0.0360
Kinematic Viscosity at 672 R	in ² /s	0.0082
Kinematic Viscosity at 564 R	in ² /s	0.042
Kinematic Viscosity at 420 R	in ² /s	0.020
Pour Point	R	389.07
Flash Point	R	963.27

3-D drawings of the PHOENIX Engine's shaft are given in Figure 48.

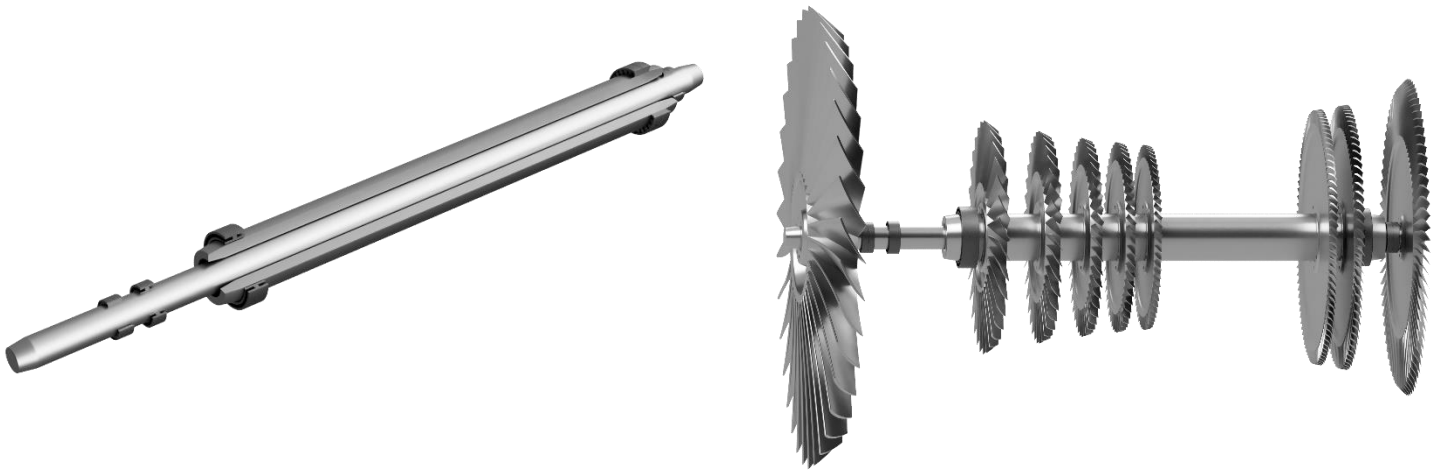


Figure 48. 3-D CAD Drawing of the Shaft (Left), 3-D CAD Drawing of the ETU- PHOENIX Engine's Rotors (Right)

10. BLADE ANALYSIS

In the preceding pages, streamline analyses for turbomachinery are conducted using aerodynamic design principles, and temperature, strain, and Mach number distributions are obtained, as well as blade designs. Aside from aerodynamic requirements, rotor and stator blades at each stage of the compressor, as well as rotor blades at each stage of the turbine, are subjected to a range of pressures such as thermal, bending, vibrational, and centrifugal due to high rotational speed and temperature [14]. However, of these stresses, centrifugal stress caused by high rotational speed is the most dominant and essential for turbomachinery construction. As a result, rotor and stator blades are in the safety margin under centrifugal loading if the acceptable stress value of the chosen material for the blade is higher than the measured stress value [14]. Allowable centrifugal force on turbomachinery blades is calculated using Equation 10.9 [54]

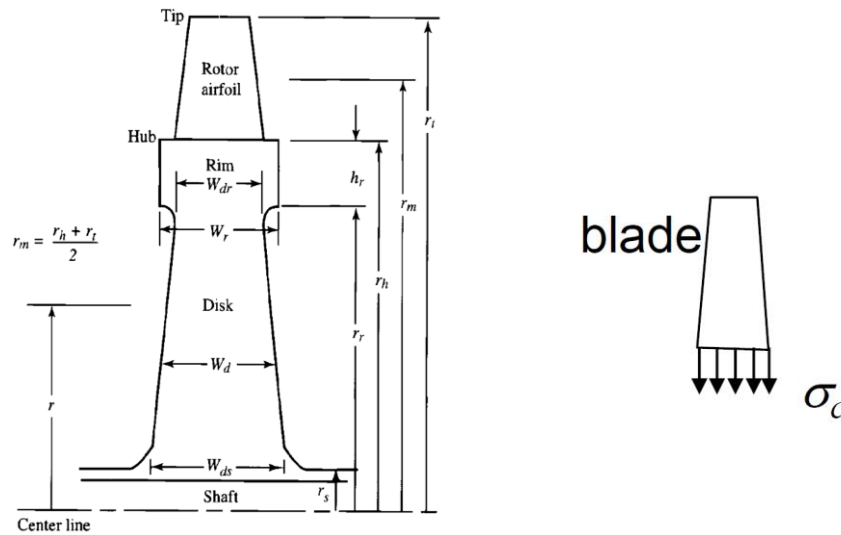


Figure 49. Rotor Nomenclature (left) and Centrifugal Stress on a Blade (right)

Maximum stress occurs at the rotor blade hub. This stress can be calculated using equation 2

$$\sigma_c = \frac{F_c}{A_{hub}} \quad (10.1)$$

And the centrifugal stress force can be calculated using Equation 2

$$F_c = \int_{r_h}^{r_t} \rho_{blade} A_{blade}(r) \Omega_{shaft}^2 r dr \quad (10.2)$$

Combining Equation 10.2 and Equation 10.3:

$$\frac{\sigma_c}{\rho_{blade}} = \Omega^2_{shaft} \int_{r_h}^{r_t} \frac{A_{blade}(r)}{A_{hub}} r dr \quad (10.3)$$

$$\frac{A_t}{A_h} \equiv Taper Ratio \quad (10.4)$$

With linear taper assumption:

$$\frac{\sigma_c}{\rho_{blade}} = \Omega^2_{shaft} \int_{r_h}^{r_t} \left[1 - \frac{r - r_h}{r_t - r_h} \left(1 - \frac{A_t}{A_h}\right)\right] r dr \quad (10.5)$$

Integrating:

$$\frac{\sigma_c}{\rho_{blade}} = \Omega^2_{shaft} (r_t - r_h) \left[\left(\frac{r_t + 2r_h}{6}\right) + \frac{A_t}{A_h} \left(\frac{2r_t + r_h}{6}\right) \right] \quad (10.6)$$

Assuming:

$$r_t + 2r_h \cong r_h + 2r_t \cong 3r_m \quad (10.7)$$

$$A_z \cong 2\pi r_m (r_t - r_h) \quad (10.8)$$

Resulting:

$$\frac{\sigma_c}{\rho_{blade}} \cong \Omega^2_{shaft} \frac{A_z}{4\pi} \left(1 + \frac{A_t}{A_h}\right) \quad (10.9)$$

Now the AN^2 rule can be used to check the turbine blades' stresses, which is shown in Equation 10.9. AN^2 rule is a design limit for a turbine material at maximum temperature. Its typical values for traditional turbines are in $0.5 - 10 \times 10^{10} \text{ in}^2 \text{ RPM}^2$ range.[24]

$$AN^2 = \Omega^2_{shaft} \times A \times \left(\frac{30}{\pi}\right)^2 \quad (10.10)$$

For turbomachinery components, the taper ratio ranges between 0.8 and 1 [14]. AxSTREAM measures the taper ratio for each blade. Each component's material selection is outlined in the material section. PC [55] is chosen as a material for Fan Blade Design to minimize weight while increasing power. TMC (Titanium Matrix Composite) [56] is chosen as a material for HPC Blade Design to minimize weight while increasing strength. Table 38 shows the stress analysis results due to centrifugal loading and the parameters defined in Equation 10.9.

Table 38. Fan and Compressor Blades' Properties [55,56]

Part Name	Fan R1	Fan S1	HPC R1	HPC S1	HPC R2	HPC S2
Material	Polyimide Composites	Polyimide Composites	Ti-45Al-8Nb	Ti-45Al-8Nb	Ti-45Al-8Nb	Ti-45Al-8Nb
Material Density (lbm/in ³)	0.04805	0.04805	0.14	0.14	0.14	0.14
Allowable σ_c (ksi)	287	287	90.65	90.65	90.65	90.65
Rotation Speed (rpm)	7500	-	11500	-	11500	-
Taper Ratio	0.8	-	0.8	-	0.8	-
Flow Area (in ²)	2947.94	-	641.21	-	418.89	-
Design σ_c (ksi)	32.418	-	48.30	-	31.56	-

Part Name	HPC R3	HPC S3	HPC R4	HPC S4	HPC R5	HPC S5
Material	Ti-45Al-8Nb	Ti-45Al-8Nb	Ti-45Al-8Nb	Ti-45Al-8Nb	Ti-45Al-8Nb	Ti-45Al-8Nb
Material Density (lbm/in ³)	0.14	0.14	0.14	0.14	0.14	0.14
Allowable σ_c (ksi)	90.65	90.65	90.65	90.65	90.65	90.65
Rotation Speed (rpm)	11500	-	11500	-	11500	-
Taper Ratio	0.8	-	0.8	-	0.8	-
Flow Area (in ²)	276.07	-	188.35	-	132.58	-
Design σ_c (ksi)	20.80	-	14.19	-	9.98	-

The critical stress value in the turbine, as in the compressor, is caused by centrifugal loadings caused by high rotational speed and also the thermal stress. The flow area in the turbine is gradually increasing, allowing the flow to expand. As a result, the turbine in the final stage has

the highest flow field. Table 39 shows the stress analysis findings for the final stage of HPT and LPT due to centrifugal charge. Detailed material properties are given in the MATERIAL SELECTION section.

Table 39. Turbine Blades' Properties [57,58,59,60]

Part Name	HPT S1	HPT R1	HPT S2	HPT R2	LPT S1	LPT R1
Material	TMS-238	TMS-238	TMS-238	TMS-238	TMS-238	TMS-238
Material Density (lbm/in ³)	0.33	0.33	0.33	0.33	0.33	0.33
Allowable σ_c (ksi)	150.9	150.9	150.9	150.9	150.9	150.9
Rotation Speed (rpm)	-	11500	-	11500	-	7500
Taper Ratio	0.80	0.80	0.80	0.80	0.80	0.80
Flow Area (in ²)	-	286.99	-	451.42	-	731.67
Design σ_c (ksi)	-	50.97	-	80.14	-	129.9
$AN^2[in^2 \times rpm^2 \times 10^{10}]$	2.22	2.97	3.86	4.69	3.92	5.01

11. MATERIAL SELECTION

One of the most important processes in extending turbine efficiency is material selection. Furthermore, material selection has an important effect on the engine's life cycle. As a result, the engine's last estimated lifetime for each part should be acknowledged. Furthermore, a good engine design must satisfy its aerodynamic, thermodynamic, and structural requirements. The advancement in material technology limits the ability to boost the performance of gas turbine engines. As a result, new materials are continuously being designed for more effective, long-lasting, and strength-reliable gas turbines. Over the last 60 years, technological advancements have made tremendous advances in the field of materials. Along with improved mechanical and thermal properties provided by new materials, the fuel consumption of subsonic engines is decreased by around 40%, and the maximum turbine entry temperature is increased from 1440R to over 3400R.

The engines' overall pressure ratio was increased from 5 to 40. Then, stress fracture life and creep properties were studied. Because of their material properties, all components on the engine are limited to particular variable loads, and scientific studies are based on potential faults in these components [62]. The materials used in the construction of the PHOENIX Engine were chosen based on extensive research and historical experience. New materials that are expected to replace them by 2028 are being considered for material selection. As seen in Figure 50, preferred materials such as CMC, PC, CFRP, Titanium, and Aluminum are widely used today.

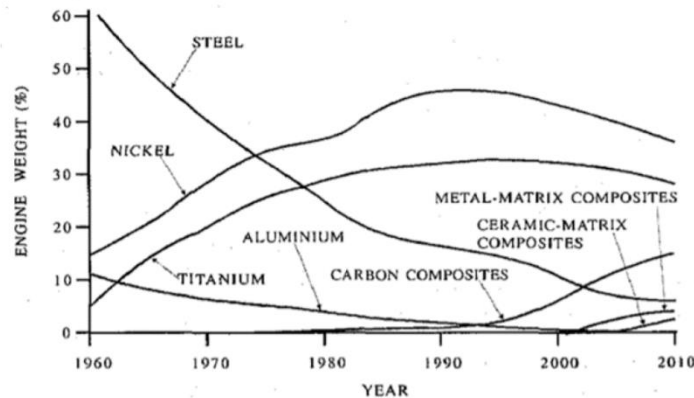


Figure 50. Materials used in engine structure through the years [57]

11.1 Inlet Materials

The rate of air mass flow is determined by the efficiency of the engine intake. Such performance is obtained by proper geometry design and accurate production. The materials used in the inlet should be able to withstand high temperatures, particularly at supersonic speeds [63].

Carbon fiber reinforced polymer is a fiber-reinforced composite that is incredibly durable and light. Composite materials reinforced with carbon fiber vary from conventional FRP composites produced with fiberglass or aramid fiber. CFRP materials provide significant benefits to aircraft design by minimizing weight and fuel consumption, increasing payload, expanding flight range, improving toughness and durability, optimizing design, reducing component count, lowering maintenance costs, and maximizing passenger comfort and safety. A major advantage of carbon fiber reinforced Pre-pregs over Aluminum is their improved fatigue strength [63]. More than half of the components used in the Boeing 787 and Airbus A350 XWB airframes (ailerons, panels, flaps, upper deck floor beams, wing ribs, etc.) are carbon fiber composite. CFRP is a significant material for programs, and Airbus has awarded it the contract to provide the primary structure Pre-preg for the A350 XWB program [64]. CFRP components passed both field and flight checks with success. In addition, the Rolls-Royce Trent series has begun to use CFRP components. As a result, the PHOENIX Team chose CFRP as an inlet material, the mechanical properties of which are seen in Table 40.

Table 40. Inlet Material Properties [65]

Selected Material	CFRP
Density (lb/in³)	0.058
Maximum Operation Temperature (R)	747
Young Modulus (ksi)	10150
Yield Strength (ksi)	170

11.2 Compressor Materials

Polyimide resin has outstanding heat resistance and mechanical properties, and it has long been the focus of research on high-temperature-resistant composite materials for the aerospace industry. The epoxy resin has a long-term working temperature of no more than 725R, the Bismaleimide resin has a temperature range of 490-900R, and the polyimide resin has a temperature range of 995-1300R. P2SI900HT, a fourth-generation organic-inorganic hybrid polyimide composite resin matrix with a temperature resistance of 1300R, was the first material grade to be developed. The glass transition temperature is as high as 880R (Tan δ), and it can be used at temperatures of 1250R for a long period of time, as well as at temperatures as high as 1960R. The properties of the P2SI900HT polyimide composite are given in Table 41. Also, these fan blades have a titanium leading edge for extra protection. Ti-6Al-4V that has a low density and is used in implants and aviation was added to protect FOD. Table 41 displays the mechanical properties of a chosen coating substance.

The compressor is the part of the system that compresses the air from the fan and raises the temperature. Phoenix also has a pressure ratio of more than 15 and the temperature of the compressor outlet is about 1620 Rankine. Under these conditions, materials with high strength must be used for high temperatures. Furthermore, the material used must be fatigue, crack, oxidation, and creep resistant. Titanium-beta-alloys may be recommended because the temperature in the compressor is higher than the fan, for example, Ti-45Al-8Nb with a maximum service temperature of 2111 R. Ti-45Al-8Nb alloy used in also such as disc material. Since blisk technology will be used, it has been deemed appropriate to use the same material in the disc and blades. In this case, nickel-based alloys might be considered, but this material, which is heavier than titanium, cannot be used in blades that rotate quickly. For compressor blades, the Ti-45Al-8Nb material was chosen, which is a titanium alloy with a strong strength of up to 2340 R. To increase corrosion resistance, chromium was also added. Table 41 describes the mechanical properties of the materials selected.

Table 41. Compressor Material Properties [55]

Component	Fan (LPC)	Fan (Coating)	HPC
Selected Blade Material	PC	Ti-6Al-4V	Ti-45Al-8Nb
Density (lb/in³)	0.04805	0.16	0.14
Maximum Operation Temperature (R)	1256	1170	2111 R
Young Modulus (ksi)	20000	16530	26106 ksi
Yield Strength (ksi)	287	160	90.65 ksi

11.3 Combustion Chamber Materials

Temperatures in the combustion chamber rise to dangerously high levels. As a result, the combustion chamber's wall temperature should be lower than the material's melting point. Hasteloy X, Nicomic 75, Nicomic 263, HA18 (cobalt-based-superalloy) materials used in Pratt & Whitney F100 engines, and Inconel 625/718 have long been common materials for combustion chambers. HA188 stands out from the competition with higher temperature strength and strong oxidation resistance up to 2460R, which is in line with the evolving technology. The base material could be a cobalt-based superalloy like HA188, and ultra-lightweight CMC (Ceramic Matrix Composite) tiles could be used to avoid high temperatures at the start of the burner liner. This approach was used in the GE9X test flight, which was the first of its kind in the world. With the use of CMC, it is now possible to increase operating temperatures without incurring the costs associated with increased cooling air use. Due to their high thermal conductivity, excellent thermal shock, creep, and oxidation resistance, Si-C matrix composites are ideal materials for gas turbine engines. As a result, the combustion chamber material is Sylramic-iBN, which was designed by NASA for ultra-high temperature applications, and C/SiC is favored for both temperature resistance and weight [57, 68, 69]. Since a highly stable and safe hafnium silicate forms at the surface, it can operate at higher temperatures than silicon carbide in an oxidizing environment. [70, 71] Layered Hafnium Carbide/Silicon Carbide with a coating of Yttriumstabilized Zirconium was chosen as the combustion chamber material as a result of these searches and evaluations. Ceramic-based Tantalum Carbide (known to be used in the F-35 and GE-9X) was tested for this coating procedure. However, due to its high cost, this material is not suitable. Because of the structural and thermal properties of SiC, Yttrium-Stabilized Zirconium can withstand high temperatures up to 4200 R. Despite their costs, both materials are thought to be good choices. As a consequence, maintenance costs will be minimized. To reduce the temperature in the insulation layer and prevent high temperature streaking, a thermal barrier coating (based on ZrO₂ – Y₂O₃ and developed by plasma spraying) with a temperature resistance of +360-540 R is also used. Table 42 lists the mechanical properties of various materials.

Table 42. Compressor Material Mechanical Properties [72,73]

Selected Material	C/SiC CMC (hafnium layered)
Density (lb/in ³)	0.0722
Max. Service Temperature (R)	4451.2
Tensile Strength (psi)	0.79×10 ⁶
Selected Coating Material	Yttrium-Stabilized Zirconium
Density (lb/in ³)	0.22
Max. Service Temperature (R)	4239

11.4 Turbine Materials

Since they are subjected to high temperatures and stresses, the first set of turbine blades must be temperature and pressure resistant. As a result, the material used for turbine components should be thermally and mechanically resistant. The temperature and creep strengths of 4th and 5th generation superalloys are very good. Despite their strong properties, they have poor oxidation resistance due to refractory elements like Mo, Re, and Ru. High-temperature creep and oxidation-resistant 6th generation superalloys have been developed [74]. CMSX-10, TMS-138, TMS-196, and TMS 238 are examples of different generation superalloy materials that compared for PHOENIX Engine. These materials were subjected to the necessary investigations. Oxidation resistance, creep rate, temperature power, and mechanical strength were calculated as selection parameters under high temperature and pressure. The graphs below (Figure 51) show mass change over one-hour cycles, metal loss in hot corrosion tests, and creep-rupture life vs. oxidation resistance for various materials. As a result of these investigations, the 5th generation single crystal super alloy TMS-238 was chosen as a material for high and intermediate pressure turbine blades [57,74,59,75].

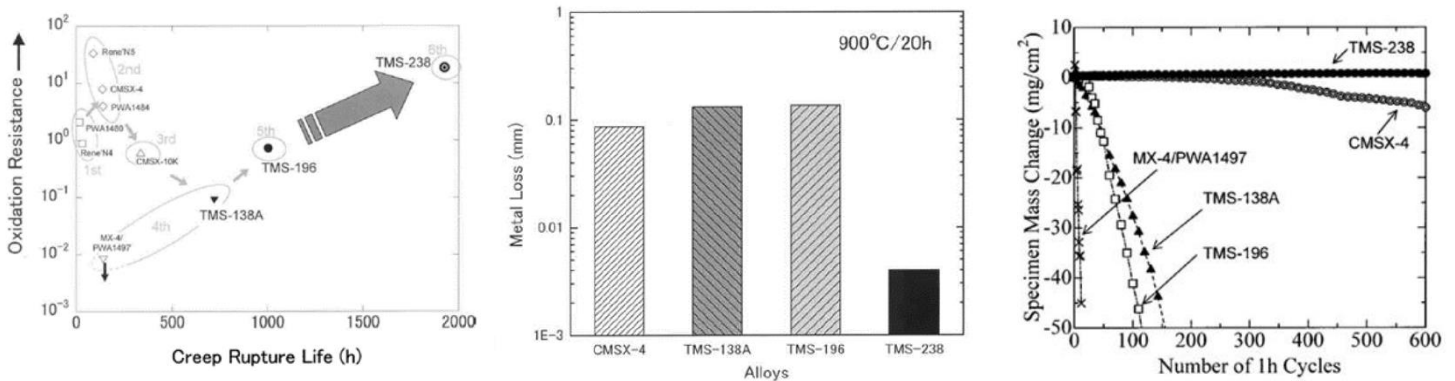


Figure 51. Alloy Comparisons Based on a Combination of Creep and Oxidation(left) & Hot-Corrosion Test Results (middle) and Tests for Cyclic Oxidation (right) [61]

11.5 Mixer-Nozzle Materials

Throughout the mission, the nozzles are exposed to a variety of temperatures. For nozzles and exhausts, Inconel, stainless steel alloys, Hastelloy X, and CFRPs are commonly used. Because of their corrosion resistance and capacity to endure extremely high temperatures, Inconel (nickel-chromium-iron) alloys are commonly used in turbine engines. In comparison to FSX414, the alloy has a significantly higher creep strength. N155, an iron-based superalloy with strong weldability, is used in some GE engines' later stage nozzles. The key points of materials used for nozzles today are mentioned in Table 43. [57] PHOENIX design team decided to use an N155 as a mixer nozzle material.

Table 43. Frequently used nozzle materials by GE, P&W, RR [57]

Grade	Chemical Composition	Remarks
X40	Co-25Cr10Ni8W1Fe0.5C0.01B	Cobalt-base super alloy
X45	Co-25Cr10Ni8W1Fe0.25C0.01B	Cobalt-base super alloy
FSX414	Co-28Cr10Ni7W1Fe0.25C0.01B	Cobalt-base super alloy
N155	Fe-21Cr20Ni20Co2.5W3Mo0.02C	Iron-base super alloy
GTD-222	Ni-22.5Cr19Co2.0W2.3Mo1.2Ti0.8Al0V0.008C1.0B	Nickel-base super alloy

11.6 Shaft Materials

The Phoenix shaft is made of heat-treated steel, such as Super CMV (Chrome-Molybdenum-Vanadium). The next-generation engine design is attempting to replace the primary shaft with F1E, an iron-based superalloy that is expected to be used in future Rolls-Royce engines until 2025. Centrifugal force is produced by rotating components and shafts on the inner ring, causing tensile stress.

M50NiL, which is resistant to high temperatures and has strong fracture-corrosion and mechanical shock resistance, was chosen as a bearing material for Phoenix to solve this issue. [76,77]

Table 44. Component-Material Overview

Component	Operation Temperature	Material	Allowable Service Temperature
Inlet		Carbon Fiber Reinforced Poylmer (CFRP)	~720-900R
Fan	~ 717.9R	PC (Polyimide Resin) and Ti-6Al-4V Coating	~995-1300R ~1170-1260R
Compressor	~1619.65R	Ti-45Al-8Nb	~1575R-2160R
Combustion Chamber	~4500R	C/SiC CMC and Yttrium-stabilized Zirconium Coating (Thermal Barrier): ZrO ₂ – Y ₂ O ₃	~4320R-4500R
Turbine	~2744R	TMS-238 and MCrAlY Coating	-
Mixer-Nozzle	~1658R	N115	-
Shaft	-	Super CMV	-
Bearing	-	M50NiL	-

12. WEIGHT ANALYSIS OF THE PHOENIX ENGINE AND OLYMPUS 593

One of the critical design parameters is engine weight during the new engine design. Optimization of overall engine weight provides decrement in fuel consumption and increment of flight range. A detailed literature survey was conducted through this examination. Among several correlations, the WATE++ correlation developed by Boeing and NASA is chosen for giving the best solutions compared to real results. This correlation uses overall pressure ratio (OPR), bypass ratio (BPR) and mass flow rate through the core [2]. A simplified version of the program was obtained from a report because the program is not open source Equations 12.5 and 12.6. After having a weight analysis of Engine Phoenix, the base engine (Olympus 593) has to be analyzed in order to compare how much weight is optimized. Due to the fact that Olympus 593 turbojet engine was built in the 1960s, there is a different correlation from a new designed engine, which is assumed to be applied to engines built in the late 1990s through the mid-2000s Equations 12.1-12.2-12.3 [79]. Real mass and correlation mass are defined exactly, so there is such a coefficient called weight coefficient which is defined as W_{CAD}/W_{real} . This ratio must be kept constant during the Engine Phoenix weight analysis. In Table 45, $W_{CAD}(W_{real})$ is obtained from the whole 3D Model of the Engine Phoenix in Solidworks software and assigned materials with related components. So level of difference between real and correlation weight could be seen. Also, the density, volume and weight of each component are stated in detail in Table 46. To sum up, overall engine weight was developed from 7000 lbm to 5640 lbm with a low-bypass turbofan engine which can be seen in Table 46.

Table 45. Engine ETU-PHOENIX and Base Engine Weight Analysis Parameters and Results

Design Parameters	Base Engine	PHOENIX
Core Mass Flow Rate (lb/s)	289,345	165,211
OPR	11,7711	15.535
BPR	0	1.99
$W_{CAD}(W_{real})$ (lbm)	7000	5640
$W_{correlation}$ (lbm)	5419	3438.7
Weight Coefficient	1.64	1.64
% Error	6.85	6.85

$$W_{engine} = a * \left(\frac{\dot{m}_{core}}{100}\right)^b * \left(\frac{OPR}{40}\right)^c, \quad \text{Weight Coefficient} = W_{CAD}/W_{correlation} \quad (12.1)$$

$$\begin{aligned} a &= (-6.590 \times 10^{-1})BPR^2 + (2.928 \times 10^2)BPR + 1915 = 1915 \\ b &= (6.784 \times 10^{-5})BPR^2 - (6.488 \times 10^2)BPR + 1.061 = 1.061 \\ c &= (-1.969 \times 10^{-3})BPR + 0.0711 = 0.0711 \end{aligned} \quad (12.3)$$

$$\begin{aligned} W_{wate}(Base\ Engine) &= 5419\ lbm \\ f_{correction} &= \frac{W_{baseline_{real}}}{W_{baseline_{wate}}} = 1.29 \end{aligned} \quad (12.4)$$

$$\begin{aligned} a &= (-6.204 \times 10^{-1})BPR^2 + (2.373 \times 10^2)BPR + 1702 = 2174.12 \\ b &= (5.845 \times 10^{-5})BPR^2 - (5.866 \times 10^2)BPR + 1.045 = 1.03356 \\ c &= (-1.918 \times 10^{-3})BPR + 0.0677 = 0.0639 \end{aligned} \quad (12.5)$$

$$\begin{aligned} W_{wate}(Pheonix) &= 3439\ lbm \\ W_{phoenix_corrected} &= f_{correction} \times W_{phoenix_wate} \end{aligned} \quad (12.6)$$

Table 46. Physical Properties and Mass at Each Components

Component	Density (lb/in ³)	Material	Volume (in ³)	Mass (lbm)
Shaft	0.287	Super CMV	2148	616
LPC	0.04805	CP	3867	185.8
HPC	0.14	Ti-45Al-8Nb	1727	241.9
CC	0.0722	CMC	602	43.49
HPT	0.33	TMS 238	1063	351
LPT	0.33	TMS 238	671	221.5
Casing (Cold)	0.1	Hiiuminium RR58	31437	3143
Casing (Hot)	0.16	Ti-6Al-4V	3870	619
Mixer	0.296	N 155	731	216.6
TOTAL				5640

The calculations for weight estimation were performed by multiplying the volumes of components taken from 3D CAD files with the densities of the selected materials and using formulas derived from WATE ++ correlation. In order to be more conservative, the heavier result, which is obtained from the 3-D CAD files, is determined as the weight of PHOENIX.

13. ENGINE SUBSYSTEMS

13.1. Lubrication System

Lubrication is of paramount importance wherever there are moving parts. The presence of many moving parts in an aircraft engine reveals the necessity of lubrication for the performance and safety of the engine. Another benefit of the lubrication system is that it reduces the operating temperature of the engine by drawing heat from the engine. Turbofan engine the lubrication system functions could be summarized as lubrication of rotor bearings, removing the contaminants from the lubricant, cooling of the bearings especially in turbine area and supplying a squeezed film between the outer bearing races and their housings for oil-dampened bearings [83]. Some features that should be considered in the selection of lubricants which are the thermal, oxidation and corrosion stability, viscosity, and pressure resistance of the lubricant, pour and flash point of the lubricant [83]. Therefore, lubricants used in commercial jet aircraft are subject to SAE-5780 standards.

Two different lubrication systems, wet-sump and dry-sump systems, are used in aviation. Wet-sump engines store the lubricating oil in the engine or gearbox and dry-sump engines use an external tank mounted on the engine or somewhere in the aircraft structure near the engine. Dry sump systems are widely used in aviation. This is due to some of the disadvantages found in wet sump systems. Wet-sump systems have some disadvantages in terms of the challenge of cooling the lubricant continuously subjected to the engine temperature and the oil supply is limited by the sump capacity. Since the tank is mounted separately from the engine in dry sump systems, it has more storage space and is, therefore, easier to hold the oil at the optimum temperature. Dry-sump and wet-sump lubrication systems are shown in Figure 52.

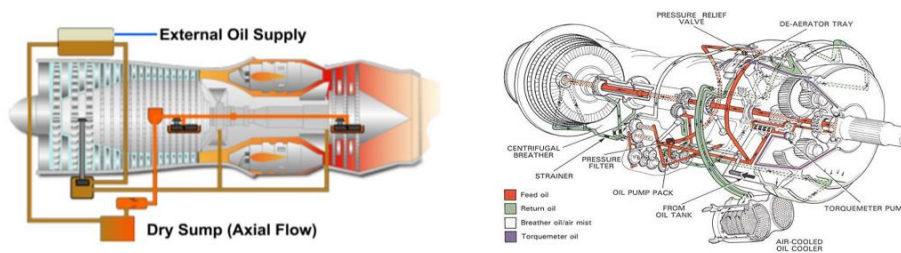


Figure 52. Dry-sump Lubrication Systems (left) [2], Wet-sump Lubrication Systems (right) [82]

Considering the research and the advantages mentioned above, it was decided to use the dry-sump lubrication system in PHOENIX.

13.2. Oil Cooling

During lubrication, the heat generated in the parts in the engine passes to the lubricant. This heat transferred to the lubricant must be kept within certain temperature limits in order not to affect the operation of the engine. Therefore, it is necessary to use an oil cooler system. There are two different types of heat exchangers commonly used, namely air-cooled and fuel cooled heat exchangers. Generally, fuel-cooled heat exchangers are used in turbofan engines [83].

13.3. Anti-Icing System

Due to extremely cold-water droplets in the clouds during the flight and frost fog before take-off, the icing on the fan rotor and the leading edge of the intake may occur. The airflow is disrupted by the ice on the inlet, which often causes vortices. These vortices could affect compressor activity, causing a stall and surge. Anti-icing systems should be used because icing has a detrimental impact on engine performance [85]. For these reasons hot-air anti-icing system is chosen which are given in Figure 53.

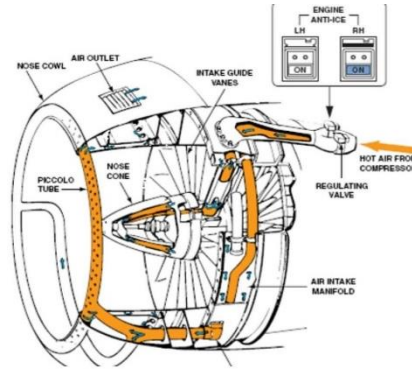


Figure 53. Hot Air Anti-Icing System [84]

13.4. Auxiliary Power Unit

Aircraft could meet the electrical and hydraulic power requirements from the engine during flight. On the other hand, when the aircraft is on the ground, the required energy cannot be provided because the engines shut down, such as when the passengers can get on and the luggage can be placed. Energy is needed to keep the compartment at a certain temperature where the passengers sit and to avoid any discomfort. Today, in most aircraft, this energy problem is solved by the Auxiliary Power Unit (APU) placed inside the aircraft.

It is a small gas turbine designed to meet some of the aircraft's requirements. APU is a self-contained unit that makes the aircraft independent of external pneumatic and electrical power sources. On the ground, APU supplies bleed air for starting the engines, bleed air for the air conditioning system and electrical power to the electrical system. During take-off, APU supplies bleed air for air conditioning. The reason is that it is to prevent any loss in thrust force during the take-off of the aircraft. During cruise conditions, APU helps the electrical system, air conditioning and can be used to restart the engine in undesirable situations such as the engine shut down in the air [86,87]. Considering all these, it was decided to use APU in PHOENIX.

13.5. Engine Starter Systems

Most aircraft engines need assistance to get started. The starter should rotate the engine up to a speed that provides sufficient air flow through the engine to ignite the fuel and then continue to help the engine reach a self-sustaining speed. There are several techniques used in modern engines, such as electric motors, starter/generators, and air turbines. Air turbine starters have some advantages compared to other techniques. They are designed to provide high starting torque from a small, light source. Due to the reasons and advantages mentioned above, it was decided to use an air turbine starter in PHOENIX [88,89]. Figure 54 shows air turbine starters schematically.

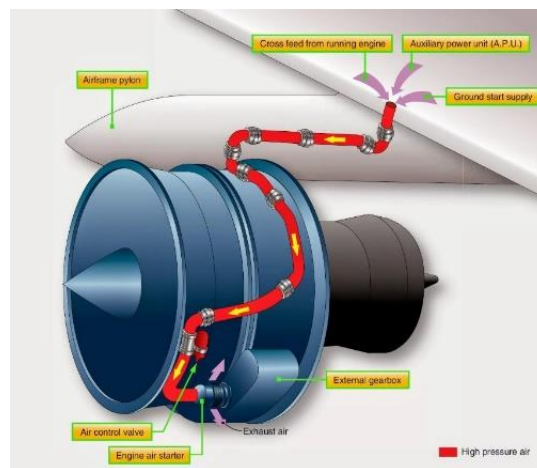


Figure 54. Air Turbine Starters [88]

13.6. Engine Control Systems

Full Authority Digital Engine Control (FADEC) is the system used in almost all aircraft engines to controlling the engine. This system manages the entire engine independently from start-up to shut down. It does not need any mechanical rod or steel cable connection between the cockpit and the engine. FADEC systems have many advantages arising from being digital such as lighter, less bulky, and require less maintenance than old control systems and increase fuel efficiency and reduce maintenance costs. Due to its many advantages, it was decided to use FADEC as the motor control system in PHOENIX. The FADEC system is given in Figure 55 [90,91].

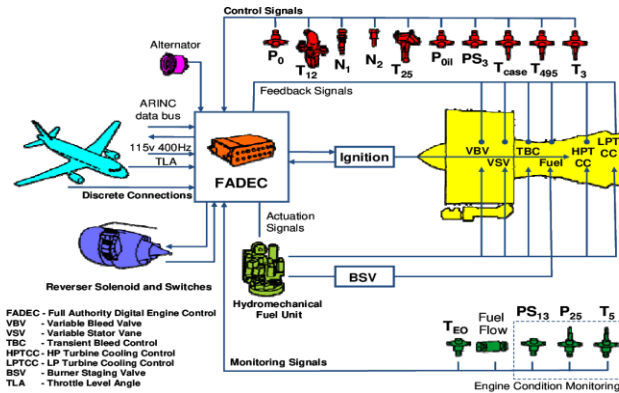


Figure 55. FADEC System [92]

13.7. Fire Detection and Extinguishing Systems

Fire protection systems in aircraft are divided into two main headings. These are fire detection system and fire extinguishing system. The fire detection system, which consists of high-temperature detection and smoke detectors, is used to warn the flight crew in case of high temperature or fire in the aircraft. Smoke detectors are placed in the cargo, toilets, and avionics compartments and high-temperature detectors are in the aircraft compressor, APU, landing gear housing, and pneumatic device tubing [93,94]. Fire Extinguishing System could be seen in Figure 56.

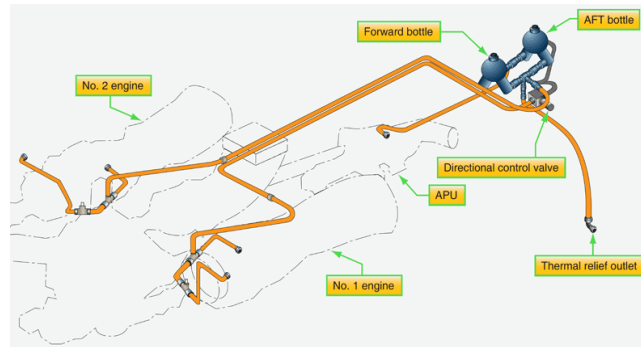


Figure 56. Fire Extinguishing System [95]

14. EMISSIONS

The International Civil Aviation Organization's (ICAO) Committee on Aviation Environmental Protection makes NOx pollution regulations (CAEP). The certification process is dependent on the LTO Cycle (Landing Take-Off). The following are the NOx emission standards for turbojet and turbofan engines designed for supersonic propulsion based on ICAO Annex 16 Volume 2 information [96].

$$Emission\ Standard\ (ES) = \frac{Dp}{F_{00}} = 36 + 2.42 * \pi_{\infty} \quad (14.1)$$

Also, the correlation between the sNOx (NOx severity parameter) and the emission index used in calculations is stated as following [2]. Correlation constants and default values are stated in Table 47.

$$EINOx = (a + b * e^{c*T_3}) * \left(\frac{P_3}{P_{3,ref}}\right)^d * e^{f*h} * \left(\frac{\Delta T_{comb}}{194\ K}\right)^{TF} \quad (14.2)$$

Table 47. Proposed NOx Emissions Correlation Constant and Exponent Default Values for RQL Combustor [97]

a	b	c	d	f	TF	P _{3,ref} (kPa)	ΔT _{comb} (K)	h
8.4	0.0209	0.0082	0.4	19	0	3000	300	0.006344

$$Emission\ Index\ (EI) = \frac{Dp}{m_{fuel}} \left(\frac{gr}{kg} \right) = 32 * sNOx \quad (14.3)$$

Therefore, inequality relation has been created is given below.

$$\frac{TSCF \left(\frac{gr}{h * kN} \right)}{1000} * time\ (s) * 32 * sNOx \leq 36 + 2.42 * \pi_{\infty} \quad (14.4)$$

Table x gives the result of calculations of emission standard given above. Also, emissions of the engine PHOENIX is compared in this table with the emission standard. LTO (Landing Take-Off) Cycle covers the segments below 3000 ft altitude.

Table 48. LTO Cycle for Supersonic Engines and Emission Comparison Between Phoenix and Standards

Missions	Power (%)	Time in Mode (minutes)	Dp/Foo NOx (gr/kN)	
			Engine Phoenix	Emission Standards
Taxi Out	3.8	15	23.48	132.39
Take Off	100	1	23.52	
Approach & Touchdown	34	7.5	23.48	
Taxi In	3.8	6	61.91	
			Σ	191.05

15. PERFORMANCE CONSTRAINT ANALYSIS

Performance constraint analysis is about to investigate aircraft characteristics by determining the thrust-to-weight ratio as a function of wing loading. It is important that this analysis includes all flight conditions. Thus, with the new Phoenix engine, the preliminary performance constraint analysis of the Concorde can be determined by developing take-off distance constraints, landing distance constraints, climb constraints and cruise constraints.

15.1. Drag Polar Estimation

To able to analyze nearly all performance constraints, the drag polar of flight configurations must be known. There is a total of five main flight configurations for the Concorde, including the clean configuration (cruise), take-off with landing gear up or down, and landing with landing gear up or down. The drag polar for each of the five main flight configurations of the Concorde could be estimated using the techniques outlined in Ref [98] and could be seen in Table 49.

Table 49. Drag Polar Estimations for the Concorde

Flight Configuration	Drag Polar
Low Speed, Clean	$C_d = 0.001 + 0.4201 C_l^2$
Take-off, Gear Up	$C_d = 0.0250 + 0.4776 C_l^2$
Take-off, Gear Down	$C_d = 0.0420 + 0.4776 C_l^2$
Landing, Gear Up	$C_d = 0.07 + 0.5534 C_l^2$
Landing, Gear Down	$C_d = 0.0870 + 0.5534 C_l^2$

15.2. Take-off Distance, Landing Distance, Climb and Supersonic Cruise Constraints

Firstly, one of the most important performance constraints is take-off distance. The Equation (15.1), rearranged form of the equation from Ref [98], can be utilized to describe the take-off performance constraint. In this equation, the required runway length (s_{TOG}) for Concorde used as 11800 feet from Ref [99] and μ_G ground friction coefficient is selected as 0.03 from Ref [98]. Secondly, the Equation (15.2), rearranged form of the equation from Ref [98], can be utilized to describe the landing distance constraint. The landing distance performance constraint is a single value that the wing loading cannot exceed. Thirdly, the Equation (15.3), rearranged form of the equation from Ref [98], can be utilized to describe the climb distance constraint. The Concorde is sized for climb by FAR 25.121(OEI), which is a balked landing climb with one engine inoperative. Lastly, the Equation (15.4), rearranged form of the equation from Ref [100], can be utilized to describe the supersonic cruise constraint at Mach 2 and 53000 feet. All these equations and inputs are used in developed MATLAB code and the constraint diagram of the Concorde with Phoenix engine is generated with design point as shown in Figure 57.

$$\left(\frac{T}{W}\right)_{TO} = \frac{\mu_G}{K_2} + \frac{0.0447 \left(\frac{W}{S}\right)_{TO}}{K_2 s_{TOG} \rho_{sea} C_{Lmax,TO}} + \frac{0.72 C_{D_0(TO,GD)}}{K_2 C_{Lmax,TO}} \quad K_2 = 0.75 * \frac{5 + \lambda}{4 + \lambda}, \quad \left(\frac{W}{S}\right)_{TO} = \frac{\rho_{sea} V_{SL}^2 C_{Lmax,L}}{2 \left(\frac{W_L}{W_{TO}}\right)} \quad (15.1), (15.2)$$

$$\mu_G = 0.03, \quad \lambda = 1.9917, \quad s_{TOG} = 11800 \text{ ft}, \quad \rho_{sea} = 0.00237 \frac{\text{slug}}{\text{ft}^3}, \quad C_{Lmax,TO} \approx 1, \quad C_{Lmax,L} \approx 1.2, \quad \frac{W_L}{W_{TO}} = 0.8$$

$$\left(\frac{T}{W}\right)_{TO} = \frac{N_{engine}}{N_{engine} - 1} \left(\frac{1}{L/D_{approach}} + CGR \right), \quad \left(\frac{T}{W}\right)_{TO} = \frac{\beta}{\alpha} \left(K_1 \frac{\beta}{q_{cruise}} \left(\frac{W}{S}\right)_{TO} + \frac{C_{D_0(clean)}}{\frac{\beta}{q_{cruise}} \left(\frac{W}{S}\right)_{TO}} \right) \quad (15.3), (15.4)$$

$$N_{engine} = 4, \quad L/D_{approach} \approx 1.2, \quad CGR = 0.021, \quad \alpha = 0.2, \quad \beta = 0.95, \quad K_1 = 0.24, \quad q_{cruise} = 586.9 \frac{\text{slug}}{\text{ft}^2 \cdot \text{s}^2}$$

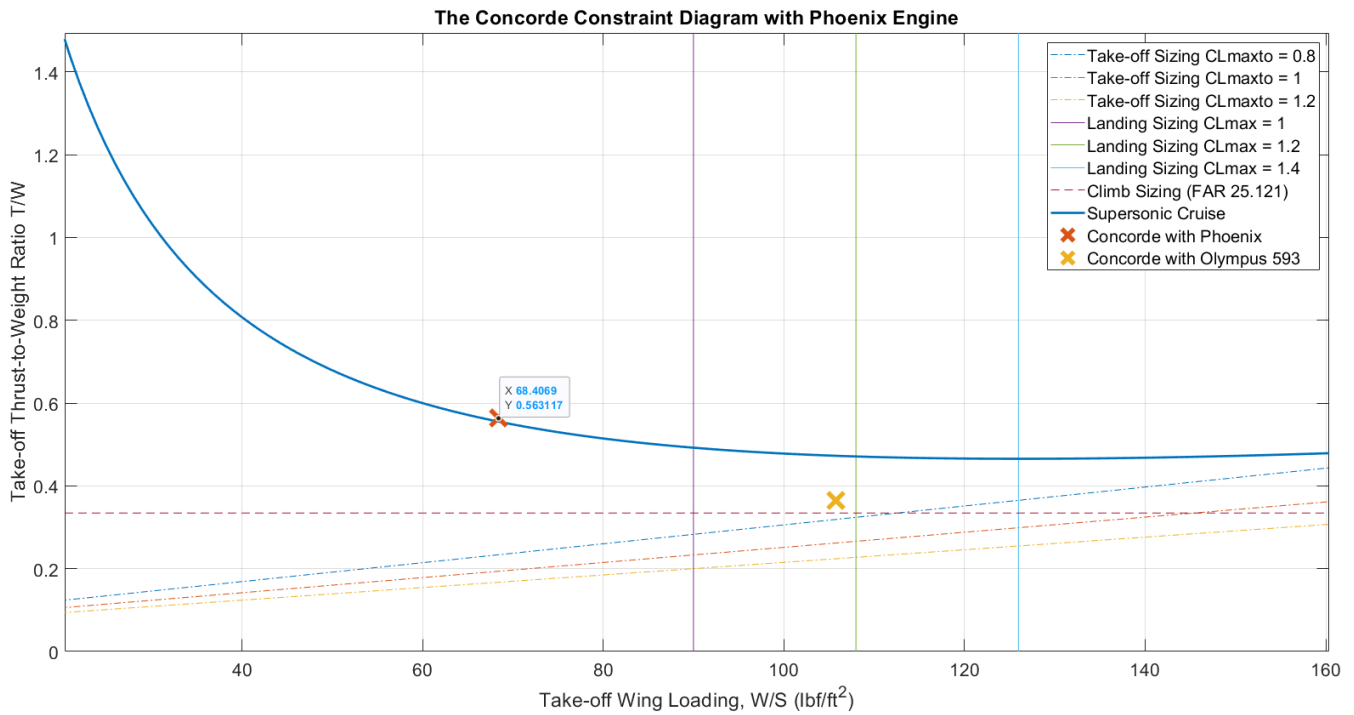


Figure 57. The Concorde Constraint Diagram with Phoenix Engine

16. ENGINE FLOW PATH

The airflow path of the PHOENIX Engine which is created from the 3-D model, is demonstrated in Figure 58. In Figure 58, the blue color represents the cold side and the red color represents the hot side.

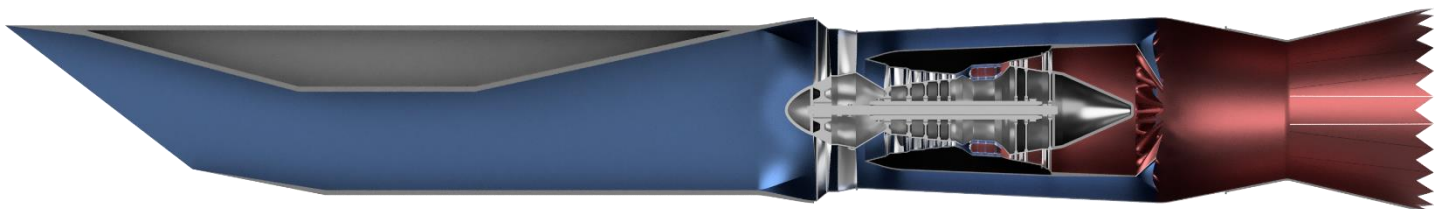


Figure 58. The PHOENIX Engine Airflow Path (blue=cold side, red=hot side)

17. CONCLUSION

Although the Concorde is the lead aircraft for supersonic civil transport, it has a couple of disadvantages which are high fuel consumption and high jet velocity due to having a turbojet engine with afterburner causes extremely high fuel consumption and high jet velocity during take-off. Additionally, the accident that the Concorde has been involved in induced its retirement from aviation. The scope of this project was to revive the Concorde with a low bypass mixed flow turbofan engine. The primary goal of this transition is to reduce fuel consumption and jet velocity.

Engine Phoenix, our latest design, is intended for use with 92-128 passengers and crew at 2.01 Mach and 53,000 feet above sea level. The base engine, Olympus 593 MK 610, is validated in Gasturb13 software considering the output table given in RFP [101]. After validation, a low bypass mixed turbofan engine is created. Beginning of the new engine design, the engine mass flow rate must be determined to satisfy the required thrust. Four design parameters, overall pressure ratio (OPR), turbine entry temperature (TET), fan pressure ratio (FPR) and bypass ratio (BPR) are optimized to reduce the thrust-specific fuel consumption considering the technologies and materials that can be developed until 2028. Several constrain values are also used in the optimization phase, such as thrust for cruise and takeoff (to minimize jet velocity), engine weight and duration (satisfied by reducing both the LP and LT stages), and NO_x emission values that are lower than regulations and requirements. Finally, in terms of specific fuel consumption and engine weight, the PHOENIX engine improved by approximately 30% and 19.5%, respectively. Furthermore, as compared to the Olympus engine, the PHOENIX Engine's jet velocity at take-off is less than 1150 ft/s.

Another step of this project is to design each component in detail. In this chapter, 1-D MATLAB code and AxSTREAM software are used. 2-D and 3-D CFD analyses were performed during the design of components such as the intake, combustion chamber, and nozzle in order to satisfy and improve the design produced by the MATLAB code. AxSTREAM software was used to develop turbomachinery components such as the fan, compressor, and turbine. After all of the analyses and designs of the components were completed, Solidworks software was used to build 3-D CAD models. Materials of components have been determined by a comprehensive literature survey, considering the technology of 2028. The modern aviation industry is rapidly evolving as a result of technological advancements. Therefore, the PHOENIX engine, which is outlined in this project, is a turbofan for reviving supersonic civil transportation at a cost that is affordable. Finally, in Table 50, the certain specifications of the PHOENIX Engine are demonstrated.

Table 50. Features and Improvements of the PHOENIX Engine

Parameters	OLYMPUS 593	PHOENIX	Limitations and Improvements
Cruise Thrust (lbf)	10031	10044	Satisfied
Cruise TSFC (lbm/lbf*h)	1.33	1.02	23 % Improvement
Total Fuel Weight Consumption (lbm)	53579	31212	30 % Improvement
Total Fuel Cost (\$), Per Operation of One Engine	36149	\$25106	\$11043 Improvement
Total Engine Weight (lbm)	7000	5640	19% Improvement
Engine Thrust to Weight Ratio	5.4	5.96	10% Improvement
Nozzle Exit Velocity at Take-off (ft/s)	$V_9 > 1150$	1148	Limitation Satisfied
Reheat at Take-off	YES	NO	Satisfied



Figure 59. Final Representation of ETU-PHOENIX

18. REFERENCES

- [1] 2021 AIAA Undergraduate Team Engine Design RFP
- [2] "Bypass Ratio," [Online]. Available: https://en.wikipedia.org/wiki/Bypass_ratio. [Last received: 10 April 2021].
- [3] "MIT Thermodynamics Notes," MIT, [Online]. Available: <http://web.mit.edu/16.unified/www/FALL/thermodynamics/notes/node82.html>. [Last received: 10 April 2021].
- [4] Emanuel Fleuti, Silvio Maraini, "Taxi-Emissions at Zurich Airport, Calculation Analysis and Opportunities", Zürich, Page:16
- [5] Brian Calvert, "Flying Concorde", 1982, NY, Pages: 123 and 82
- [6] Payne, C. E. G. (1967). *Olympus 593 Control System. Aircraft Engineering and Aerospace Technology*, 39(4), 10–16. doi:10.1108/eb034252
- [7] https://www.planestats.com/aptot_2016mar (Accessed on 2021, April 16)
- [8] Lynam, Joe (19 July 2006). "Are the skies turning green?". BBC News.
- [9] John D. Eames, "Concorde Operations", SAE Transactions, 1991, Vol. 100, Section 1: JOURNAL OF AEROSPACE, Part 2 (1991), pp. 2603-2619
- [10] https://www.highskyflying.com/how-long-does-it-take-for-a-plane-to-descend-and-land-rule-of-three/#The_Rule_of_Three (Accessed on 2021, April 16)
- [11] <https://flyfa.com/difference-between-two-spool-engines-and-three-spool-engines/> (Flying Academy Website)
- [12] THERMODYNAMIC ANALYSIS OF TURBOFAN ENGINE R. Yadav Emeritus Professor of Mechanical Engineering, MNNIT, Allahabad (U.P.)-211004 INDIA email: ramashishy@yahoo.com
- [13] Future SST Engines with particular reference to Olympus 593 Evolution and Concorde Experience." P.H. Calder and P.C Gupta SAE 751056, presented at National Aerospace Engineering and Manufacturing Meeting, Culver City, Los Angeles. November 1975.
- [14] Farokhi, Saeed, Aircraft Propulsion, Wiley, 2nd Edition, 2014
- [15] Whitford, R., "Design for Air Combat", Jane's, London, 1987.
- [16] Aziz, M. A., Elbanna, H. M., & Abdelrahman, M. M. (2010). Design optimization of a three dimension supersonic intake using the CFD-RC package. In *Tenth International Congress of Fluid Dynamics (ICFD10)*.
- [17] Fisher, S. A., Neale, M. C., & Brooks, A. J. (1970). On the sub-critical stability of variable ramp intakes at mach numbers around 2.
- [18] Sepahi-Younsi, J., Esmaeili, S., Forouzi Feshalami, B., Pellerito, V., & Hassanalian, M. (2019). Performance Enhancement of an External Compression Intake by the Boundary Layer Suction. In *AIAA Propulsion and Energy 2019 Forum* (p. 4320).
- [19] Soltani, M. R., Sepahi Younsi, J., & Daliri, A. (2015). Performance investigation of a supersonic air intake in the presence of the boundary layer suction. *Proceedings of the Institution of Mechanical Engineers, Part G: Journal of Aerospace Engineering*, 229(8), 1495-1509.
- [20] Candel, S. (2004). Concorde and the future of supersonic transport. *Journal of propulsion and power*, 20(1), 59-68.
- [21] Mattingly Jack D., Heiser William. H., Pratt David T., Aircraft Engine Design, AIAA Education Series, Reston, Virginia, 2nd Edition, 2002
- [22] Cohen H., Rogers GFC, Saravanamuttoo HIH, Gas Turbine Theory, Longman Group Limited, England, 4th Edition, 1996.
- [23] Walsh, P. P., & Fletcher, P. (2004). *Gas turbine performance*. John Wiley & Sons.
- [24] Jerry M. Seitzman, "Turbomachinery - Axial Turbine Design and Performance (gatech.edu)"
- [25] <https://turboerodesign.com/> [Access Date 03.18.2021]
- [26] Cumpsty Nicholas, Jet Propulsion: Aerodynamic and Thermodynamic Design and Performance of Jet Engines, Cambridge University Press, New York, USA, 7th Edition, 2009
- [27] Gordon C., Aerothermodynamics of Aircraft Engine Components, American Institute of Aeronautics and Astronautics, Broadway, New York, 3rd Edition, 1989
- [28] Lefebvre, A. H. (1998). *Gas turbine combustion*. CRC press.
- [29] Royce, R. (2015). *The jet engine*. John Wiley & Sons.
- [30] Lefebvre Arthur H., Ballal Dilip R., Gas Turbine Combustion Alternative Fuels and Emissions, CRC Press Taylor & Francis Group, England, 3rd Edition, 2010
- [31] Çelik, E., USLU, S., TOPAL, A., & Battaloğlu, H. (2013). Reacting CFD Simulations Through a Small Turbojet Combustor with Pre-Filming Air-Blast Atomizer. In *21st ISABE Conference*.
- [32] Tacina Robert R., "Low NO, Potential of Gas Turbine Engines", American Institute of Aeronautics and Astronautics, 28th Aerospace Sciences Meeting, Reno, Nevada, January 1990
- [33] Mohammed B. S., Jeng S. M., "Design procedures and a Developed Computer Code for Preliminary Single Annular Combustor Design", 45th AIAA/ASME/SAE/ASEE Joint Propulsion Conference & Exhibit, Denver, Colorado, August 2009
- [34] Conrado Ana Costa et al., "Basic Design Principles For Gas Turbine Combustor", 76 Proceedings of the 10o Brazilian Congress of Thermal Sciences and Engineering, ABCM, Rio de Janeiro, Brazil, Nov. 29-Dec. 03, 2004
- [35] McCormic, D. C. and Bennett, J. C. Jr., "Vortical and Turbulent Structure of a Lobed Mixer Free Shear Layer," AIAA Journal, Vol. 32, No.9, Sep. 1994, pp 1852-1859.
- [36] Paul Traub, Dominik Broszat, Thomas Röber and Jens Wellner, Germany, "Exhaust (broadband) noise simulation of a realistic turbofan forced mixer by using a CFD/CAA-approach"
- [37] Baran İper, Çağdaş Cem Ergin, Burak Cenik, Tacettin Utku Süer and Sıtkı Uslu, Ankara, "Investigation of the Effects of Lobe Number and Configuration on Mixing Performance in Lobed Mixer"
- [38] BABBITT, R., COHN, J., & FLEMING, K. (1991), "Advanced high bypass mixed-flow exhaust system design study. 27th Joint Propulsion Conference"
- [39] Zhi-qiang Sheng, Pei-lin Huang, Tong Zhao, Jin-zu Ji, "Configurations of lobed nozzles for high mixing effectiveness"
- [40] G. Eric, T. Dwain and D. Rich, "Nozzle Selection and Design Criteria," American Institute of Aeronautics and Astronautics, SPIRITECH Advanced Products, Inc., 2004.
- [41] Aircraft engine design, Jack D. Mattingly, William H. Heiser, David T. Pratt., 2nd ed. (2002)
- [42] Noise Reduction Concept Using Variable Exhaust Nozzle for Supersonic Aircraft Junichi Akatsuka1, Yasushi Watanabe2, and Tatsuya Ishii3 Japan Aerospace Exploration Agency, Mitaka, Tokyo 181-0015, Japan
- [43] James Mabe, "Variable area jet nozzle for noise reduction using shape memory alloy actuators", June 29-July4, 2008, Seattle
- [44] Junichi Akatsuka, Yasushi Watanabe, and Tatsuya Ishii, "Simple Jet Noise Reduction Technique for Variable Nozzle of Supersonic Aircraft", Japan Aerospace Exploration Agency, Mitaka, Tokyo, 181-0015, Japan
- [45] Eric J. Bultemeier, Ulrich Ganz, John Premo, Eric Nesbitt, "Effect of Uniform Chevrons on Cruise Shockcell Noise", The Boeing Company, Seattle, WA, 98124
- [46] Frederick T. Calkins and George W. Butler, "Variable Geometry Chevrons for Jet Noise Reduction", Boeing Commercial Airplanes, Seattle WA 98124
- [47] Kerrebrock Jack L., Aircraft Engines and Gas Turbines, The MIT Press, London, England, 2nd Edition, 1992
- [48] Budynas Richard G., Nisbett J. Keith, "Shigley's Mechanical Engineering Design", Mc Graw Hill, New York, 9th Edition, 2010
- [49] Hibbeler R.C., "Mechanics of Materials", Pearson, USA, 8th Edition, 2011
- [50] Egik Rulmanlar, Ardmak, < <http://www.ardmak.com/urun-35-Egik-Rulmanlar.html>>, (Access Date 05.10)
- [51] Budynas, R. G., Nisbett, J. K., & Tangchaichit, K. (2005). Shigley's mechanical engineering design (pp. The-McGraw). New York: McGraw Hill.
- [52] Ugural, A. C., & Fenster, S. K. (2011). Advanced mechanics of materials and applied elasticity. Pearson Education.
- [53] BP Production Data, BP Turbo Oil 2197
- [54] Davide Boiani, "Finite Element Structural and Thermal Analysis of JT9D Turbofan Engine First Stage Turbine Blade", Bachelor Thesis, Alma Mater Studiorum, Bologna, Italy
- [55] P2SI-900HT-Datasheet, <https://www.proofresearchacad.com/products/prepregs/P2SI-900HT-Datasheet>
- [56] KTW Titan Matrix Composite (TMC), <https://ktwtechnology.de/en/products/titan-matrix-composite/>
- [57] Muktinutalapati Nageswara Rao, "Materials for Gas Turbines – An Overview", VIT University, India
- [58] Kawagishi Kyoko, Yeh An-Chou, Yokokawa Tadaharu, Koyashi Toshiharu, Koizumi Yutaka, Harada Hirsohi, "Development of an Oxidation Resistant High Strength Sixth Generation Single-Crystal Superalloy TMS-238", 12th International Symposium on Superalloys, 2012.
- [59] Pollock T. M., Tin Sammy, "Nickel-Based Superalloys for Advanced Turbine Engines: Chemistry, Microstructure, and Properties", Journal Of Propulsion
- [60] Sato Akihiro, Harada Hiroshi, Yeh An-Chau et al., "A 5th Generation Sc Superalloy With Balanced High-Temperature Properties and Processability", TMS (The Minerals, Metals and Materials Society), 2008
- [61] Linke Andreas, Diesinger, Systems of Commercial Turbofan Engines an Introduction to Systems Functions, Springer-Verlag Berlin Heidelberg, 1st Edition, 2008
- [62] Long term performance of polymers, <www.m.eumn.edu/labs/composites/Project_s/Polymer%20Heat%20Exchanger/Creep%20description.pdf>, (Accessed on: 2021, April 20)
- [63] El-Sayed Ahmed, Emeara Mohamed S, "Aero-Engines Intake: A Review and Case Study", The International Conference of Engineering Sciences and applications, Aswan, Egypt, January 2016.
- [64] Carbon Fiber Reinforcements, Hexcel, <<http://www.hexcel.com/Products/Fabrics-Reinforcements/Carbon-Fiber-Reinforcements>>, (Accessed on: 2018, February 25)
- [65] Lin Jinbao, Jin Yanjuan, Zhang Zhu, Cui Xiaochao, "Strength Analysis of the Carbon-Fiber Reinforced Polymer Impeller Based on Fluid Solid Coupling Method", Mathematical Problems in Engineering, Volume 2014 (2014), Article ID 803261, April 2014
- [66] Titanium Alloys - Ti6Al4V Grade 5, Azo Materials, <<https://www.azom.com/properties.aspx?ArticleID=1547>>, (Accessed on: 2018, February 22)
- [67] Titanium Ti-6Al-4V (Grade 5), ASM Aerospace Specifications Metals Inc, <http://asm.matweb.com/search/SpecificMaterial.asp?bassnum=mtp642>, (Accessed on: 2018, March 22)
- [68] DiCarlo J, Jacobson N, Lizcano M., Bhatt R., "Ultra High Temperature (UHT) SiC Fiber", NASA Aeronautics Mission Directorate FY11 Seedling Phase I Technical Seminar, June 2012
- [69] Bertrand J. D., "Ceramic Matrix Composite Characterization Under a Gas Turbine Combustion and Loading Environment", Wright-Patterson Air Force Base, Ohio, March 2014
- [70] Ultramet, <<http://www.ultramet.com>>, (Accessed on: 2021, March 15)
- [71] NASA-Small Business Innovation Research, <<http://sbir.gsfc.nasa.gov/>>, (Accessed on: 2018, February 20)
- [72] Petko Jeanne F., Kiser Douglas, McCue Terry, "Characterization of C/SiC Ceramic Matrix Composites (CMCs) with Novel Interface Fiber Coatings", QSS Group, Inc., Cleveland, Ohio, USA, 2002
- [73] Shirooyeh Mahmood R., "Mechanical Properties Of Ytria-Stabilized Zirconia Ceramics", Faculty Of The Usc Graduate School, December 2011
- [74] Kawagishi Kyoko, Yeh An-Chou, Yokokawa Tadaharu, Koyashi Toshiharu, Koizumi Yutaka, Harada Hirsohi, "Development of an Oxidation Resistant High Strength Sixth Generation Single-Crystal Superalloy TMS-238", 12th International Symposium on Superalloys, 2012.
- [75] Sato Akihiro, Harada Hiroshi, Yeh An-Chau et al., "A 5th Generation Sc Superalloy With Balanced High Temperature Properties and Processability", TMS (The Minerals, Metals and Materials Society), 2008
- [76] Materials of Rolling Bearing Technology, IINAA FAG, Schaeffler
- [77] Nishikawa Takashi, Hayashi Nao, Hayakawa Akiko, "Technical Trend of Aircraft Bearings", Ntn Technical Review, 2014
- [78] J. Lapin "TiAl-based alloys: present status and future perspectives", Institute of Materials and Machine Mechanics, Slovak Academy of Sciences, April 2009
- [79] E. M. Greitzer ve H. N. Slater, «Design Methodologies for Aerodynamics, Structures, Weight, and Thermodynamic Cycles – Final Report.» MIT - Aurora, Cleveland, 2010.
- [80] Lolis, P. (2014). Development of a preliminary weight estimation method for advanced turbofan engines
- [81] http://navybm.com/study%20material/14008a/14008A_ch5.pdf [Last received: 15 March 2021].
- [82] <https://blog.softinway.com/gas-turbine-lubrication-systems/> [Last received: 15 March 2021].
- [83] https://link.springer.com/content/pdf/10.1007%2F978-3-540-73619-6_3.pdf [Last received: 15 March 2021].
- [84] <https://tr.pinterest.com/pin/598626975456135501> [Last received: 15 March 2021].
- [85] <http://aeromodelbasic.blogspot.com/2012/02/ice-protection-introduction.html>
- [86] Saravanamuttoo, H. I., Rogers, G. F. C., & Cohen, H. (2001). *Gas turbine theory*. Pearson Education.
- [87] <http://airbusone.blogspot.com/2013/05/auxiliary-power-unit.html> [Last received: 31 March 2021].
- [88] <https://www.aircraftsystemstech.com/p/air-turbine-starters-air-turbine.html> [Last received: 31 March 2021].
- [89] <https://www.aircraftsystemstech.com/2017/04/aircraft-engine-starting-systems.html> [Last received: 31 March 2021].
- [90] <http://uted.org/fadec-nedir/> [Last received: 31 March 2021].
- [91] <https://www.baesystems.com/en-us/definition/what-is-fadec#> [Last received: 31 March 2021].
- [92] <https://www.semanticscholar.org/topic/FADEC/461412> [Last received: 31 March 2021].
- [93] <http://uteddergi.com> [Last received: 31 March 2021].
- [94] <https://ifpmag.mdmpublishing.com/fire-extinguishing-and-detection-systems-in-general-aviation/> [Last received: 31 March 2021].
- [95] <https://www.aircraftsystemstech.com/p/engine-fire-extinguishing-system.html>
- [96] ICAO Meeting Presentation, Kenya, 2014
- [97] Kyprianidis, K. G., Nalianda, D., & Dahlquist, E. (2015). A NOx emissions correlation for modern RQL combustors. *Energy Procedia*, 75, 2323-2330.
- [98] Jan Roskam. Airplane Design: Preliminary configuration design and integration of the propulsion system DARcorporation, 1985.
- [99] <https://en.wikipedia.org/wiki/Concorde> (12.05.2021)
- [100] Maningly, J.D. Hever, W.H., and Prnn, D.T., "Aircraft Engine Design," J.S. Pr:el11ieniecki Ed., AIAA, Reston Virginia, 2002.
- [101] Kurzke, J., & Halliwell, I. (2018). *Propulsion and power: an exploration of gas turbine performance modeling*. Spring

APPENDIX A

Low-Pressure Compressor

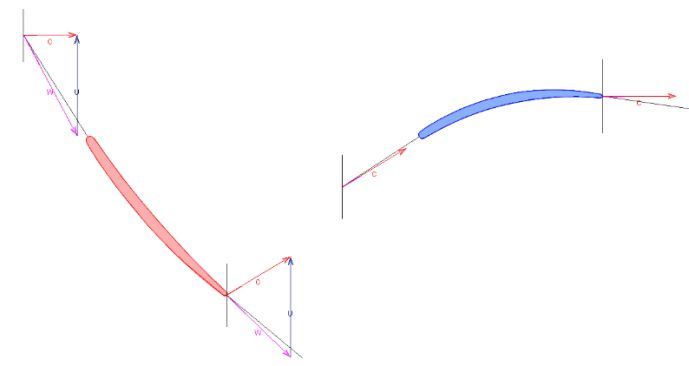


Table 51. Properties of Velocity Triangles for Mid-Section of LPC

Mid-Section	1 st Rotor Inlet	1 st Stator Inlet	1 st Rotor Outlet	1 st Stator Outlet
C [ft/s]	695.40	967.77	967.77	965.17
B [tan.deg]	28.05	59.09	45.9	90.00
A [tan.deg]	90.00	59.09	59.09	90.00
K ₁ [tan.deg]	32.32	56.93	-	-
W [ft/s]	1478.7	-	1158.4	-
U [ft/s]	1304.98	-	1304.98	-
K ₂ [tan.deg]	-	-	50.3	98.18

Figure 60. Velocity Triangles of Low-Pressure Compressor for Mid-Section

High-Pressure Compressor

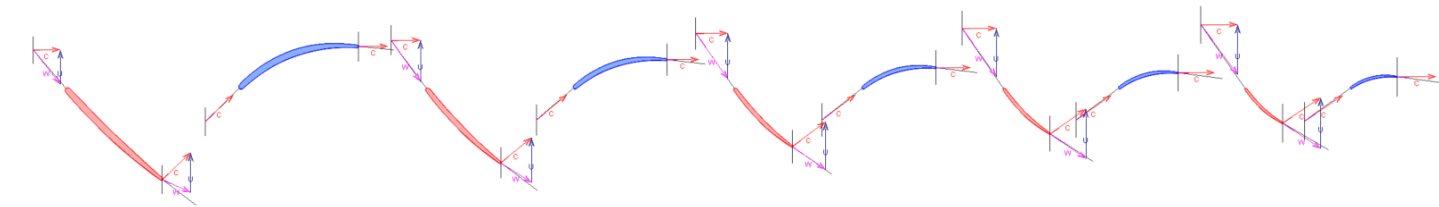


Figure 61. Velocity Triangles of High-Pressure Compressor for Mid-Section

Table 52. Properties of Velocity Triangles for Mid-Section Inlet of High-Pressure Compressor

Mid-Section	1 st Rotor Inlet	1 st Stator Inlet	2 nd Rotor Inlet	2 nd Stator Inlet	3 rd Rotor Inlet	3 rd Stator Inlet	4 th Rotor Inlet	4 th Stator Inlet	5 th Rotor Inlet	5 th Stator Inlet
C [ft/s]	809.87	1161.32	881.75	1181.49	953.62	1230.64	1025.49	1292.03	1097.36	1359.57
B [tan.deg]	38.40	46.75	35.77	50.96	35.17	53.52	35.59	55.24	36.49	56.47
A [tan.deg]	90.00	46.75	90.00	5.96	90.00	53.52	90.00	55.24	90.00	56.47
K ₁ [tan.deg]	40.48	45.71	36.68	49.63	35.10	51.95	34.72	53.47	34.97	54.54
W [ft/s]	1303.93	-	1508.33	-	1655.65	-	1762.19	-	1845.42	-
U [ft/s]	1021.93	-	1223.77	-	1353.43	-	1433.07	-	1483.70	-

Table 53. Properties of Velocity Triangles for Mid-Section Outlet of High-Pressure Compressor

Mid-Section	1 st Rotor Outlet	1 st Stator Outlet	2 nd Rotor Outlet	2 nd Stator Outlet	3 rd Rotor Outlet	3 rd Stator Outlet	4 th Rotor Outlet	4 th Stator Outlet	5 th Rotor Outlet	5 th Stator Outlet
C [ft/s]	1161.32	881.72	881.5	953.62	1230.64	1025.49	1292.04	1097.36	1359.57	1169.24
B [tan.deg]	65.57	90.00	50.96	90.00	55.30	90.00	55.24	90.00	56.20	90.00
A [tan.deg]	46.75	90.00	57.57	90.00	53.52	90.00	55.24	90.00	56.46	90.00
W [ft/s]	929.00	-	1087.30	-	1203.54	-	1291.77	-	1363.75	-
U [ft/s]	1180.05	-	1327.30	-	1416.66	-	1472.94	-	1509.64	-
K ₂ [tan.deg]	52.88	95.72	53.23	96.51	54.92	97.06	57.19	97.47	59.72	97.79

High-Pressure Turbine

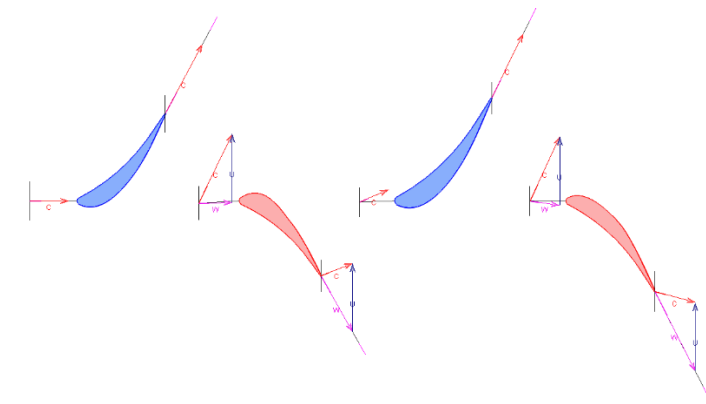


Figure 62. Velocity Triangles of High-Pressure Turbine for Mid-Section

Table 54. Properties of Velocity Triangles for Mid-Section of High-Pressure Turbine

Mid-Section	1 st Stator Inlet	1 st Rotor Inlet	1 st Stator Outlet	1 st Rotor Outlet	2 nd Stator Inlet	2 nd Rotor Inlet	2 nd Stator Outlet	2 nd Rotor Outlet
C [ft/s]	932.75	1823.30	1862.24	810.51	753.38	1672.96	1694.25	997.84
B [tan.deg]	90.00	88.81	28.39	29.62	112.76	98.41	26.41	27.15
A [tan.deg]	90.00	26.04	28.39	111.07	112.76	24.90	26.41	75.00
K ₁ [tan.deg]	90.00	86.69	-	-	91.79	89.93	-	-
W [ft/s]	-	800.51	-	1530.18	-	712.13	-	2112.50
U [ft/s]	-	1621.64	-	1621.61	-	1621.57	-	1621.54
K ₂ [tan.deg]	-	-	28.39	29.62	-	-	26.41	27.09
K _g [tan.deg]	-	-	28.39	29.62	-	-	26.41	27.09

Low-Pressure Turbine

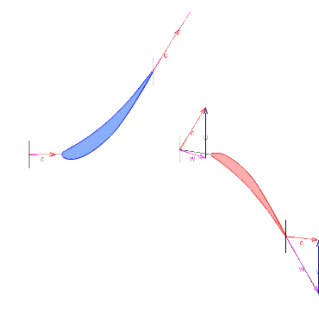


Figure 63. Velocity Triangles of Low-Pressure Turbine for Mid-Section

Table 55. Properties of Velocity Triangles for Mid-Section of LPT

Mid-Section	1 st Stator Inlet	1 st Rotor Inlet	1 st Stator Outlet	1 st Rotor Outlet
C [ft/s]	869.45	1569.73	1590.62	1045.09
B [tan.deg]	90.00	108.13	32.49	30.20
A [tan.deg]	90.00	31.76	32.49	83.47
K ₁ [tan.deg]	90.00	98.64	-	-
W [ft/s]	-	869.51	-	2063.81
U [ft/s]	-	1605.24	-	1664.74
K ₂ [tan.deg]	-	-	32.49	29.84
K _g [tan.deg]	-	-	32.49	29.84

APPENDIX B: TECHNICAL DRAWINGS OF THE COMPONENTS

	Units	St 2	St 21	St 25	St 3	St 4	St 44	St 45	St 5	St 6	St 13	St 16	St 64	St 8	St 9
Mass Flow	lb/s	480,984	177,871	177,87	176,88	168,981	178,573	179,242	179,564	179,564	303,113	303,113	482,677	482,677	482,677
Total Temperature	R	514,12	637,58	637,58	1359,76	2553,56	1869,06	1864,89	1535,36	1535,36	663,389	663,389	1002,9	1002,91	1002,91
Static Temperature	R	428,292	589,878	598,54	1333,66	2519,46	1777,07	1788,81	1416,26	1511,12	632,188	650,601	966,069	842,075	640,291
Total Pressure	psia	7,51582	14,5166	14,3423	171,404	165,14	39,6405	39,2277	16,1567	15,9664	16,4998	16,3618	15,879	15,879	15,879
Static Pressure	psia	3,96936	11,0475	11,4882	159,277	155,768	32,2243	33,0542	11,744	14,9887	13,9318	15,2808	13,8513	8,42684	3,1764
Velocity	ft/s	1014,8	758,522	686,202	582,54	713,345	1138,64	1036,35	1271,18	574,71	613,459	392,731	679,614	1415,23	2114,71
Area	in ²	2608,08	668,011	720,514	135,642	204,414	461,42	499,362	908,84	1680,54	1196,22	1753,19	2642,74	1818,29	2454,69
Mach Number	1	0,637402	0,572488	0,572488	0,330155	0,300629	0,566191	0,513728	0,703267	0,308405	0,49815	0,31442	0,449465	1	1,70839
Density	lb/ft ³	0,025015	0,050549	0,051805	0,322344	0,166875	0,048944	0,049875	0,022381	0,026772	0,05948	0,063393	0,038699	0,02701	0,01339
Spec Heat @ T	BTU/(lb*R)	0,24007	0,24128	0,24128	0,26006	0,297259	0,282256	0,282117	0,272454	0,272454	0,241578	0,241578	0,251052	0,251052	0,251052
Spec Heat @ Ts	BTU/(lb*R)	0,239797	0,240729	0,240829	0,259235	0,296711	0,279777	0,28009	0,268592	0,271678	0,241218	0,241431	0,249958	0,246675	0,242808
Enthalpy @ T	BTU/lb	-5,40691	24,3187	24,3187	204,489	548,164	348,842	347,63	256,21	256,21	30,5397	30,5397	114,493	114,493	114,493
Enthalpy @ Ts	BTU/lb	-25,9868	12,8208	14,9088	197,708	537,995	322,933	326,167	223,918	249,609	23,0191	27,4574	105,263	74,4672	25,1249
Entropy Function @ T		-0,150034	0,604962	0,604962	3,34474	6,01147	4,68598	4,67637	3,89073	3,89073	0,744317	0,744317	2,23289	2,23289	2,23289
Entropy Function @ Ts		-0,788437	0,331872	0,383069	3,27135	5,95304	4,47885	4,50514	3,57161	3,82754	0,575138	0,675962	2,09628	1,59932	0,623643
Eexergy	BTU/lb	27,2247	54,3031	53,9725	227,055	496,731	294,631	293,396	199,203	198,875	60,2148	59,9849	102,377	102,377	102,377
Gas Constant	BTU/(lb*R)	0,068607	0,068607	0,068607	0,068607	0,068606	0,068606	0,068606	0,068606	0,068606	0,068607	0,068607	0,068606	0,068606	0,068606
Fuel-Air-Ratio	0	0	0	0	0,019138	0,018092	0,018023	0,01799	0,01799	0	0	0	6,6178E-3	6,6178E-3	6,6178E-3
Water-Air-Ratio	0	0	0	0	0	0	0	0	0	0	0	0	0	0	

Figure 64. Detailed Output of PHOENIX at Climb Condition

Time: 15:15 Alt=53000ft / M=2.000 ISA + 9 F

	Units	St 2	St 21	St 25	St 3	St 4	St 44	St 45	St 5	St 6	St 13	St 16	St 64	St 8	St 9
Mass Flow	lb/s	494,327	185,211	185,211	184,291	158,758	165,867	186,289	186,587	186,587	329,116	329,116	495,704	495,704	495,704
Total Temperature	R	717,899	827,971	827,971	1619,84	2744,74	1962,34	1988,38	1657,15	1657,15	852,842	852,842	1136,32	1136,32	1136,32
Static Temperature	R	659,086	781,691	789,358	1602,22	2708,63	1900,36	1911,88	1563,1	1636,03	801,886	832,908	1065,56	956,707	570,334
Total Pressure	psia	10,8834	16,8349	16,0666	165,968	159,329	38,7497	38,3622	16,9936	16,8237	18,5776	18,3918	17,387	17,387	17,387
Static Pressure	psia	7,91308	13,7206	14,0632	159,169	150,344	31,8905	32,6291	13,454	15,9731	14,8223	16,9081	15,1719	9,24417	1,4818
Velocity	ft/s	842,246	751,739	686,652	480,853	737,103	1141,82	1041	1136,15	541,675	788,802	493,369	722,62	1505,28	2646,4
Area	in ²	2608,08	668,011	720,514	183,491	204,414	461,42	499,362	908,84	1680,54	1196,22	1753,19	2642,75	1818,29	2454,69
Mach Number	0,67	0,55	0,5	0,25	0,3	0,55	0,5	0,6	0,28	0,57	0,35	0,45	1	2,26327	
Density	lb/ft ³	0,032405	0,047375	0,048088	0,268131	0,146814	0,04528	0,046064	0,023232	0,026352	0,050227	0,054791	0,037378	0,02608	0,0179E-3
Spec Heat @ T	BTU/(lb*R)	0,242208	0,244526	0,244526	0,267891	0,299837	0,285203	0,285082	0,276021	0,276021	0,245055	0,245055	0,254915	0,254915	0,254915
Spec Heat @ Ts	BTU/(lb*R)	0,241529	0,243543	0,243706	0,267378	0,299423	0,282837	0,283109	0,273126	0,275408	0,243972	0,244631	0,253585	0,249431	0,241886
Enthalpy @ T	BTU/lb	43,6786	70,5318	70,5318	272,99	604,797	383,497	382,327	289,385	289,385	76,6009	76,6008	148,109	148,109	148,109
Enthalpy @ Ts	BTU/lb	29,5024	59,2387	61,1098	268,37	593,939	357,443	360,671	283,59	283,522	64,1667	71,7365	137,674	102,828	8,15251
Entropy Function @ T		1,02163	1,52882	1,52882	4,01658	6,32108	4,94641	4,93768	4,19289	4,19289	1,63408	1,63408	2,69072	2,69072	2,69072
Entropy Function @ Ts		0,721463	1,32426	1,35897	3,97475	6,26303	4,75128	4,77581	3,95933	4,14101	1,41498	1,54996	2,55445	2,05899	0,214664
Eexergy	BTU/lb	74,915	100,333	100,058	297,333	564,857	342,584	341,378	246,536	246,261	106,217	105,942	146,995	146,995	146,995
Gas Constant	BTU/(lb*R)	0,068607	0,068607	0,068607	0,068607	0,068606	0,068606	0,068606	0,068606	0,068607	0,068607	0,068607	0,068606	0,068606	0,068606
Fuel-Air-Ratio	0	0	0	0	0,018562	0,017546	0,017479	0,017447	0,017447	0	0	0	5,7963E-3	5,7963E-3	5,7963E-3
Water-Air-Ratio	0	0	0	0	0	0	0	0	0	0	0	0	0	0	
Inner Radius	in	9,06121	17,8573	8,74351	16,3134	17,9685	17,2498	17,2498	13,2823	0	23,2515	23,3255	0	0	0
Outer Radius	in	30,204	23,0546	17,487	17,9271	19,8961	21,0815	21,386	21,5804	23,1286	30,204	33,1984	29,0037	24,8628	36,1444
Axial Position	in	21,9157	21,9157	88,2243	94,7803	108,604	109,911	109,928	121,082	150,225	58,4385	150,225	183,424	205,176	254,542

Figure 65. Detailed Output of PHOENIX at Supersonic Cruise Condition

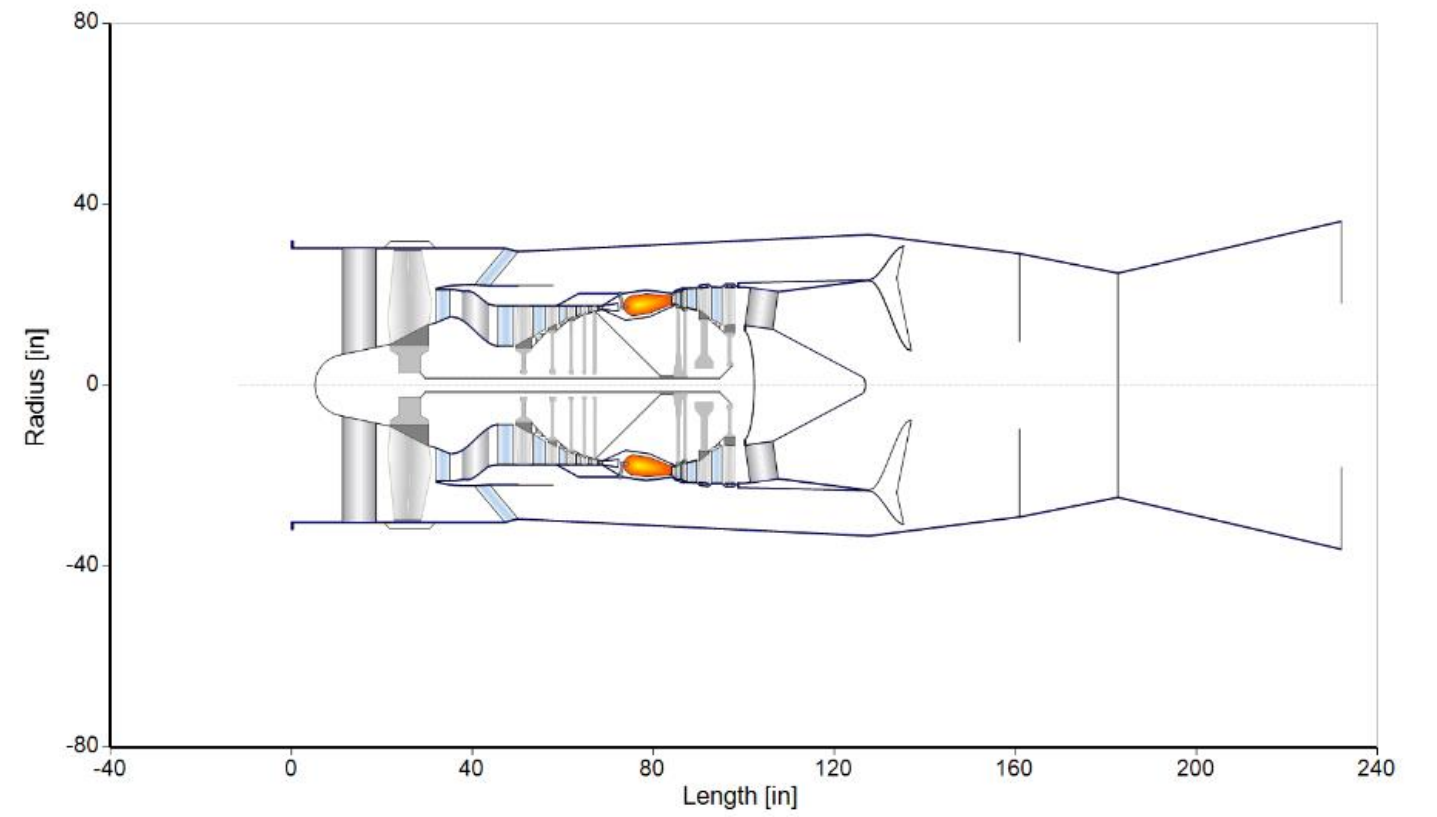


Figure 66. Engine Overall Geometry from GasTurb 13

APPENDIX C: TECHNICAL DRAWINGS OF THE COMPONENTS (Drawing Sheet Scales: A3)

